

Behaviour of Moored Ships in Harbours

Gedrag van afgemeerde schepen in havens

Behaviour of Moored Ships in Harbours

PROEFSCHRIFT

ter verkrijging van de graad van doctor
aan de Technische Universiteit Delft,
op gezag van de Rector Magnificus prof.dr.ir. J.T. Fokkema,
in het openbaar te verdedigen ten overstaan van een commissie,
door het College van Promoties aangewezen,
op maandag 20 november 2006 te 12:30 uur

door

Willem VAN DER MOLEN
civiel ingenieur
geboren te Harderwijk

Dit manuscript is goedgekeurd door de promotoren:

Prof.ir. H. Ligteringen

Prof.dr.ir. J.A. Pinkster

Samenstelling promotiecommissie:

Rector Magnificus

voorzitter

Prof.ir. H. Ligteringen

Technische Universiteit Delft, promotor

Prof.dr.ir. J.A. Pinkster

Technische Universiteit Delft, promotor

Prof.dr.ir. A.W. Heemink

Technische Universiteit Delft

Prof.dr.ir. R.H.M. Huijsmans

Technische Universiteit Delft

Prof.dr. B. Molin

Ecole Supérieure d'Ingénieurs de Marseille

Prof.dr.ir. G.S. Stelling

Technische Universiteit Delft

Dr. H.B. Bingham

Danmarks Tekniske Universitet

This research has been supported by the Water Research Centre of the Delft University of Technology.

Cover picture: Saldanha Bay, South Africa; courtesy by Google Earth.

Copyright © 2006 by W. van der Molen

Printed by Gildeprint Drukkerijen BV, Enschede, The Netherlands.

ISBN-10: 90-9021264-7

ISBN-13: 978-90-9021264-7

SUMMARY

Behaviour of Moored Ships in Harbours

A moored ship experiences problems if its motions in waves become too large. Then, line breaking accidents can occur or the movements are simply too large to continue the on or off-loading process. This is an expectable problem if the ship is moored at sea in rough wave conditions, but also in seemingly sheltered ports downtime due to wave-induced ship motions can occur if long waves with periods between 0.5 and 5 minutes penetrate in the harbour and excite harbour oscillations. Accurate modelling of the waves in the harbour as well as the forcing on the ship is required to check the wetted layout of new ports or port extensions on the safety of the berths.

Most previous studies either focussed on the (nonlinear) wave modelling in the harbour or on an accurate determination of the wave forces on a ship in travelling waves. The objective in this thesis is to develop new methods to calculate the response of a moored ship in a complex geometry taking into account low-frequency nonlinearities in the wave field and the methods should comprise coherent approaches to compute the forces on the ship in the inhomogeneous and multi-directional wave field at the berth. The methods described in this thesis consist of a coupling between models to determine the waves in a harbour or a coastal zone and models to determine the wave forces in the computed waves. The methods thus developed are suitable for different situations.

The first method consists of (1) a depth-averaged nonlinear flow model with short-wave forcing for the calculation of low-frequency wave propagation in the shore zone or penetration in the harbour, (2) a strip theory based method to determine the low-frequency wave forces from the computed wave elevations and fluid motions and (3) a ship motion simulation model which also takes into account the nonlinear properties of mooring lines and fenders. This method can be applied to determine the response of a moored ship in low-frequency waves which are either free or originate due to the occurrence of wave groups at the ocean. The short waves in the wave model are phase-

resolved so that the grid size is determined by the length of the long waves. Therefore, large coastal areas can be treated in the model, whereas the interaction between short-wave groups and bound long waves is still preserved. Only the individual short waves and short-wave diffraction are not modelled.

If long and short waves are equally important at the berth and if the area of interest is sufficiently small, the ship response can be calculated with a combined Boussinesq-panel model. This is the second method described in this thesis. Accurate results of short-wave diffraction and refraction in an arbitrary geometry, including the ensuing low-frequency nonlinearities, can be obtained with a Boussinesq-type wave model. The 3D shape of the ship cannot be incorporated directly in the Boussinesq model. Therefore, the calculated orbital velocities at the position of the hull of the ship serve as the boundary conditions in a time-domain panel model to determine the scattering of the incident waves. The first order wave force is obtained using the calculated pressures in the incident and scattered waves. Because pressures and flow velocities along the hull are known at any time, the second order wave drift forces can be determined as well.

Verification of the methods is treated for various cases including comparison with model test experiments, prototype measurements and computations with a frequency-domain panel model. Results obtained with the low-frequency strip theory approach show that large low-frequency surge motions can occur in a harbour, despite the fact that the wave height offshore is not exceptional. The large surge motion were also measured. Besides the generation of oscillations in a harbour, bathymetrical effects such as the slope of the sea bed have large effects on the low-frequency forces on a ship moored in shallow water. Comparison of computations with the Boussinesq-panel model for the first and second order forces on a ship in open water show good correspondence with model test results and computations with the same wave model, only connected with a frequency-domain panel model instead of a time-domain panel model. Further validation of this method is needed for the forces on a ship in a harbour geometry.

SAMENVATTING

Gedrag van afgemeerde schepen in havens

Een afgemeerd schip krijgt te maken met problemen als de bewegingen in golven te groot worden. Dan kunnen afmeerlijnen breken of de bewegingen zijn simpelweg te groot om door te kunnen gaan met het laad- of losproces. Dit is een verwacht probleem als het schip ligt afgemeerd op zee in ruige golfcondities, maar ook in schijnbaar beschutte havens is het mogelijk dat het laden of lossen gestopt moet worden door scheepsbewegingen als gevolg van golven met een periode tussen 0.5 en 5 minuten. Deze golven kunnen gemakkelijk in de haven doordringen en havenoscillaties veroorzaken. Nauwkeurige modellering van de golven in de haven en de krachten op het schip is noodzakelijk om het ontwerp van een nieuwe haven of een havenuitbreiding te toetsen op de veiligheid van de aanlegplaatsen.

De meeste studies in het verleden hebben zich ofwel gericht op (niet-lineaire) modellering van golven in de haven ofwel op een nauwkeurige bepaling van golfkrachten op een schip in lopende golven. De doelstelling in dit proefschrift is om nieuwe methodes te ontwikkelen om de respons van een afgemeerd schip in een complexe geometrie te berekenen, waarbij laagfrequente niet-lineariteiten in het golfveld worden meegenomen. Verder moeten de methodes coherente benaderingen bevatten om de krachten op het schip te berekenen in het inhomogene en kortkammige golfveld nabij het schip. De methodes beschreven in dit proefschrift bestaan uit een koppeling tussen modellen om de golven in een haven of in een kustgebied te bepalen en modellen om golfkrachten te bepalen in de berekende golven. De hiermee ontwikkelde methodes zijn geschikt voor uiteenlopende situaties.

De eerste methode bestaat uit (1) een dieptegemiddeld niet-lineair stromingsmodel met korte golfforcering voor de berekening van lange golfvoortplanting in de kustzone of doordringing in de haven, (2) een op striptheorie gebaseerde methode om laagfrequente golfkrachten te bepalen op basis van de berekende oppervlakte-uitwijkingen en stroomsnelheden en (3) een scheepsbewegingssimulatiemodel dat ook de niet-lineaire

eigenschappen van fenders en afmeerlijnen meeneemt. Deze methode kan worden toegepast om de respons van een schip in laagfrequente golven te bepalen, waarbij het gaat om vrije lange golven of om golven die zijn ontstaan door golfgroepen op zee. Alleen de amplitudes van de korte golven worden meegenomen in het golfmodel, zodat de gridgrootte wordt bepaald door de lengte van de lange golven. Derhalve kunnen grote kustgebieden worden gemodelleerd, terwijl de interactie tussen golfgroepen en gebonden lange golven blijft behouden. Alleen de individuele korte golven en korte golfdiffractie wordt niet gemodelleerd.

Als lange en korte golven van gelijk belang zijn op de plaats van de aanlegplaats en als het interessegebied voldoende klein is, kan de respons van het schip worden berekend met een gecombineerd Boussinesq-panelenmodel. Dit is de tweede methode beschreven in dit proefschrift. Nauwkeurige resultaten van korte golfdiffractie en -refractie in een willekeurige geometrie, met ook de daaruit volgende laagfrequente niet-lineariteiten, kunnen worden bepaald met een Boussinesq-type golfmodel. De 3D vorm van het schip kan niet worden opgenomen in het Boussinesq model. Daarom worden de berekende orbitaalsnelheden op de positie van de scheepshuid gebruikt als de randvoorwaarden in een tijddomein panelenmodel om de diffractie van de inkomende golven te bepalen. De eerste orde golfkracht wordt gevonden aan de hand van de berekende drukken in de inkomende en gediffracteerde golven. Omdat de drukken en snelheden rond de scheepshuid bekend zijn op elk moment, kunnen de tweede orde driftkrachten ook worden bepaald.

Verificatie van de methodes wordt behandeld voor verschillende gevallen, waaronder vergelijking met modelproeven, prototype metingen en berekeningen met een frequentiedomein panelenmodel. Resultaten behaald met de laagfrequente striptheorie aanpak laten zien dat grote laagfrequente verzetbewegingen kunnen voorkomen in een haven, ondanks het feit dat de golfcondities niet exceptioneel zijn. Deze grote verzetbewegingen zijn ook gemeten. Naast het genereren van oscillaties in een haven, kunnen diepteliggingseffecten, zoals de helling van de zeebodem, grote effecten hebben op de laagfrequente krachten op een schip afgemeerd in ondiep water. Vergelijking van de berekeningen met de Boussinesq-panelenmethode voor de eerste en tweede orde krachten op een schip in open water laten goede overeenstemming zien met experimentele resultaten en berekeningen met hetzelfde golfmodel, alleen gekoppeld aan een frequentiedomein panelenmodel in plaats van een tijddomein panelenmodel. Verdere validatie van deze methode is nodig voor de krachten op een schip in een havengeometrie.

CONTENTS

Summary	vii
Samenvatting	ix
List of symbols	xiv
1. Introduction	1
1.1 Shallow water ship hydrodynamics	1
1.2 Overview of existing calculation methods	4
1.2.1 Moored ship motions	5
1.2.2 Wave-body interaction	6
1.2.3 Long waves and harbour oscillations	8
1.2.4 Moored ships in complex geometries	12
1.3 Research objectives	13
1.4 General approach	15
1.5 Outline of the thesis	16
2. Model tests	17
2.1 Test set-up	17
2.2 Test program	20
2.3 Discussion on the measurements	23
3. Moored ship response in long waves: model and validation	25
3.1 Introduction	25
3.2 Model description	26
3.2.1 Infragravity wave model	26
3.2.2 Wave force formulations	28
3.3 Results for a container ship in open water	31
3.4 Results for a container ship in a harbour basin	31

3.5	Results for a coal carrier in Tomakomai Port, Japan	37
3.5.1	Prototype measurements	37
3.5.2	Simulation of infragravity waves	41
3.5.3	Simulation of ship motions	45
3.6	Results for an LNG carrier on a sloping sea bed	48
3.7	Discussion	52
4.	A Boussinesq-panel model for moored ship response in nonlinear waves	55
4.1	Computational approach	55
4.2	Model formulations	56
4.2.1	Integral equations	56
4.2.2	Equation of motion	58
4.2.3	Hydrodynamic forces	58
4.2.4	Incident waves	60
4.2.5	Wave forces	61
4.3	Numerical considerations	64
4.3.1	Numerical implementation	64
4.3.2	Irregular frequencies	66
5.	Results of the time-domain panel model for linear waves	69
5.1	200 kDWT tanker in open water	69
5.1.1	Hydrodynamic coefficients	70
5.1.2	Ship motions	74
5.1.3	Drift forces	75
5.2	Panamax container ship in a harbour	77
5.2.1	Impulse response functions	78
5.2.2	Wave forces	80
6.	Validation of the Boussinesq-panel model for nonlinear waves	85
6.1	Forces on a container carrier due to a passing ship	85
6.1.1	Wash waves	86
6.1.2	Wave forces	88
6.2	Forces on an LNG carrier in irregular short-crested waves	89
6.3	Discussion	93

7. Conclusions and recommendations	97
7.1 Conclusions	97
7.1.1 Moored ship response in long waves	97
7.1.2 Moored ship response in nonlinear waves	98
7.2 Recommendations	99
Bibliography	101
Appendix	109
A. Model test results	111
B. Computation of the Green function	115
Curriculum Vitae	119
Acknowledgements	120

LIST OF SYMBOLS

Roman symbols

Symbol	Designation
A	added mass matrix [kg]
A_x	cross-sectional area [m ²]
B	linearized viscous damping matrix [kg/s]
B_v	quadratic viscous damping matrix [kg/m]
\mathcal{B}	sea floor
C	hydrostatic restoring matrix [kg/s ²]
D	total water depth [m]
\mathcal{D}	fluid domain
D_w	wave energy dissipation rate [N/m ² /s]
E_r	roller energy [J/m ²]
E_w	wave energy [J/m ²]
\mathcal{F}	fluid surface
\vec{F}	force [N]
\vec{F}'_{FK}	cross-sectional Froude-Krylov force [N/m]
\vec{F}'_d	cross-sectional diffraction force [N/m]
F_n	Froude number [-]
F_x	surge force [N]
F_y	sway force [N]
F_z	heave force [N]
G	Green function
$G^{(0)}$	impulsive part of the Green function [1/m]
G^w	wave part of the Green function [1/m/s]
H_s	significant wave height [m]
\mathcal{H}	wetted hull surface
K	matrix with impulse response functions [kg/s ²]

Symbol	Designation
L	length of the floating body [m]
\mathbf{M}	mass matrix [kg]
\vec{M}	moment [Nm]
M_x	roll moment [Nm]
M_y	pitch moment [Nm]
M_z	yaw moment [Nm]
R	horizontal distance [m]
S	spectral variance density
\mathbf{S}	radiation stress tensor [N/m]
T	wave period [s]
T_1	mean period [s]
T_p	peak period [s]
V_s	forward speed of the (passing) ship [m/s]
\mathcal{W}	wetted surface of fixed structures
\vec{X}	body motion [m]
\mathbf{a}	frequency dependent added mass matrix [kg]
\mathbf{b}	frequency dependent damping matrix [kg/s]
b_s	sectional breadth at the waterline [m]
c	wave celerity [m/s]
c_g	group velocity [m/s]
d_s	sectional draft [m]
f	wave frequency [1/s]
g	acceleration of gravity [m/s ²]
h	(still) water depth [m]
k	wave number [rad/m]
k_s	bed roughness [m]
m_n	n^{th} moment of the variance spectrum
\mathbf{m}'	frequency dependent cross-sectional added mass matrix [kg/m]
\mathbf{n}'	frequency dependent cross-sectional damping matrix [kg/m/s]
\vec{n}	normal vector [-]
p	pressure [N/m ²]
r	radial distance [m]
t	time [s]
\vec{u}	fluid velocity [m/s]
u	fluid velocity component in the x -direction [m/s]
v	fluid velocity component in the y -direction [m/s]

Symbol	Designation
w	fluid velocity component in the z -direction [m/s]
\vec{x}	coordinate relative to the field point [m]
\vec{x}_G	coordinate of the centre of gravity [m]
x	principal horizontal coordinate [m]
y	lateral horizontal coordinate [m]
z	vertical coordinate [m]

Greek symbols

Symbol	Designation
Γ	waterline of the floating body
Δ	displacement volume [m ³]
Φ	total potential [m ² /s]
$\vec{\Omega}$	rotational displacement [rad]
$\vec{\alpha}$	total displacement [m]
β	bed slope parameter [-]
γ	peak enhancement in the wave spectrum [-]
γ_b	depth-induced wave breaking parameter [-]
δ	water depth relative to the draft of the floating body [-]
ε	transmission parameter [-]
ζ	wave elevation [m]
ζ_a	wave amplitude [m]
θ	wave direction [rad]
θ_0	mean direction [rad]
λ	wave length [m]
ν	kinematic viscosity [m ² /s]
$\vec{\xi}$	coordinate relative to the source point [m]
ρ	fluid density [kg/m ³]
σ	source strength [m ² /s]
$\vec{\tau}$	bed shear stress [N/m ²]
ϕ^I	incident wave potential [m ² /s]
ϕ^S	scattered wave potential [m ² /s]
χ	time-varying part of the radiation potential [m ² /s]
ψ	impulsive part of the radiation potential [m ² /s]
ω	angular wave frequency [rad/s]

1. INTRODUCTION

1.1 Shallow water ship hydrodynamics

Most old sea ports are situated inland, close to a river mouth, or they are well protected by breakwaters. The conditions in the harbour remain fairly calm, also in storm conditions. However, there has been a scaling-up of particularly container carriers in the last decades. To host these large ships, container terminals are moved closer to the sea and entrance channels are dredged deeper and wider. Consequently, the influence of ocean waves on a moored ship in the port is becoming more and more important. In ocean facing ports line breaking accidents have occurred, even in fairly calm weather conditions. Long waves generated in ocean storms or earthquakes (tsunamies) are amplified in the port if the wave frequency is close to a resonant frequency of the harbour basin. Protection against these long waves is much more difficult than protection against short storm waves. Long waves easily diffract around the breakwater heads, penetrate into the harbour and possibly amplify as a standing wave pattern arises. Especially large ships with soft mooring lines are heavily affected by these low-frequency harbour oscillations. Therefore, it is essential to predict the mooring forces and vessel motions in the design stage of new ports, as well as during operation, for an economic port design and safe mooring. In the design stage it is

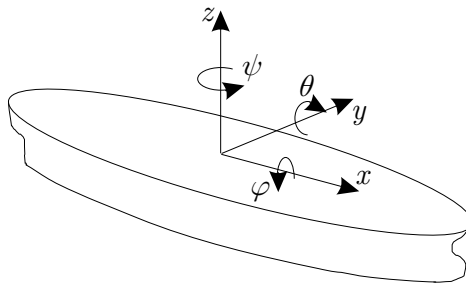


Figure 1.1: Six degrees of freedom of a moving ship

Table 1.1: Maximum allowable ship motion amplitudes

	surge	sway	heave	roll	yaw
	[m]	[m]	[m]	[°]	[°]
tanker ^{1,2}	2.5	2	1.5	4	2
ore carrier ¹	1.5	0.5	0.5	4	2
grain carrier ¹	0.5	0.5	0.5	1	1
container carrier ²	0.5	0.3	0.4	1.5	0.5
ro/ro ship ²	0.3	0.2	0.1	-	-
general cargo ship ¹	1	0.5	0.5	3	2

¹ from Bruun (1981)

² from PIANC (1995)

useful to perform several computations for various port layouts and berth locations.

The results have to include the forces in mooring lines and the vessel motions in the six degrees of freedom: surge (x), sway (y), heave (z), roll (φ), pitch (θ) and yaw (ψ), see Figure 1.1). The calculated line forces can be compared with the break strength of the ropes. Line breaking must be prevented to avoid damage to the ship and the quay wall. Besides, a breaking line is a lethal missile. In order to guarantee the safety of the port workers the occurrence of line breaking accidents must be minimized. The ship motions are important for the workability during the on- and off-loading of the ship. The prediction of ship motions is important, particularly for those ship types that allow little movements for efficient loading or offloading. In Table 1.1 the allowable ship motions are given for different ship types. The maximum allowable amplitude is given here as a single value. However, in practice this value also depends on the loading equipment and the experience of the crane driver. Furthermore, the loading process is not stopped immediately after exceeding a certain motion amplitude, but the process slows down first and is only stopped if the productivity has become very low with respect to the capacity.

The productivity of the loading process of container vessels is strongly dependent on the movements of the moored ship. Large roll motions can cause jamming of the container in the slot. In case of too large surge or sway motions the crane operator is not able to position the container at the right place at the right time and he has to wait until the movements become smaller. Jamming and waiting causes downtime and a longer stay of the ship at the berth. Also for roll-on/roll-off (ro/ro) and general cargo vessels the movements are limiting for operational conditions. Ore carriers, Liquefied Natural Gas (LNG) carriers and oil tankers allow larger movements, but the

strength of mooring lines remains as a limiting condition.

The difficulty of the protection of a harbour against resonances or seiching is stated as the Harbour Paradox (Miles & Munk, 1961): "Assuming, then, that seiches excited through the harbor entrance are the limiting factor for the usefulness of a harbor, a narrowing of the entrance leads not (as one might expect) to a reduction in harbor surging, but to an enhancement." This leads to contradictory solutions for the protection of the harbour against either short waves or long waves. The cause of the paradox is the fact that there is less radiation of waves from the harbour for a narrow entrance. Most energy in the oscillation remains inside the harbour.

Apart from the fact that long waves, although low outside, can be significant inside the harbour, there is the influence of the stiffness of the mooring system on the resulting ship motions. The ship and the mooring lines act like a mass-spring system which resonates if it is forced close to its natural frequency. To prevent the mooring line against very high tensions at small elongations, most ships are equipped with synthetic lines or steel wire ropes with a synthetic tail. Because of this, the natural surge period of the moored ship is in the range of 30 seconds to a few minutes. This is also the range of natural periods of a small harbour basin. Hence, it is important for a designer to determine whether the wave motions at the berth location are close to a natural period of the moored ship. For a profound and accurate downtime analysis of a new port it is not enough to consider just the wave heights at the berth. An integrated model is required to consider both the propagation of waves in the harbour and the response of the ship to the calculated waves.

Long waves in the range of frequencies close to harbour resonance can originate in ocean storms. Small variations of air pressure above the sea cause storm surges which propagate as free long waves. Another origin is an earthquake at the ocean floor which also causes a free long wave. Due to shoaling of these waves in shallow water, their influence becomes more important in coastal areas and ports. A third origin of long waves is the set-down beneath wave groups. Due to the irregular properties of waves, wave groups are present with varying lengths and heights. Because the radiation stress is larger underneath a group of higher waves than underneath low waves, water is expelled from the wave group and a long wave is formed with a length scale of the wave group length. The radiation stress is the contribution of the waves to the horizontal transfer of momentum. This set-down wave is bound to the wave group and therefore it does not satisfy the dispersion relation. The phase celerity of the bound wave is equal to the group velocity of the carrier waves. The height of the bound wave is negligible in deep water, but increases rapidly as the waves travel into shallow water. In shallow water, where mooring facilities are often situated, the

bound wave has a large contribution to the low-frequency drift force. A ship sailing or moored at sea tends to drift in the wave direction. This is also the cause of the fact that an anchored ship will rotate until it lies head-on to the waves. The drift force varies with the periods of passing wave groups and together with the bound wave contributes to the low-frequency force. Because of the soft mooring systems that are often applied, the low-frequency drift forces, although they may be small, are able to excite large low-frequency motions.

It is possible that the bound wave causes amplification in an open basin, although the length of the bound wave does not match a resonant wave length of the basin (Bowers, 1977). Actually the bound wave generates a long wave at the basin entrance which behaves like a free wave and this generated wave amplifies in the basin, if its frequency is close to a resonant frequency of the basin.

The main areas of concern for a port planner in his goal to minimize downtime are to reduce the wave action in the harbour and to limit the response of the moored ship to the waves that are still present. Not only for designing and engineering purposes is it important to take both aspects into account, but also for research purposes both areas need to be considered. Remarkably, research has mainly concentrated on only one or the other issue in the last decades and the coupling between both was left to the designer. Research on the behaviour of moored ships has successfully lead to the development of computer models for a ship moored to a jetty or a quay wall (e.g. Van Oortmerssen, 1976) or a Single Point Moored (SPM) tanker (e.g. Wichers, 1988). These models calculate the ship's response up to second order. The incident waves are considered as a given irregular uni-directional wave train. In case of a berth inside a harbour, where diffraction, refraction and reflections play an important role, the assumption of a uni-directional wave train is far from accurate and therefore an extension of the applications is necessary representing the behaviour of a ship in an arbitrary wave field.

1.2 Overview of existing calculation methods

In the design of ships, offshore structures and terminals the role of calculation methods is becoming more and more important, although it cannot replace model testing of new ships or structures. Turbulence and viscous effects are quantities that rely on tuning in calculation models, so that model testing and prototype measurements will remain important in the design of ships and terminals. However, accurate model testing is difficult and expensive. It is much easier to carry out computer simulations for a large number of vessel shapes or harbour geometries.

The first order potential flow of waves around a structure is now rather well understood. With the increase of computer power and the development of more efficient numerical algorithms it has become now possible to include a very accurate description of the shape of the floating body. Nevertheless, model tests will remain necessary for high-cost projects to include the correct influence of turbulence and higher order effects. Increasing insight has been gained in the past about these effects, but researchers and engineers still face many difficulties with the correct inclusion into workable numerical models.

1.2.1 Moored ship motions

Around 1970 several accidents were reported due to very large low-frequency surge motions of tankers moored to an offshore buoy. Little was known by then about the cause of these motions which were clearly at much larger periods than the incident waves. Remery and Hermans (1971) reported a method to calculate the slowly oscillating character of the surge motion based on an approximation of the drift force in regular waves. They also indicated that not only the forcing terms are important, but also an accurate description of the damping at near-resonance. This so-called Maruo/Newman far-field approach for calculation of the mean drift force (Maruo, 1960; Newman, 1967) is based on the conservation of momentum and energy. Pinkster (1980) developed the more accurate direct pressure integration technique. The main contributions are due to the integration of relative wave elevations over the water line and due to integration of particle velocities over the submerged hull. An advantage associated with this approach is that it is also possible to consider the low-frequency second order force in a bichromatic wave directly and accurately. Disadvantage is that it might be difficult to treat the derivatives of the water velocities over the body correctly. However, this should not be a problem for ships without forward speed.

A typical phenomenon that is concerned with the behaviour of moored ships or offshore structures is the non-linear characteristics of the mooring system. Even if the characteristics of fenders and mooring lines could be linearized, the system is still strongly non-linear, because stiffness is much different for the oscillating ship that is pushed against the fenders and the ship that is moving away from the fenders. Hence, a linear frequency-domain approach to analyse the behaviour of the moored ship is not satisfactory. Time-domain approaches have been used successfully in order to calculate the behaviour of the moored ship in irregular waves. Examples of these models developed in the Netherlands are TERMSIM, developed at MARIN, BAS (WL|Delft Hydraulics) and SHIPMOORINGS (Alkyon). These models are based

on the impulse response technique suggested by Cummins (1962). The retardation functions in the equation of motion can be related to frequency dependent added mass and damping coefficient through the Fourier Transform, so that frequency-domain diffraction methods can be used for the determination of the retardation functions. TERMSIM uses the bifrequency determined values of the low-frequency second order wave drift forces, where the contribution of the second order wave is determined from the solution of the wave that satisfies the second order boundary condition at the free surface according to Bowers (1976); the dispersion relation is modified in such a way that the wave length of the second order wave is equal to the group length of the short waves. The other models use an approximation of the varying drift force based on the values of the mean drift force in regular waves according to Newman (1974). This is a valid assumption in deep water. In shallow water it is less satisfactory particularly due to the influence of bound waves, which have no contribution to the mean drift force. Therefore, the contribution of the second order waves must be added explicitly, if Newman's approximation is used in shallow water. These moored ship response models are only able to integrate the equation of motion in time. The hydrodynamic coefficients and the first and second order wave force transfer functions need to be precalculated by a model that takes into account the wave-body interaction of the oscillating body in still water and the restrained body in waves. The development of the latter methods is discussed in the next section.

1.2.2 Wave-body interaction

Based on the formulations derived by Ursell (1949) for the forces on an oscillating circular cylinder Korvin-Kroukovsky and Jacobs (1957) developed a quasi three-dimensional so-called strip theory method to calculate the motions of a ship. The method treats each cross-sectional strip as if it were part of an infinitely long cylinder. Hence, the fluid flow is considered to be entirely underneath the body and the flow past the ends of the ship is neglected. This assumption reduces the application to slender bodies and to wave lengths that are short compared with the ship length for the calculation of hydrodynamic coefficients. The shape of the cross-section is mapped to the unit circle in order to be able to use Ursell's formulations for the forces on the cylinder. It takes care of forward speed in an approximate way, which is theoretically not satisfying, but the results agree well with experiments. Although far more sophisticated fully three-dimensional methods have been developed since then, strip theory is still used successfully, especially in early ship design.

The most widely used three-dimensional approaches are the panel methods, see

e.g. Faltinsen (1990) and Lee and Newman (2005) for a theoretical overview of wave force calculations using the panel method. Following the pioneering work of Hess and Smith (1962), most panel models are linear frequency-domain methods where the mean wetted part of the hull is divided into N quadrilateral panels. The velocity potential or the source strength is assumed to be piecewise constant on each element. The integral equation is then replaced by a set of N linear equations, where the singularities are located in the centre of each element. Van Oortmerssen (1976) was one of the first to develop a workable model (DIFFRAC), capable of analyzing the behaviour of a moored tanker. He was also able to include the effect of a quay wall by applying the method of images. The most widespread linear frequency-domain model is WAMIT, developed at MIT. After the initial development in the 19-eighties, the model has been extended with various modules to make it suitable for almost any type of wave-structure interaction in offshore engineering.

The advantage of these linear methods is that only panels are needed on the body surface. The satisfaction of the boundary conditions at the free surface and the radiation condition are included in the formulation of the Green function. This not only reduces the number of panels, but also overcomes difficulties that are related to open boundaries. These open boundaries are necessary to close the computational domain, if panels are used at the free surface and these boundaries often cause some difficulties to include the radiation condition accurately.

One of the main assumptions of the linear frequency-domain methods is that the motions can be regarded as a linear superposition of oscillations at different frequencies. Consequently, it is not possible to include the second order boundary conditions at the free surface.

If the response of a ship in a multi-directional wave field has to be analyzed, it is more efficient to use the time-domain approach. In these methods the body is not regarded to make purely oscillatory movements, but the response is determined forced by successive impulsive excitations. Time-integration of these excitations leads to the subsequent ship motions. This method is used in the development of the time-domain model TiMIT (MIT; Bingham et al., 1993).

Many of the more recent research activities have dealt with the development of non-linear panel methods. In these models the wetted body surface as well as the free fluid surface are represented by Rankine sources. To close the computational domain, an open boundary is required far enough away from the floating body. The models are considered non-linear, because the quantities are not evaluated on the mean wetted area of the body, but the actual body movements are considered and the panels on the body surface move with the oscillating body. Also the panels on the free surface move

with the calculated wave motions, so that higher order wave motions can be treated. Disadvantage of these methods is that the matrix containing the Green functions need to be refilled every time-step to treat the non-linearities correctly. Secondly the conditions at the open boundaries cause much trouble. In irregular waves it is very difficult to create a boundary that absorbs all wave energy and does not reflect any waves. Thirdly the regridding, particularly at the intersection between the free surface and the body, causes a lot of difficulties. For a simply shaped object, such as a cylinder or a sphere, the intersection points are easy to obtain. However, for a more complicated shape, such as a ship or a floating platform, errors are easily made to find the intersection points. Until now this has reduced the applicability to bodies of which the shape can be described by a number of polynomials. Research at the University of Twente has lead to the development of the non-linear model HYPAN. Berkvens (1998) extended the two-dimensional algorithm developed by Van Daalen (1993) to make it applicable to three-dimensional bodies. At MIT the higher order panel model HIPAN (Newman & Lee, 2002) has been developed as an extension to WAMIT for the inclusion of second order diffraction, the effect of large body motions and the possibility of treatment of e.g. a barge with a moonpool which would cause problems or inaccuracies using linear methods. They use a method of B-splines for a more accurate description of the body surface, while the number of panels is reduced. The panels are not flat, but have a certain constant curvature along which the potential is described.

It was intended to make these nonlinear wave models applicable to floating bodies in complex geometries. Instead of open boundaries at all sides, the boundaries can be partly closed, partly open, so that the shape of a harbour can be represented. However, the treatment of the open boundaries in a calculation with such a complex shape gives large errors and the simulation for a large domain, such as a realistic harbour configuration, gives problems, especially if apart from the quay walls also the bottom topography should be considered. Hence, accurate calculation of moored ship behaviour in complex geometries still involves the usage of a wave propagation model to include the effects of closed boundaries and a varying bottom topography and a model that takes into account the diffraction around the hull and the radiated waves.

1.2.3 Long waves and harbour oscillations

For the calculation of the wave field at a berth in a harbour, it is not sufficient to use a method for wave generation and propagation at open seas, because these methods

take into account the effects of refraction and shoaling, but they neglect diffraction, e.g. around breakwater heads. A relatively simple approach (Penney & Price, 1952) can be used to calculate the linear diffraction around a semi-infinite breakwater at uniform water depth. By applying the sum of the contributions of two semi-infinite breakwaters, the wave field behind a gap or a detached breakwater can be obtained. This method has been applied by Wuisman and Van der Molen (2005) to calculate wave forces and subsequent motions of a moored ship behind a breakwater. The applicability of this method is limited, because the effect of refraction in for instance shipping channels is neglected and it is inaccurate if standing waves play a role behind the breakwater.

These standing waves are often the most important cause of mooring problems in harbours. A wave that excites the whole harbour is also called a seiche. The periods of these seiches vary roughly from a minute to an hour depending on the length and depth of the basin. Seiches in open basins are caused by small long-period waves at the ocean which are excited in the basin. The generation of seiches can be due to varying wind set-up in shallow coastal waters, local atmospheric pressure changes (e.g. in storms or in convection cells; De Jong, 2004), internal waves, tsunamis or due to wave group forcing. A comprehensive description of the generation of seiches has been made by Wilson (1972). The most hazardous waves for moored ships are oscillations in the range of periods between 30 seconds and 5 minutes, which is the range of natural periods of horizontal ship motions. Free long waves accompanying short waves due to ocean storm are also in this range of periods and can therefore cause problems in small basins.

For the evaluation of wave-induced oscillations of harbours of arbitrary shape, but constant water depth, numerical solutions have been obtained by Hwang and Tuck (1970) and Lee (1971). They solve the Helmholtz equation formulated as an integral equation in the frequency-domain, which satisfies the zero normal velocity boundary conditions at the walls. To take into account the influence of varying depth a hybrid-element method can be used (e.g. Mei et al., 2005, Section 4.11). The most convenient solution is to solve the Helmholtz equation using a 2D finite-element approximation with triangular elements.

These methods are well validated for the treatment of linear waves. However, they do not take into account low-frequency nonlinearities. Apart from wind-generated waves, infragravity waves are present in coastal regions with wave periods on the wave-group scale. The total wave motion of incoming and outgoing infragravity waves produces a standing wave-like pattern. This phenomenon was first observed by Munk (1949) and Tucker (1950) who reported a correlation between incoming wave groups

and outgoing long waves with a certain time lag, approximately equal to the time for the swell to travel to the surf zone plus the time for a long wave to travel back to the wave recorder. Munk introduced the term "surf beat" to indicate these waves. In addition, Tucker found a (smaller) negative correlation at zero time lag. Biésel (1952) clarifies this negative correlation by the spatial changes of momentum flux associated with short-wave groups forming a wave which is 180° out phase with the short-wave envelope. Longuet-Higgins and Stewart (1962, 1964) describe that the gradients of momentum flux force the water away from the wave group forming a set-down underneath the group. Consequently a set-up is generated under lower waves. The set-down wave is bound to the wind-generated waves and travels shoreward with the group velocity of the short waves. The infragravity wave is released in the breaker zone as a free wave. The set-down wave grows substantially in the shoaling process which clarifies the larger correlation of the outgoing waves than of the incoming waves as observed by Tucker. See also Mei et al. (2005, Chapter 11) for a comprehensive overview of infragravity wave theory.

Another mechanism for infragravity wave generation is due to the temporal variation of the breakpoint (Symonds et al., 1982). Large waves in wave groups break earlier than small waves forcing a modulation of the offshore propagating free wave.

In case of oblique incident waves the outgoing infragravity waves refract more strongly than the incident short waves. If the angle of incidence of the short waves is small, the outgoing infragravity waves travel back to deep water as a leaky wave. If the angle of incidence is larger than a critical angle, the outgoing wave refracts back to the shore forming a trapped edge waves. Near-resonant edge waves result in large amplification of the infragravity waves at a certain angle of incidence. The edge-wave phenomenon has been observed by e.g. Huntley et al. (1981). Gallagher (1971) was able to give a theoretical explanation for edge-wave generation after making some crude assumptions. A more detailed analytical model was presented by Schäffer (1994) for an alongshore uniform beach. In most cases the total infragravity wave energy is a combination of leaky and edge waves due to directional spreading of the incident waves. Furthermore, edge waves can be generated in both alongshore directions due to interactions between wave components with different wave directions (Herbers et al., 1995).

Besides the trapped edge waves, a trapped wave can be generated in an open basin. Bowers (1977) showed theoretically that the natural oscillation of a harbour can be excited directly, without breaking of the primary wave system, by set-down beneath wave groups. When the period of the wave group is close to a natural period of the harbour, resonance will occur with the set-down behaving as if it were a free

long wave. Here the objectives of coastal and port engineering come together. It should be possible to use the same theories for the prediction of harbour oscillations due to wave-group forcing as for the computation of infragravity waves near a beach. A complete second order solution for a rectangular harbour with a narrow entrance and uniform water depth has been given by Mei and Agnon (1989) and Wu and Liu (1990). Similar approaches for arbitrarily shaped harbours are not available, which reduces the applicability for real ports.

Research on infragravity waves in coastal engineering has also led to some interesting solutions for the calculation of harbour oscillations due to wave group forcing. Roelvink (1993) developed the one-dimensional model SURFBEAT to calculate infragravity wave motions near a beach to clarify the shape of sand bars near the surf zone. This model has been extended to two dimensions (Reniers et al., 2000), which makes it suitable for the calculation of infragravity wave motions in a harbour or a sheltered bay (Van Giffen et al., 2003).

An appropriate way of treating first and higher order waves simultaneously is the use of Boussinesq-theory. Boussinesq-theory is used to reduce the three-dimensional flow problem to two-dimensional formulations. The vertical distribution of the velocity potential is approximated by a polynomial expansion. The classical Boussinesq equations (Peregrine, 1967) incorporate only weak dispersion and weak nonlinearity and in practice their range of applicability is limited to values of $kh < 0.75$, with k the wave number and h the mean water depth. Generally, the weak dispersion is most critical, because it affects the wave celerity, so that old Boussinesq models predict the right wave at the wrong place. Many improvements have been made over the last 15 years in terms of dispersion and nonlinearity as well as for flow kinematics and dynamics, the most considerable improvements being the use of Padé approximations for improved dispersion characteristics (Madsen et al., 1991), an expansion point at an arbitrary vertical level (most effectively around mid-depth; Nwogu, 1993), and the decoupling of the solution in a linear part in which the Laplace equation is expanded and a nonlinear part satisfying the exact boundary conditions at the bottom and the free surface (Agnon et al., 1999). Madsen et al. (2003) derived a new set of high-order equations which allows the correct modelling of nonlinear and extremely dispersive irregular waves up to $kh \approx 40$. Accurate velocity profiles are obtained for $kh < 10$. Fuhrmann et al. (2005) showed that this model can be used to directly determine the forces on a bottom-mounted surface-piercing structure. Such a highly nonlinear approach to calculate the wave forces on a structure is in some cases very useful, e.g. as high run-ups occur against a wall due to third order interaction between the incident and the reflected wave, if the width of the wall is of the same order as the

wave length (Molin et al., 2005).

Boussinesq equations do not only allow the modelling of sum and double-frequency nonlinearities, but the set-down beneath wave groups is treated correctly as well. This makes the models very useful for the calculation of low-frequency harbour oscillations induced by wave group forcing (Woo & Liu, 2004).

1.2.4 Moored ships in complex geometries

For the modelling of the behaviour of a moored ship in a harbour with a complex shape, the simulation techniques for wave penetration in the harbour and the interaction of waves with the ship need to be combined. In the first study on this subject, Sawaragi and Kubo (1982) introduced a single integrated method to calculate the motions of a ship, simplified as a rectangular box, in a rectangular harbour basin. The fluid domain is divided into three regions: (I) outside the harbour, (II) inside the basin and (III) underneath the ship. The problem is solved by deriving a Green function for each region, taking into account the conditions at the borders between the regions. The number of panels is reduced by applying the method of images in the rectangular basin. The excitation treated in that paper is due to ocean swells. Such a division into regions is also used by Ohyama and Tsuchida (1997). The wave field in the harbour with arbitrary shape and uneven bottom is computed with a 2D linear finite element model and the region around the ship is treated with a 3D boundary element model. First order wave theory is used to calculate the wave propagation into the harbour. However, the natural periods of harbour basins are much larger than the periods of swell waves.

A technique taking into account both the low-frequency harbour oscillations and the first order short waves has been developed by Kubo and Sakakibara (1997). They split the wave spectrum at wave period $T = 20$ s. The shorter waves are treated as progressive waves and the longer waves are treated as standing waves following from a calculation of harbour oscillations by a frequency-domain wave model.

Shiraishi et al. (1999) compared the results from four different hydrodynamical techniques to calculate the wave-ship interaction for a moored ship in a harbour and two different ways to treat the radiation damping. They compare the three-dimensional panel method combined with retardation functions for the radiation damping, as known from the analysis of the behaviour of a ship moored to an offshore jetty, with more simplified techniques. They conclude that an accurate description of the hull shape is necessary in case of slender ships such as container carriers. The simplified technique using a constant damping coefficient is inaccurate if the natural

period of the moored ship is far away from the significant wave period.

Another example of the usage of frequency-domain wave models has been described by Weiler and Dekker (2003). The standing wave acting on the ship is separated into two travelling waves taking into account the correct phase angle. The response is calculated using the wave force transfer functions for the two opposite wave directions and taking into account the presence of the quay wall.

A more sophisticated model than all methods described above has been developed by Bingham (2000). He describes a method combining a Boussinesq model to calculate the incident waves including the harbour geometry and bottom topography, but excluding the presence of the ship. The linear frequency-domain panel model WAMIT is used to calculate the hydrodynamic coefficients and the diffraction of the incident waves of which time-series are provided on each panel. In order to reduce the number of frequencies to be treated, the Haskind relations are used to obtain the forces due to the scattered waves. A similar approach has been described by Pinkster and Naaijen (2003) and Wenneker et al. (2006). They also obtain wave forces using a combination of a Boussinesq model and a linear frequency-domain panel model. However, they do not use the Haskind relations to obtain the diffraction forces, but all Fourier components are used, so that it is possible to describe the full flow distribution on the hull and it is possible to obtain the low-frequency varying drift forces as well. Disadvantage is the large number of frequency components. This is not a problem for the analysis of the effect of a passing ship which disappears after a few wave periods, but it is a drawback for the simulation of the ship's behaviour in an ocean storm.

In case of small sea ports the natural periods can be in the range of wave group periods. Bowers (1998) indicates that both the released bound waves and the surf beat are important for the generation of harbour oscillations in these small ports. The bound wave energy becomes free as the short waves diffract around a breakwater and this free wave can resonate in the harbour basin. Surf beat can play a role in harbour oscillations in the form of edge waves that are trapped in the shore zone due to oblique incident waves. These edge waves can diffract in the harbour basin and lead to resonance. Therefore, it is important to model not only the waves in the port, but also the waves in the shore zone close to the port entrance.

1.3 Research objectives

Existing methods for the calculation of wave penetration in a harbour either focus on short waves or on long waves. In the long-wave models the interaction between short

and long waves, or the generation and amplification of bound long waves associated with short-wave groups, is neglected. A proper method for low-frequency waves and ship motions in a harbour should have (1) the advantages of a long-wave model, e.g. a coarse grid and large time step, (2) it should include the interactions between short and long waves and (3) a correct coupling between long waves in the harbour and wave forces on the ship should be secured. This leads to the first objective.

More requirements need to be fulfilled if the berth is not located in a sheltered port, but more exposed to short waves, so that an approach based on first order wave forces is not sufficient. Present methods are either accurate for the determination of the waves at the berth and neglect drift forces or they focus more on second order forces, but assume a horizontal sea bed denying the facts that in shallow water the influences of refraction and enhancement of bound waves due to depth differences are important. The improved method should include the correct treatment of nonlinearities in the propagation of the incident waves over a topography and nonlinearities related to the interaction with the ship. Differently compared with the combined frequency and time-domain approach as described by Pinkster and Naaijen (2003) and Wenneker et al. (2006), a fully time-domain method is investigated in this thesis, so that straightforward and direct links are secured between the subsequent model components. This leads to the second objective.

The objectives in this thesis are to develop and validate two computational methods for wave interaction with a ship moored in shallow water:

- A method with the focus on long-period ship response, either forced by free long waves or forced by long waves associated with wave groups at the ocean. The wave force formulations should be independent on the wave direction, so that wave forces can be determined directly in an irregular multi-directional wave field in a harbour. This is an adequate approach in case of a berth which is sufficiently sheltered for short waves, but is exposed to long waves or harbour oscillations.
- A method for moored ship motions in an arbitrarily shaped harbour which includes both forcing due to first order waves and second order effects associated with bound long waves and drift forces. The focus is on developing a fully time-domain model. Besides the validation against model test experiments, the results of the fully time-domain method are compared with a combined time and frequency-domain method.

1.4 General approach

A sufficiently accurate but still practicable solution must have the advantages of an advanced wave model, which includes refraction in shallow water, diffraction around breakwaters and reflection against walls. Furthermore, it must include a correct description of the hull shape and the diffraction around the hull. Thus, accurate descriptions are required for both the sea floor and the ship's hull. These two demands are difficult to combine in a single computer model. Therefore, the solutions discussed in this thesis are combinations of simulation methods. The advantage is that the strong points of each model are utilized. The general modelling procedure consists of the following steps (also schematized in Figure 1.2): (1) the waves throughout the harbour are calculated not taking into account the presence of the moored ship, because it is difficult to treat the exact 3D shape of the hull in such a large-scale model; (2) the diffraction around the hull is calculated taking into account the 3D shape of the hull and the interaction of the diffracted wave with nearby structures, such as a quay wall; (3) the ship motions are simulated due to the wave forcing, taking into account the characteristics of the mooring system, radiation damping and viscous damping.

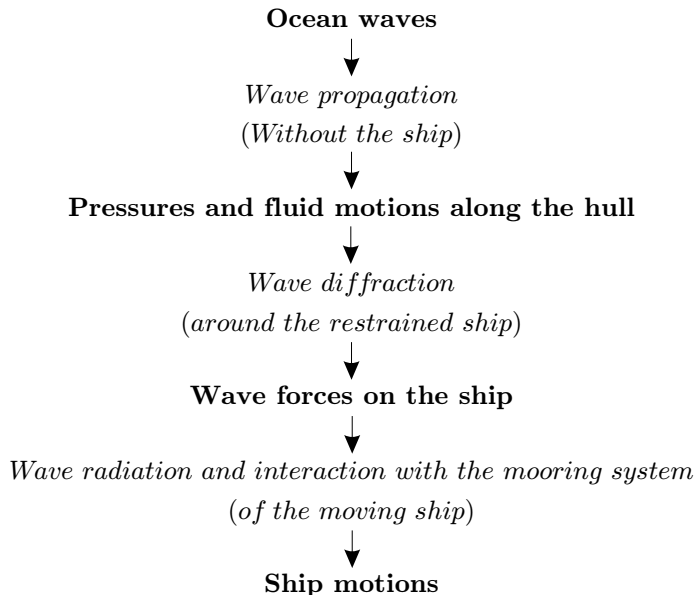


Figure 1.2: Flow diagram of the simulation process for a moored ship in a port.

1.5 Outline of the thesis

Two solutions are presented in this thesis consisting of a combination of a wave propagation model and a method to obtain the wave forces on the ship:

1. an infragravity wave model and a strip theory method;
2. a Boussinesq-type wave model and a boundary-integral method.

The two methods fulfill the subsequent research objectives. The first combination only treats the moored ship behaviour in long waves. In most cases the wave motions in the harbour are dominated by long waves and a long-wave analysis would be sufficient. Consequently, it is possible to include a large coastal area in the calculation and a long simulation time can be adopted. The second combination treats all nonlinear characteristics of surface waves. Therefore it is possible to achieve more accurate results, only at higher computational costs.

The method for long-period ship motions in a harbour is described in Chapter 3 together with a comparison with model test experiments for a container ship, described in Chapter 2, and prototype measurements of long waves and ship motions obtained during a typhoon in Tomakomai Port, Japan. Chapters 4 through 6 deal with the description and validation of the Boussinesq/boundary-integral approach. The method is described in Chapter 4; a first validation of the boundary-integral model for a tanker in open water and a container ship in a harbour is provided in Chapter 5 and the validation of the model chain is given in Chapter 6, where the calculations for a container ship are compared with the model tests. Finally, conclusions are drawn and recommendations are made about possible improvements of the calculation methods.

2. MODEL TESTS

2.1 Test set-up

To validate the computational methods to calculate the behaviour of a moored ship in a harbour, model tests have been carried out in the directional wave basin of WL|Delft Hydraulics with a modelled uniform water depth of 20 m (see Figure 2.1). The tests were performed on a Panamax container ship at a model scale of 1:100. All dimensions are provided here on prototype scale using Froude scaling. The dimensions of the ship are given in Table 2.1; the body plan is given in Figure 2.4. The ship was fixed to its position by a large steel frame (see Figure 2.2). Six force transducers were fitted in this frame to measure the forces on the ship in the six degrees of freedom. This has been done to avoid the difficult treatment of springs to model the behaviour of mooring lines in the tests and since the objective of the experiments is to validate the wave propagation in shallow water and the subsequent forces on the moored ship. The last step in the modelling chain, the simulation of ship motions excited by the wave forces, is rather straightforward. In other words, for validation purposes it is sufficient to model the wave forces only, and the difficulty in representing the mooring lines in a physical model can therefore be discarded. Nevertheless, it should be considered that the representation of the low-frequency wave forces is critical for the correct modelling of the horizontal ship motions.

For the tests of the ship in the harbour, a simple rectangular open basin was created with a length of 1200 m (see Figure 2.3). The ship is situated in the middle of the basin, close to one of the walls. Wave elevations were measured with three wave gauges close to the wavemaker (WG1-3) and with five wave gauges in the harbour basin (WG4-8).

To specify the wave directions a global coordinate system is used with the origin at the wavemaker, the y-axis directed into the basin and perpendicular to the wavemaker. The harbour basin and the ship are placed under an angle of 210° with respect to the global coordinate system.

The wavemaker in the basin consists of a large number of piston type paddles



Figure 2.1: Model test set-up

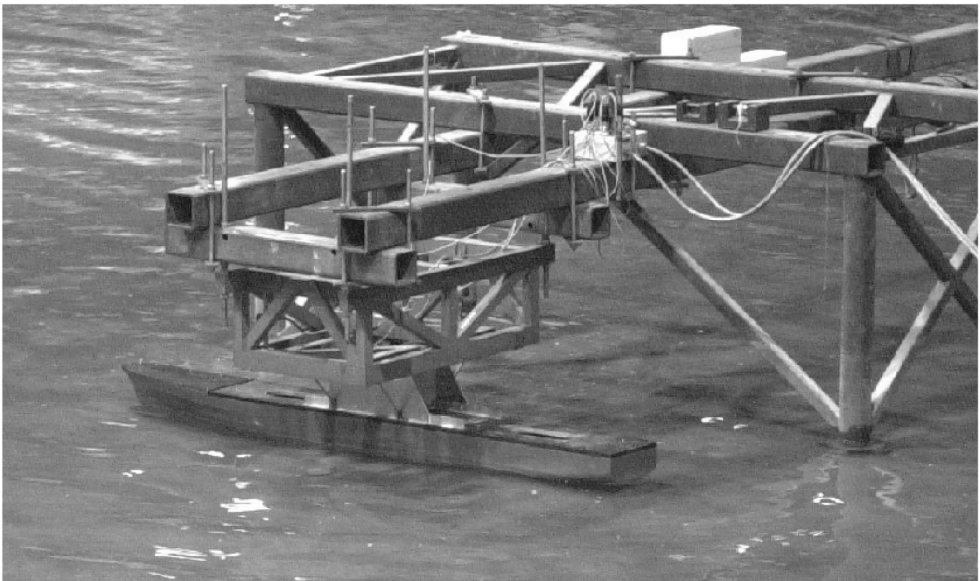


Figure 2.2: The model ship with the force frame

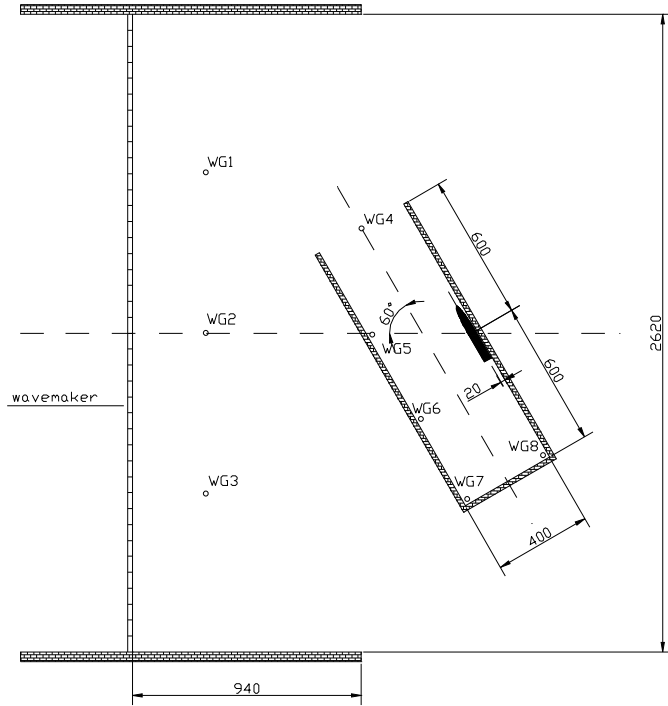


Figure 2.3: Layout of the test basin

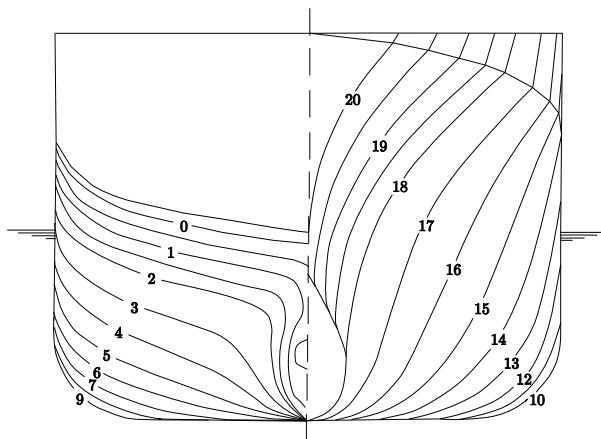


Figure 2.4: Body plan of the Panamax container ship

Table 2.1: Dimensions of the Panamax container ship

Designation	Symbol	Unit	Magnitude
Length between perpendiculars	L_{PP}	m	255.00
Breadth	B	m	32.26
Depth	D	m	25.00
Draft	d	m	12.00
Displacement volume	Δ	m ³	58,660
Centre of buoyancy forward of station 10	LCB	m	-6.37
Centre of gravity above keel	\overline{KG}	m	13.50
Transverse metacentric height	\overline{GM}	m	1.50
Transverse radius of gyration	k_{xx}	m	12.40
Longitudinal radius of gyration	k_{yy}	m	69.25
Longitudinal radius of gyration	k_{zz}	m	70.35
Natural heave period	T_z	s	10.60
Natural roll period	T_φ	s	22.80
Natural pitch period	T_θ	s	9.20

which are able to move independently. In this fashion waves can be generated in all directions including directional spreading. The second order long waves are included in the waveboard control signals to produce the correct wave motions in the basin up to second order and avoid otherwise generated spurious long waves (Sand, 1982a). The available model area in oblique waves is increased by applying the side wall reflection method, based on Dalrymple (1989), which uses the side wall to generate a wave train at a specified location. Furthermore the waveboard is equipped with active reflection compensation (Van Dongeren et al., 2001). With this method any reflected waves from the basin are absorbed at the waveboard and thus the generation of oscillations in the laboratory basin is reduced. The routine uses the surface elevations measured by a waveboard mounted gauge and full-spectrum linear theory to estimate the reflected wave and compute a real-time correction signal to the waveboard motion.

2.2 Test program

The tests consisted of several series for different conditions:

1. extinction tests of the ship in open water;
2. waves and forces on the ship in open water;

3. extinction tests of the ship in the harbour basin;
4. waves and forces on the ship in the harbour basin;
5. waves in the harbour basin without the ship;
6. waves in open water without the ship.

The extinction tests were performed to verify whether the natural frequency of the ship connected to the frame was well outside the frequencies of the incident waves for the tests in waves. If the natural frequency would be too close to the wave frequency, resonance of the ship would affect the measured forces on the ship. The natural frequencies should be much higher than the wave frequency, so that the ship can be regarded as restrained to its position in all test series.

The tests in waves consisted of series of regular waves, irregular long-crested waves and irregular short-crested waves. In each case several tests were performed for different (peak) wave periods and (mean) wave directions. The conditions for the tests in open water and in the harbour are given in Tables 2.2 and 2.3 respectively. The wave directions are given with respect to the wavemaker in the global coordinate system. The same conditions are applied for the tests with and without the ship in the harbour, so that the conditions for test series 5 and 6 are equal to the conditions of series 4 and 2 respectively. For the tests without the ship an array of six wave gauges was placed at the position of the ship, including a wave gauge combined with a current gauge at the position of the centre of gravity of the ship. These tests without the ship are important in the validation process, so that it can be verified whether differences between measurements and calculation occur due to the determination of the incident waves or due to the waves diffracted by the ship.

Apart from the tests to model sea waves, tests have been carried out for the waves generated by a passing ship. For these tests the passing ship is not modelled as a real ship, but it is mimicked by the waveboard motion. The independent waveboard steering can be used to simulate a moving object. By letting each paddle make one forward and backward movement one after another, a moving bulge is created. The moving bulge generates waves similar to the waves generated by a passing ship, obviously only at one of the symmetric sides of the ship. Two conditions have been tested for a passing ship simulated in this way: a subcritical speed of 12 m/s ($F_n = 0.86$) and a supercritical speed of 21 m/s ($F_n = 1.5$), where the Froude number is defined as $F_n = V_s/\sqrt{gh}$ with V_s the speed of the passing ship. The ship passes from right to left viewed from the left-hand side in Figure 2.3. A closer look reveals that this is not a very accurate representation of a realistic passing ship event, especially

Table 2.2: Conditions for the tests with the ship in open water

Test N ^o	γ ¹⁾	$S(\theta) \sim$ ²⁾	H_s [m]	T_p [s]	θ_0 [°]
2.1.1	∞	$\delta(\theta)$	1	10	90
2.1.2	∞	$\delta(\theta)$	2	10	90
2.1.3	∞	$\delta(\theta)$	1	10	60
2.1.4	∞	$\delta(\theta)$	2	10	60
2.2.1.1	3.3	$\delta(\theta)$	1.5	7	90
2.2.1.2	3.3	$\delta(\theta)$	1.5	10	90
2.2.1.3	3.3	$\delta(\theta)$	1.5	15	90
2.2.2.1	3.3	$\delta(\theta)$	1.5	7	60
2.2.2.2	3.3	$\delta(\theta)$	1.5	10	60
2.2.2.3	3.3	$\delta(\theta)$	1.5	15	60
2.3.1.1	3.3	$\cos^2 \theta$	1.5	7	90
2.3.1.2	3.3	$\cos^2 \theta$	1.5	10	90
2.3.1.3	3.3	$\cos^4 \theta$	1.5	10	90
2.3.1.4	3.3	$\cos^4 \theta$	1.5	15	90
2.3.2	3.3	$\cos^4 \theta$	0.5	15	60
2.4 ³⁾	3.3	$\cos^2 \theta$	1.5	7	60
	3.3	$\cos^4 \theta$	0.5	15	60
2.5.1		Passing ship: $V_s = 12$ m/s			
2.5.2		Passing ship: $V_s = 21$ m/s			

¹⁾ Gamma parameter in the JONSWAP spectrum; $\gamma = \infty$ means regular waves.

²⁾ Shape of the directional spectrum; $S(\theta) \sim \delta(\theta)$ denotes uni-directional waves.

³⁾ This test represents combined sea and swell.

Table 2.3: Conditions for the tests with the ship in the harbour basin

Test N ^o	γ	$S(\theta) \sim$	H_s [m]	T_p [s]	θ_0 [°]
4.1.1	∞	$\delta(\theta)$	2	10	90
4.1.2	∞	$\delta(\theta)$	2	10	120
4.2.1.1	3.3	$\delta(\theta)$	3	10	90
4.2.1.2	3.3	$\delta(\theta)$	3	15	90
4.2.2.1	3.3	$\delta(\theta)$	3	10	120
4.2.2.2	3.3	$\delta(\theta)$	3	15	120
4.2.3.1	3.3	$\delta(\theta)$	6	10	120
4.2.3.2	3.3	$\delta(\theta)$	6	15	120
4.3.1.1	3.3	$\cos^2 \theta$	3	10	90
4.3.1.2	3.3	$\cos^2 \theta$	3	15	90
4.3.2.1	3.3	$\cos^2 \theta$	3	10	120
4.3.2.2	3.3	$\cos^2 \theta$	3	15	120
4.3.3.1	3.3	$\cos^4 \theta$	3	10	120
4.3.3.2	3.3	$\cos^4 \theta$	3	15	120
4.4.1		Passing ship: $V_s = 12$ m/s			
4.4.2		Passing ship: $V_s = 21$ m/s			

for the case of a supercritical speed. The passing ship is rather large (in reality only small vessels move at supercritical speeds) and the paddles displace water uniformly over the depth (while the vessel has a limited draft in reality). These effects will lead to wave heights that are much larger than to be expected in reality. Nevertheless, the tests are interesting for validation. The initial condition is an undisturbed free surface. The only disturbances are at the wavemaker and due to the limited simulation time there are no influences from the boundaries of the laboratory basin other than the wavemaker and the short sidewalls. Moreover, the waves due to a passing ship are highly dispersive.

2.3 Discussion on the measurements

A summary of the results of the tests with the ship in the harbour basin is given in Appendix A. Further elaborated results are given together with computational results in Sections 3.3, 3.4, 5.2 and 6.1 for the tests that are most interesting for validation. The main considerations on the results of the experiments are discussed here.

Physical modelling of waves in shallow water is difficult, especially if the interest is mainly on the modelling of low-frequency waves. Despite the fact that the basin is equipped with the active reflection compensation method, it is difficult to eliminate all spurious effects. Moreover, in these experiments the harbour basin is rather long compared with the basin width, so that a large part of the long-wave energy reflects against the harbour walls and returns to the wavemaker. The reflected wave is compensated at the waveboard, but it cannot be fully absorbed, especially if the reflected waves are obliquely incident on the wavemaker. The reflected wave from the wavemaker affects the measured long-wave signals in the harbour basin. For the measurements in open water, the reflected long-wave energy from the far side of the laboratory basin is much smaller. The effect is also expected to be small for the short waves, because the reflected waves are much lower than the incident waves due to breaking of short waves against the slope on the outside of the harbour basin, so that small errors in the reflection compensation do not lead to significant errors in the basin.

Although the ship connected to the force frame can be considered as almost fully stiff, small measurement errors can occur in the determination of the forces on the ship. These errors are small regarding the force measured in a single force transducer. Nevertheless, problems occur in the correct measurement of the roll forces. The roll force is determined as the difference in vertical force between starboard side and port side of the ship plus a moment due to the fact that horizontal forces are measured

above the centre of gravity of the ship. Considering a restrained ship in waves, the heave forces are large if the wave length is much longer than the width of the ship. Because the roll force is mainly measured as the difference between two vertical forces, the relative error in the roll forces is much larger than the error in the measured heave forces. This error is also observed for pitch, but because the pitch forces are normally much larger than the roll forces, the relative error is much smaller.

In the validation of the calculations a comparison is made for forces in all six degrees of freedom, but for the analysis of roll forces it is allowed for the fact that the measured roll forces differ from the real forces. It is expected that the measured roll forces are larger, because unintended forces due to small measurement errors are added.

3. MOORED SHIP RESPONSE IN LONG WAVES: MODEL AND VALIDATION

3.1 Introduction

Long waves in the range of periods from 30 to 300 seconds are important for analysing moored ship motions, because the natural periods of horizontal ship motions are also in this range of periods. In many cases for a ship moored in a harbour it may even be sufficient to neglect the short waves at the berth location and only treat the response due to long waves. An approach fully describing the short and long waves might then be too costly and it is more convenient to focus on the long waves. In this Chapter a method is presented to obtain the long-period motions of a moored ship in a harbour using an infragravity wave model. There is a clear distinction between the treatment of long and short waves, which are divided at a certain split frequency. The long waves are calculated in the time-domain using classical shallow water equations. The model considers the directionally-spread short-wave energy, associated with wave groups, propagating shoreward with the wave group celerity along precalculated mean wave directions. Because no phase information is required for the short waves, but only for the variations of wave energies, the grid can be based on the long-wave motions. Thus, a much coarser grid is sufficient compared with models fully describing the profile of the short waves. This makes the model especially suitable for relatively sheltered harbour basins in which the wave motion is dominated by infragravity waves.

The presence of the moored ship is not taken into account in the wave model directly. The calculated surface elevations and particle motions at the locations of a number of cross-sections along the ship's hull are used to determine the wave forces on the ship. These wave forces are the exciting forces in the simulation of ship motions taking into account the nonlinear behaviour of fenders and mooring lines and radiation and viscous damping.

In this Chapter the model formulations are given in Section 3.2. The model is validated against the model test experiments described in Chapter 2 (Sections 3.3

and 3.4) and prototype measurements (Section 3.5). Numerical results are given for a ship moored in open water close to the coast in Section 3.6. The latter results are given to show the competence of the method in more exposed conditions where a considerable amount of long-wave energy is still bound to the short waves. In these cases it is also possible to determine the low-frequency wave forcing. However, unlike the approach based on a Boussinesq-type wave model the first order forces and drift forces associated with the first order solution are not determined directly, so that they must be added explicitly.

3.2 Model description

3.2.1 Infragravity wave model

For the calculation of infragravity wave penetration in the harbour, the 'Surfbeat' module (Reniers et al., 2000, 2004) in Delft3D as developed at WL|Delft Hydraulics is used. The model formulations are presented here following Reniers et al. (2004). The model incorporates a 2D energy propagation and dissipation model for the short waves to force the long waves, which are solved using nonlinear shallow water equations. The short-wave directions θ , along which the wave energy is 'transported', are calculated with the spectral wave model SWAN (Booij et al., 1999). The balance for the short-wave energy E_w is given by:

$$\frac{\partial E_w}{\partial t} + \frac{\partial E_w c_g \cos \theta}{\partial x} + \frac{\partial E_w c_g \sin \theta}{\partial y} = -D_w \quad (3.1)$$

where c_g represents the group velocity associated with the peak period. The wave energy dissipation D_w represents the dissipation due to breaking which is calculated using the formulation of Roelvink (1993):

$$D_w = 2\alpha f_p E_w \left[1 - \exp \left[- \left(\frac{E_w}{\gamma_b^2 E_{\text{ref}}} \right)^{\frac{n}{2}} \right] \right] \quad (3.2)$$

with

$$E_{\text{ref}} = \frac{1}{8} \rho g D^2 \quad (3.3)$$

where α is a coefficient representing the deviation of the wave height distribution from the Raleigh distribution, f_p the peak frequency, γ_b a wave breaking parameter or the ratio between the wave height and the water depth in the surf zone and n is a dissipation parameter corresponding to the randomness of the incident waves.

ρ is the density of the fluid and g is the acceleration of gravity. The water depth D represents the total time-dependent water depth including the effects of setup and the infragravity surface elevation. Roelvink suggests the following values for the coefficients obtained by model test calibration: $\alpha = 1.0$, $\gamma_b = 0.55$ and $n = 10$. The value of γ_b can decrease to about 0.35 for very gentle bottom slopes (Battjes & Groenendijk, 1999).

Wave energy released at wave breaking is first transferred to roller energy prior to dissipation into heat, causing a spatial lag between the location of wave breaking and the actual dissipation. The roller energy is the kinetic energy in the broken wave.

The process described above is used for waves incident on a beach. The short waves brake gradually on the beach. The infragravity wave is released during the breaking process, reflects at the shore and travels back offshore. All short-wave energy is released during breaking and the infragravity wave energy remains. In case of waves incident on a wall or a breakwater, there is no gradual breaking process. It is assumed in the model that all short-wave energy is released immediately during breaking against the wall. The infragravity wave is released and fully reflects against the wall.

The free infragravity wave can either leak to deeper water or be refractively trapped to the shore zone. These edge waves influence the infragravity motions near a harbour entrance if it is located close to a beach coast. Therefore, the correct modelling of infragravity waves outside the harbour improves the calculation of harbour oscillations.

The infragravity flow is solved using nonlinear shallow water equations forced by the short-wave radiation stresses. These equations consist of the continuity equation:

$$\frac{\partial \zeta}{\partial t} + \frac{\partial Du}{\partial x} + \frac{\partial Dv}{\partial y} = 0 \quad (3.4)$$

and the momentum equations:

$$\frac{\partial u}{\partial t} + u \frac{\partial u}{\partial x} + v \frac{\partial u}{\partial y} = -\frac{F_x}{\rho D} - g \frac{\partial \zeta}{\partial x} + \nu_t \left(\frac{\partial^2 u}{\partial x^2} + \frac{\partial^2 u}{\partial y^2} \right) - \frac{\tau_x}{\rho D} \quad (3.5)$$

$$\frac{\partial v}{\partial t} + u \frac{\partial v}{\partial x} + v \frac{\partial v}{\partial y} = -\frac{F_y}{\rho D} - g \frac{\partial \zeta}{\partial y} + \nu_t \left(\frac{\partial^2 v}{\partial x^2} + \frac{\partial^2 v}{\partial y^2} \right) - \frac{\tau_y}{\rho D} \quad (3.6)$$

where ζ is the infragravity wave elevation, u and v are the infragravity wave velocities in the x - and y -direction respectively and \vec{F} is the wave-induced forcing. The second term in the righthand side represents the hydrostatic pressure gradient, the third term the turbulent lateral mixing proportional to the kinematic turbulent eddy viscosity

ν_t , which is related to wave breaking, and $\vec{\tau}$ represents the nonlinear combined short-wave and current bottom shear stress. The wave- and roller-induced forces F_x and F_y are defined as:

$$F_x = \frac{\partial S_{xx}}{\partial x} + \frac{\partial S_{yx}}{\partial y} \quad (3.7)$$

$$F_y = \frac{\partial S_{xy}}{\partial x} + \frac{\partial S_{yy}}{\partial y} \quad (3.8)$$

where \mathbf{S} represents the short-wave radiation stresses varying at the wave group scale, forcing the infragravity waves. The radiation stresses are obtained from linear wave theory including the roller contribution:

$$S_{xx} = \left(\frac{c_g}{c} (1 + \cos^2 \theta) - \frac{1}{2} \right) E_w + 2E_r \cos^2 \theta \quad (3.9)$$

$$S_{xy} = E_w \frac{c_g}{c} \cos \theta \sin \theta + 2E_r \cos \theta \sin \theta \quad (3.10)$$

$$S_{yy} = \left(\frac{c_g}{c} (1 + \sin^2 \theta) - \frac{1}{2} \right) E_w + 2E_r \sin^2 \theta \quad (3.11)$$

where E_r is the kinetic roller energy in the breaking wave.

The short-wave energy as input at the boundary is obtained using a large number of wave components based on a given frequency-directional wave spectrum. The envelope of the short-wave time series is taken using the Hilbert Transform and applying a low pass filter to obtain variations at the wave group scale. From the short-wave energy variations the associated bound wave can be found. Details of this procedure are described in Van Dongeren et al. (2003). In addition, free long waves (the components below the split frequency) can be specified at the boundary. In the infragravity frequency band, the wave motions therefore consist of bound and free components.

3.2.2 Wave force formulations

For the calculation of ship motions the time-domain simulation model BAS (Mynett et al., 1985) is used. It solves the equation of motion of the ship, which is given by

$$(\mathbf{M} + \mathbf{A})\ddot{\vec{X}}(t) + \mathbf{B}_v \dot{\vec{X}}(t) \left| \dot{\vec{X}}(t) \right| + \mathbf{C}\vec{X}(t) + \int_0^\infty \mathbf{K}(\tau)\vec{X}(t-\tau)d\tau = \vec{F}(t) \quad (3.12)$$

where \mathbf{M} is the inertia matrix, \mathbf{A} is the matrix containing the added mass coefficients, \mathbf{B}_v contains the low-frequency viscous damping coefficients, \mathbf{C} the hydrostatic spring coefficients, \mathbf{K} the retardation functions containing the effect that the body oscillation

is damped due to waves radiating away from the body, \vec{X} represents the ship motion in six degrees of freedom and \vec{F} the exciting forces due to waves, current and wind and the forces in fenders and mooring lines. The hydrodynamic coefficients A_{kj} , C_{kj} and $K_{kj}(t)$ are calculated using the frequency-domain panel model DELFRAC (Pinkster, 1995) with the possibility of considering the influence of a quay wall. The exciting wave force is the force acting on the restrained ship in waves. For the calculation of wave forces on the ship, a strip theory approach is used. Within strip theory the ship is divided into a typical number of 20 cross-sectional strips. The force is calculated for each cross-section separately, F'_k , and then integrated over the ship length L to provide the total wave force

$$F_k = \int_L F'_k dx_s, \quad k = 1, 2, \dots, 6 \quad (3.13)$$

where x_s is the x -position of the cross-section in the ship-bound coordinate system $Oxyz$ with the origin at still water level above or below the ship's centre of gravity, the x -axis directed towards the bow and the z -axis positive upwards. The long-wave assumption is used in the formulations of the wave force. The horizontal fluid motions are considered constant over water depth and the pressure is hydrostatic. Because the infragravity waves are much longer than the dimensions of the cross-section, the slope of the free surface and the horizontal particle velocities and accelerations are assumed to be constant over each cross-section. With this assumptions the Froude-Krylov forces due to the incident undisturbed wave for surge, sway, heave and roll are simply equal to the integration of hydrostatic forces over the submerged hull surface:

$$F'_{1,FK}(t) = -\rho g \frac{\partial \zeta}{\partial x}(t) \cdot A_x \quad (3.14)$$

$$F'_{2,FK}(t) = -\rho g \frac{\partial \zeta}{\partial y}(t) \cdot A_x \quad (3.15)$$

$$F'_{3,FK}(t) = \rho g \zeta(t) \cdot b_s \quad (3.16)$$

$$F'_{4,FK}(t) = \rho g \frac{\partial \zeta}{\partial y}(t) \cdot \left(\frac{b_s^3}{12} - \overline{bG} \cdot A_x \right) \quad (3.17)$$

where A_x is the cross-sectional area, b_s is the sectional breadth and \overline{bG} is the vertical distance between the cross-sectional centre of buoyancy and the ship's centre of gravity. The force due to the disturbance of the incident wave by the presence of the ship is calculated using the relative motion principle, supported by the Haskind relations. This principle states that the force on a fixed body due to an oscillating fluid is equal to the force due to an oscillating body in still water. The diffraction forces

can then be determined by taking the product of fluid oscillations and hydrodynamic coefficients. Because of the frequency dependence of these coefficients, the Fourier transforms of the fluid velocities, \tilde{u} , \tilde{v} and $\tilde{w} = i\omega\tilde{\zeta}(z+h)/h$ and the accelerations, $\ddot{u} = i\omega\tilde{u}$, $\ddot{v} = i\omega\tilde{v}$ and $\ddot{w} = i\omega\tilde{w}$, are used in the formulations for the diffraction part of the wave forces in long waves:

$$F'_{1,d}(t) = \int_0^\infty [i\omega m'_{11}(\omega) + n'_{11}(\omega)] \tilde{u}(\omega) e^{i\omega t} d\omega \quad (3.18)$$

$$F'_{2,d}(t) = \int_0^\infty [i\omega m'_{22}(\omega) + n'_{22}(\omega)] \tilde{v}(\omega) e^{i\omega t} d\omega \quad (3.19)$$

$$F'_{3,d}(t) = \int_0^\infty [-\omega^2 m'_{33}(\omega) + i\omega n'_{33}(\omega)] \tilde{\zeta}(\omega) e^{i\omega t} d\omega \left(1 - \frac{d_{s,\text{rep}}}{h}\right) \quad (3.20)$$

$$F'_{4,d}(t) = \int_0^\infty [i\omega m'_{42}(\omega) + n'_{42}(\omega)] \tilde{v}(\omega) e^{i\omega t} d\omega + F'_{2,d}(t) \cdot \left(z_G + \frac{d_s}{2}\right) \quad (3.21)$$

where m'_{kj} and n'_{kj} are the cross-sectional added mass and damping coefficients respectively, z_G is the z -position of the centre of gravity, d_s is the sectional draft and $d_{s,\text{rep}}$ is a representative draft where the heave diffraction force is assumed to act. The cross-sectional hydrodynamic coefficients are estimated from the full body coefficients as obtained by DELFRAC and an approximation based on the added mass coefficients of a Lewis cross-section in deep water at zero-frequency (Journée & Adegest, 2003). The latter is only used for determination of the *distribution* of the coefficients over the ship length. The coefficients are distributed in such a way that the full body coefficients obtained by integrating the sectional values over the ship's length are equal to the DELFRAC values, which includes the influence of bottom effects and an accurate description of the hull shape. The optimization of the cross-sectional added mass is carried out to satisfy the full body added mass coefficients a_{11} for surge; a_{22} , a_{62} and a_{66} for sway; a_{33} , a_{53} and a_{55} for heave and a_{42} and a_{46} for roll. The cross-sectional damping is optimized to satisfy the full body damping coefficients b_{kj} for the same combinations of k and j .

The wave forces for pitch and yaw using strip theory follow from the calculated values for surge, sway and heave:

$$F'_5(t) = -F'_1(t) \cdot \overline{bG} - F'_3(t) \cdot x_s \quad (3.22)$$

$$F'_6(t) = F'_2(t) \cdot x_s \quad (3.23)$$

Thus, a set of formulations has been derived to obtain the wave force without in-

formation on the wave directions which are difficult to determine in an irregular standing wave pattern inside a harbour. The surface elevations and the particle velocities are the values computed with Surfbeat at the location of the midpoint of the cross-section. The free surface gradients are easily obtained with linear interpolations between nearby grid cells of Surfbeat. The problem if the ship is very close to the boundary, such as a quay wall, is solved by mirroring the wave profile in the boundary, so that gradients can be obtained with free surface elevations at the land-side of the boundary.

3.3 Results for a container ship in open water

In order to validate the method to obtain the wave forces on the ship, computational results are compared with model test results from the tests as described in Chapter 2 for a container ship in open water in irregular waves. Because the wave force formulations are limited to long waves, comparison is only made for long swell waves. The wave spectrum is a uni-directional JONSWAP spectrum with directions $\theta = 210^\circ$ and 240° in the ship-bound coordinate system which correspond to the conditions of tests 2.2.2.3 and 2.2.1.3 respectively. These waves can almost be considered as long waves.

To obtain time-series of surface elevations at the locations of the cross-sections of the ship, the waves measured at the wave gauges close to the wavemaker are taken and the propagation towards the ship is calculated using linear wave theory. The test with uni-directional waves is therefore chosen, so that time-series of waves can be generated at each cross-section. To account for the non-hydrostatic pressure and depth-varying particle velocities, the terms in the wave force formulations are not taken at the fluid surface, but at the section's buoyancy point. The results for the two different wave directions are given in Figure 3.1. The calculated wave forces are in good correspondence with the measured forces, especially for surge and pitch. Small differences are observed for sway and yaw, because of the depth-varying velocity profile which leads to small errors in the diffraction loads. These diffraction effects are much smaller for the symmetric modes surge, heave and pitch. The differences for roll are mainly due to measurement errors.

3.4 Results for a container ship in a harbour basin

To validate the combination of the infragravity wave model Surfbeat and the strip theory method to calculate the wave forces, computational results are compared with

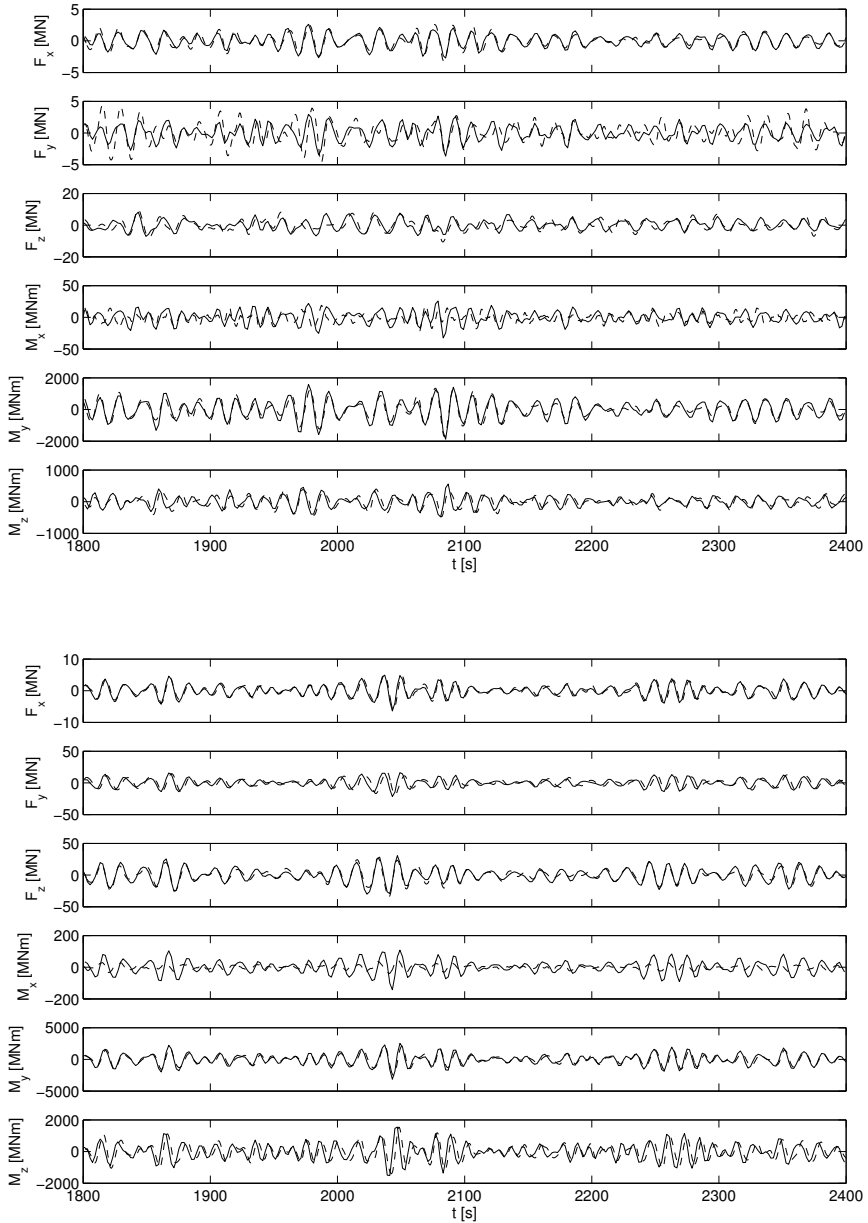


Figure 3.1: Comparison of wave forces in open water; $H_s = 1.5$ m, $T_p = 15$ s, $\theta = 210^\circ$ (top) and 240° (bottom); -- measurements, — strip theory

model test results as described in Chapter 2 for a container ship in a rectangular harbour basin. Test 4.2.3.1 is used here for comparison which comprises uni-directional irregular waves, $H_s = 6$ m, $T_p = 10$ s, $\theta = 120^\circ$ from the wavemaker, which is perpendicular to the harbour axis. These conditions are selected, so that there is a considerable amount of infragravity wave energy, which is proportional to the wave height squared. Furthermore, the wave action in the harbour basin is more or less dominated by long waves; most short-wave energy travels past the harbour entrance, but the long waves can still diffract and amplify in the harbour. Such a situation is required, because the calculation model is suitable for situations where the wave action in the harbour is dominated by long waves. The measured significant wave height at the rear of the harbour (WG8) is 2.46 m for the short waves and 1.10 m for the long waves, with the split frequency chosen at $\omega = 0.3$ rad/s. The height of the long waves is of the same order as the short-wave height. Therefore, inside the harbour most long-wave energy is free wave energy which is also assumed in the calculation.

The model domain is rectangular with the orientation of the grid perpendicular and parallel to the wavemaker in the laboratory basin. The domain consists of 86×131 grid cells of 23.09×20 m² each. The walls of the harbour basin are modelled as fully absorbing for the short waves and fully reflecting for the long waves. The boundaries opposite of the wavemaker and at the left-hand side next to the side walls are open boundaries in the calculation. Thus, reflections from the far side of the laboratory basin are neglected. To prevent too much reflections against the side wall with the oblique wave direction, the wave paddles close to the side wall at the left-hand side of the wavemaker are not used. In the calculation this part of the wavemaker is assumed as a closed boundary. The remainder of the waveboard is assumed as an open boundary where reflected waves are able to travel out of the model domain. In the model tests the active reflection compensation method is equipped at the whole waveboard. However, in this case with a large amount of reflected wave energy with different directions it is difficult to diminish all reflected waves.

An overview of the significant wave heights of short and long waves is given in Figure 3.2. The short-wave heights are obtained from the time series of wave energies in Surfbeat and the long-wave heights from the time series of surface elevations. The wave energies travel along the wave rays obtained with SWAN. Although diffraction is included (with some assumptions) in the SWAN calculation and therefore the correct wave directions are obtained in the area near the harbour entrance, a fully correct diffraction pattern of the short waves is not observed. Nevertheless, because the distance over which the diffraction takes place is fairly small, the influence on the

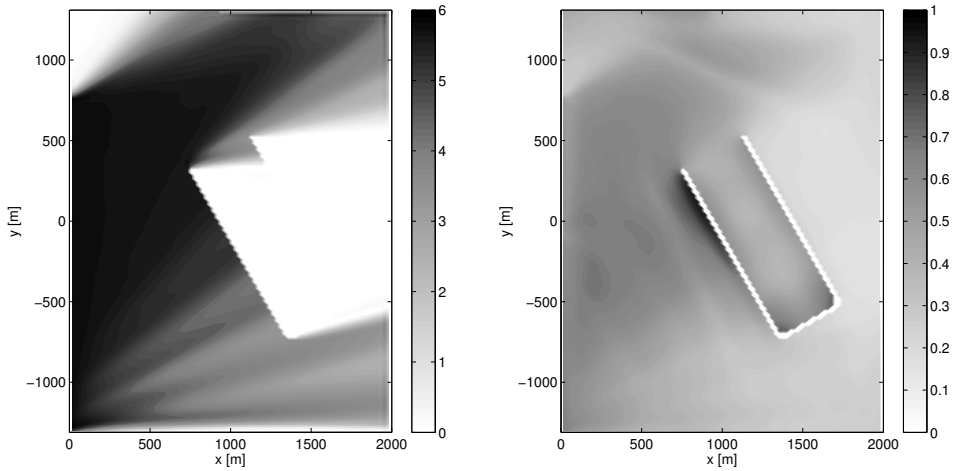


Figure 3.2: Calculated significant wave heights [m] of short waves (left) and long waves (right) in the laboratory basin.

long-wave propagation is also small. The long waves passing the entrance of the harbour are mainly bound to the wave groups. At the sides of a wave group a free wave is generated due to water level gradients transverse to the wave direction. The generation of such a free wave is the driving force for the amplification in the harbour: the bound wave itself does not diffract in the harbour, because it remains bound to the short waves, but the water level gradients directed into the harbour generate waves in that direction.

The measured and calculated wave spectra are given in Figure 3.3 at two locations: in the corner of the harbour (WG8) and at the position of the centre of gravity of the ship. Only the low-frequency part of the spectrum is given. The measured waves also show a pattern of standing short waves, although much smaller than the waves outside the harbour basin, because most wave energy travels along the harbour mouth. The peak frequencies corresponding to natural modes of the harbour are given in Table 3.1 together with theoretical values. The correspondence at the first natural mode of the harbour is quite good. The measured and simulated resonant frequency for the first mode is a little larger than the theoretical value because of the effect of the side wall of the laboratory basin. The calculated frequencies for the second and third mode are smaller than theoretical and measured. It seems that the calculated waves are not directed parallel to the harbour axis, but follow a seesawing pattern inside the

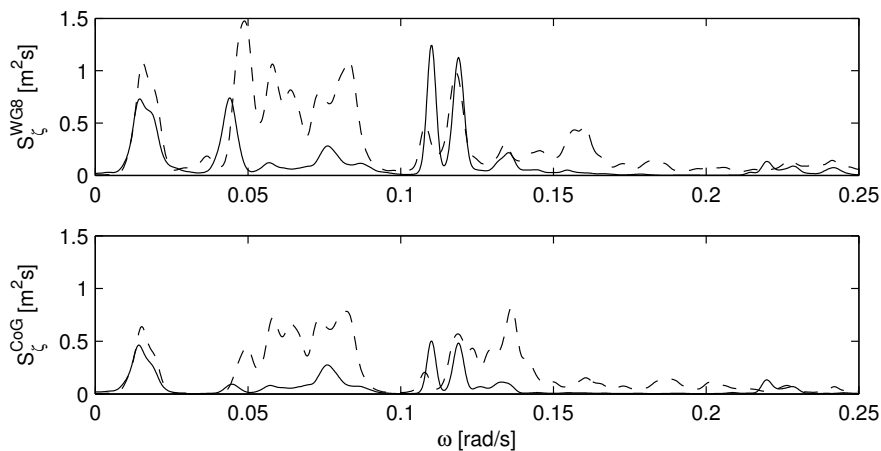


Figure 3.3: Wave spectra in the corner of the harbour (WG8, top) and at the position of the CoG of the ship (bottom); -- measurements, — SURFBEAT

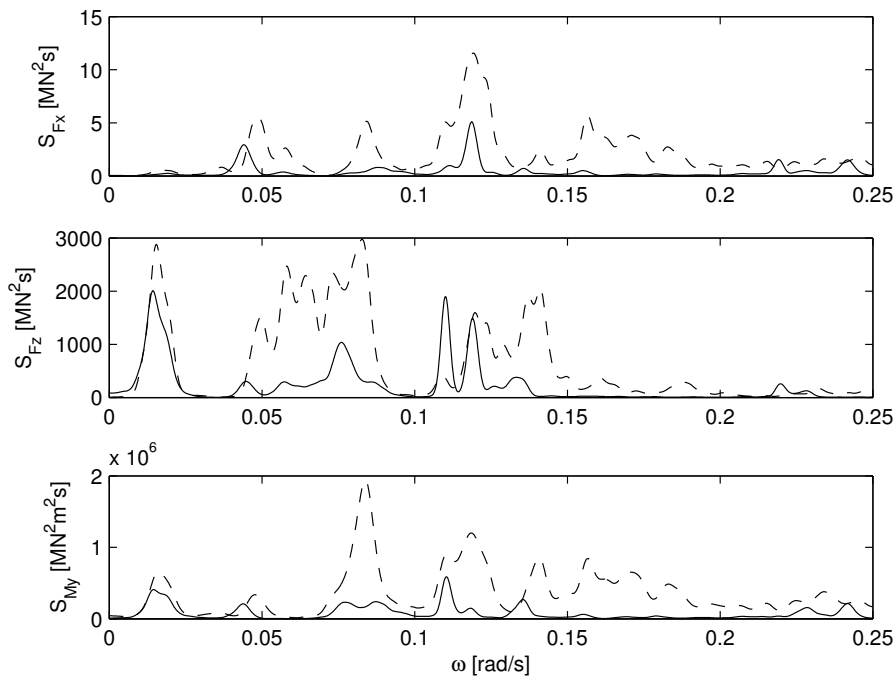


Figure 3.4: Spectra of wave forces; -- measurements, — SURFBEAT/strip theory

Table 3.1: Longitudinal resonant frequencies of the harbour basin in rad/s.

mode	theoretical ¹	measured	simulated
1	0.014	0.016	0.015
2	0.047	0.049	0.044
3	0.084	0.083	0.076

¹ after Ippen and Goda (1963)

harbour, so that the travel distance as well as the resonant period increase. In the range between 0.05 and 0.09 rad/s the measured wave energy exceeds the calculated energy. There is no direct explanation for the fact that the measurements show high energy levels also at frequencies that do not correspond with expected resonant modes of the harbour. Possibly oscillations occur in the laboratory basin which are hardly damped and amplify in the harbour. The agreement near the frequencies 0.11-0.12 rad/s seems acceptable in the corner of the harbour, but the measured peak at 0.12 rad/s is a standing wave in the direction of the harbour axis whereas the calculated waves stand in the transverse direction.

The spectra of the measured and calculated wave forces are given in Figure 3.4. The spectra are given only for the modes along the quay wall: surge, heave and pitch, because the particle motions and surface slopes in long waves perpendicular to the quay wall are very small close to the wall. Because the first mode of the harbour has a very smooth surface slope, the surge forces at this very low frequencies are almost negligible. The large peak in the measured surge spectrum at 0.12 rad/s is much smaller in the calculated spectrum, because the calculated wave energy is not directed parallel to the harbour axis. This is also shown in the comparison of current velocities in the surge direction at the location of the centre of gravity of the ship (Figure 3.5). There is a large peak in the measured current at 0.12 rad/s which also denotes large surface gradients and therefore large surge forces. The spectra for heave obviously show the same pattern as the waver levels at the CoG of the ship.

The differences between the measured and the calculated wave forces are considered to be for a major part due to the occurrence of oscillations in the model basin as mentioned above and in the difficult modelling of second order long waves in a harbour. Free long waves are generated near the harbour mouth due to pressure differences between the bound waves travelling along the harbour and the water level inside the harbour. This is also modelled, but a part of the short-wave energy diffracts into the harbour and reflects against the walls. In the model this diffraction of short waves is not treated fully correctly. The short-wave directions as calculated with

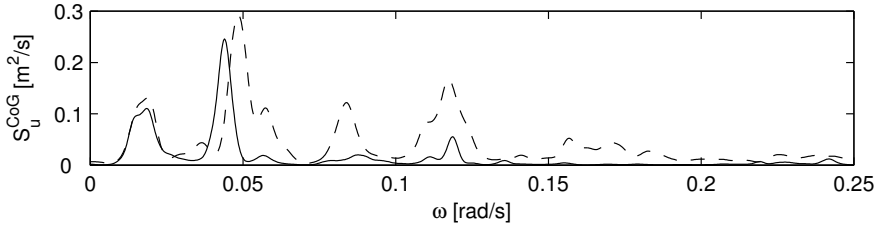


Figure 3.5: Spectra of current velocities at the location of the ship; -- measurements, — SURFBEAT

SWAN account for refraction as well as diffraction (Holthuijsen et al., 2003). However, the propagation of wave energies does not fully account for diffraction. The wave energy is only a little smoothed due to the diverging wave directions. Furthermore, all short-wave energy is assumed to be absorbed at the boundaries. These influences can be significant, but they cannot clarify the large differences between the calculated and observed long waves in the harbour at some frequencies. Obviously the modelling of these processes will improve in cases where most short-wave energy is dissipated at the boundaries due to breaking and when refraction of short waves is dominant over diffraction due to depth changes in the harbour.

3.5 Results for a coal carrier in Tomakomai Port, Japan

Further verification has been carried out for the long waves and the motions of a coal carrier in the port of Tomakomai in Japan during a typhoon passage (Hiraishi et al., 1997). This section is based on the work of Monárdez (2004). The results are also published in Van der Molen et al. (2006).

3.5.1 Prototype measurements

Port layout and wave measurements

Tomakomai Port is Japan's first large excavated port and is situated at $42^{\circ}38'$ N latitude and $141^{\circ}36'$ E longitude on the southwestern part of the Hokkaido Island, 60 km south-southeast of Sapporo. Because it is an artificial port built on a flat sandy beach facing the Pacific Ocean, it had to be protected by breakwaters from drift sand to maintain its serviceability operation, see Figure 3.6 for a layout.

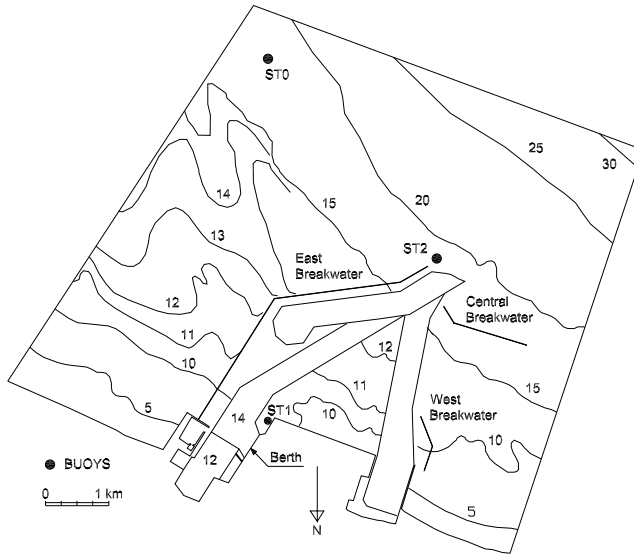


Figure 3.6: Port layout, bathymetry [m] and positions of the wave buoys.

Only sparse wave data are available, measured at three locations using pressure recorders which were able to measure high and low-frequency wave energy accurately, but were not able to record wave directions. The locations of the buoys (ST0, ST1 and ST2) are indicated in the port layout (Figure 3.6). Buoy ST0 is located offshore at a depth of about 18 m. Buoy ST1 is located near the berth inside the port area at 14 meters water depth. Buoy ST2 is placed at the entrance of the port at 18 meters water depth, just in front of the east breakwater.

Concerning wave directions in Tomakomai Port, 60% of the waves come from the south throughout the year (Hiraishi et al., 1997; Sasa, 2002, hereafter referred to as Hi97 and Sa02) followed by those from the south-southwest, south-southeast and southwest. During 80% of the year significant wave heights do not exceed 1 meter. The frequency of occurrence of waves of 1 meter or more is higher in spring and fall. Directional spreading is not known and will be assumed according to the calibration process.

The field observations were carried out on September 18 in 1994 from 00:00 until 14:00, when the cargo vessel "E.P." was berthed at the quay with a depth of 14 m, where buoy ST1 is placed. At this day, typhoon 9424 was active southeast of Japan causing the propagation of high swell waves from offshore towards Tomakomai Port (Sa02). Significant wave heights were 3 m offshore, but lower than 0.5 m inside the

port area. Despite this large reduction of the short-wave height inside the harbour, the ship was released because of large ship motions. Several lines had been broken since significant surge motions were around 4.5 m amplitude due to long-wave action (Hi97 and Sa02). After the line breaking incident, some lines were added to decrease the ship motions. In addition, initial tensions of mooring lines were lowered to prevent the breakage of ropes. Unfortunately, due to a lack of data, it is unknown when and which of the mooring lines were broken, neither the initial tensions in the mooring lines.

Table 3.2: Dimensions of the 60,000 DWT coal carrier.

Designation	Symbol	Unit	Magnitude
Length between perpendiculars	L_{PP}	m	215.00
Breadth	B	m	32.26
Depth	D	m	18.20
Actual draft	d	m	7.28
Actual displacement volume	Δ	m ³	39,685

Dimensions and mooring arrangement of the coal carrier

The dimensions of the 60,000 DWT coal carrier "E.P." are given in Table 3.2. At the moment the ship left the berth, it was loaded up to 29,446 tn, corresponding with an almost half loaded condition.

The collected data on the mooring arrangement include the coordinates of bitts, fairleads, mooring winches, number of mooring lines, force-elongation characteristics of mooring lines, coordinates, geometry and deflection-elongation characteristics of

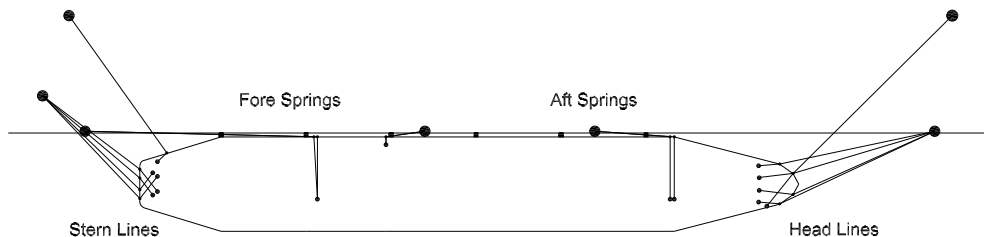


Figure 3.7: Mooring arrangement of the coal carrier.

fenders and observed ship motions for surge and heave (Shiraishi et al., 1999). The details of the mooring lines are not exactly known. Sa02 assumed synthetic fiber ropes (pylen dabbler, diameter 65 mm) with a minimum breaking strength of 657 kN at 30% elongation. Six buckling type fenders are placed against the quay wall concerned, with a height of 1.4 m and an elastic limit for the reaction force of 1153 kN at a compression of 0.19 m. The mooring arrangement consists of 4 bow lines, 4 stern lines, 4 breast lines and 4 spring lines (Figure 3.7), according to the data provided by Shiraishi et al. (1999).

Description of the measured waves and ship motions

Moored ship motions were observed on 1994 from September 17th 22:00 to September 18th 8:30 using a video observation technique to measure the ship movements in surge and heave. From the morning of September 18th, surge motions became larger as long waves became larger. The maximum amplitude of surge was nearly 4.5 m. Predominant surge period is about 150 seconds at 8:00.

The data contains several gaps in some periods. For this research, two periods of one hour of ship motions are considered. These correspond to the periods from 4:00 to 5:00 and 7:00 to 8:00 on September 18th. The energy spectra of the low-frequency waves measured inside the harbour and the surge motion of the ship are calculated for the two periods under analysis. In Figure 3.8 (left) the variance density spectra show three peaks for periods 294 s (0.0034 Hz), 142 s (0.007 Hz) and 90 s (0.011 Hz), which are values that are acceptably close to the analytical values of the natural periods of the harbour basin calculated with the methods of Merian (Raichlen, 1966) and Defant (Defant, 1961), determined at approximately 300 s, 150 s and 100 s respectively, based on the average width and length of the basin.

Figure 3.8 (right) shows that the surge motion of the ship has a different period for 4:00 to 5:00 compared with 7:00 to 8:00. The surge frequency for 4:00 to 5:00 matches with the third natural frequency of the harbour, $f = 0.011$ Hz. For 7:00 to 8:00, the peak frequency of the surge motion drops to $f = 0.007$ Hz, which matches with the second natural period of the harbour. Furthermore, the enhancement of the ship motions compared with previous periods is much larger than the enhancement of the long-wave action. The loading operation was stopped at 3:30, so the ship's mass remained constant during the periods under analysis. The only plausible explanation to the change in the response is due a drastic change in the stiffness of the mooring system possibly due to line breaking, leading to a resonant response of the moored-ship system in the period from 7:00 to 8:00 as was proposed by Hi97 and Sa02.

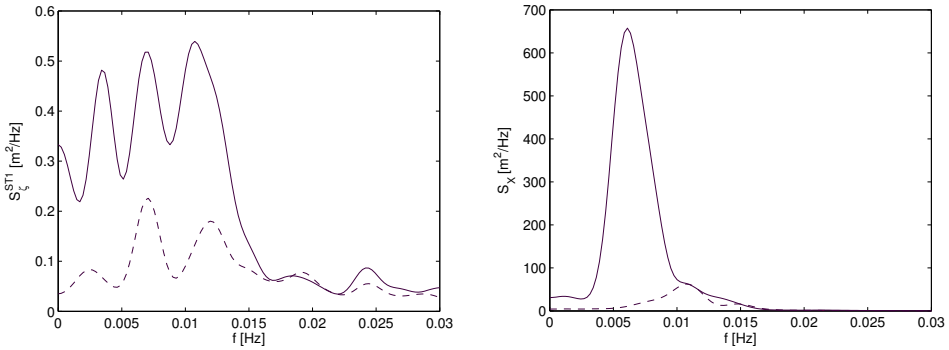


Figure 3.8: Variance density of measured long wave elevations at the harbour buoy, ST1 (left) and measured ship’s surge motion (right) on September 18th 1994 from 4:00 to 5:00 (– –) and from 7:00 to 8:00 (—).

3.5.2 Simulation of infragravity waves

Setup and calibration

The numerical model domain consists of 323×329 quadrilateral grid cells of about $25 \times 25 \text{ m}^2$ each, covering the port and a part of the ocean approximately up to the 25 m depth contour, including the location of ST0. A time step of 3.6 s was selected to fulfill the Courant number requirements for stability, calculated as 1.6. The caisson breakwaters are modelled as closed boundaries, fully absorbing the short-wave energy and fully reflecting the infragravity waves.

Input parameters of short and long waves

As explained in Section 3.2.1, the hydrodynamic model solves for the time variation of the long-wave *surface elevation* and the time variation of the short-wave *energy* at the scale of the wave groups. This distinction necessitates that a given wave spectrum (e.g. one of the measured spectra in Figure 3.9 at the offshore buoy, ST0) is separated into a short-wave part and a long-wave part at a split frequency, which is chosen at 0.03 Hz. The short-wave parameters are calibrated first for the short-wave energy model and subsequently the long-wave parameters which are the boundary conditions for the long-wave model.

Because the wave buoys provided no information about the directionality, the short-wave mean direction and directional spreading had to be chosen based on visual observations (personal communication with T. Hiraishi). The mean direction was

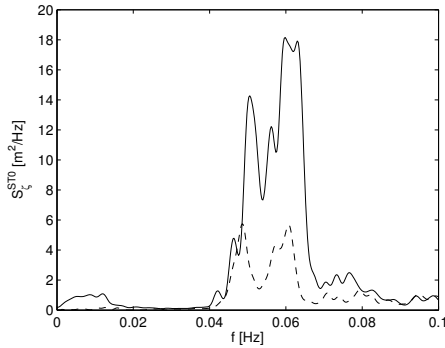


Figure 3.9: Variance density of measured wave elevations at the offshore buoy (ST0) from 4:00 to 5:00 (– –) and 7:00 to 8:00 (—).

selected as 180° (S) and a spreading angle of 17° . In this sensitivity analysis and the following calculations the parameter values of the breaking parameter γ_b and the bed roughness k_s were chosen as 0.35, which is a recommended value for small bottom slopes (Battjes & Groenendijk, 1999), and 0.2 m respectively. Variation of these parameters showed little effect on the results in these relatively deep waters, where wave breaking and bottom friction are of minor importance.

Besides the short-wave conditions, the incident long-wave conditions also need to be determined. The bound long waves are already determined by the characteristics of the short waves. The free long waves still need to be calibrated in terms of wave height, direction and directional spreading. Again, since wave directions were not measured, the mean direction and spreading of the incoming free long waves must be estimated. The free waves entering the model at the boundaries have been propagating in relatively shallow waters. Therefore, they have already been refracted according to the bathymetry and have been aligned around the mean direction. Subsequently, the mean wave direction is expected to be nearly perpendicular to the depth contours and shoreline and the directional spreading angle is expected to be much smaller than the spreading of the short waves. Therefore, the free wave mean direction are chosen as 200° (SSW), which is nearly perpendicular to the coastline (210°), with a spreading angle of 5° . The incoming free long-wave amplitude was iterated to find an optimal match between the computed and the measured low-frequency spectral shape at the offshore buoy ST0. A more detailed discussion of this iteration process and a sensitivity study on the long-wave direction and directional spreading is given in Monárdez (2004).

Results of the low-frequency wave response

Figure 3.10 shows the measured (dashed line) and computed (solid line) low-frequency wave energy for the case of 7:00-8:00 at the offshore buoy (ST0) and harbour buoy (ST1) for the parameter settings determined above. Also shown are the results of imposing only short waves with associated bound long waves (i.e. no incoming free long waves at the boundaries, dotted line).

Figure 3.10 (left) shows that the results are well-simulated at the offshore buoy (ST0), which is expected due to the correction applied to include the free wave components. The offshore buoy (ST0) recorded mainly free waves, because the energy

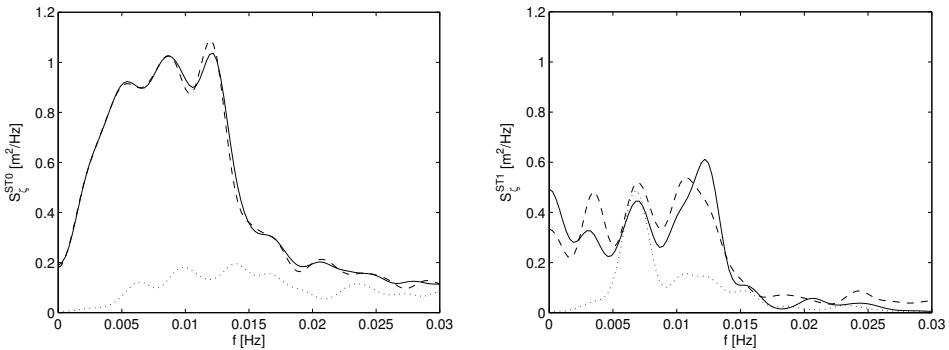


Figure 3.10: Spectral wave energy at offshore buoy ST0 (left) and harbour buoy ST1 (right) for the case from 7:00 to 8:00; measured data (---), simulation considering free and bound waves at the boundaries (—) and simulation considering only bound waves at the boundaries (···).

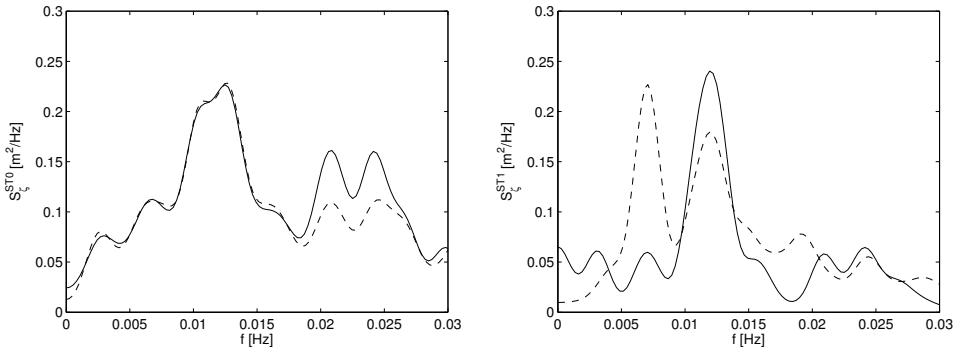


Figure 3.11: Spectral wave energy for the case from 4:00 to 5:00; legend as in Figure 3.10.

content in the case of incident short and bound long waves only (dotted line) is much lower. A possible explanation for the large amount of free wave energy is that Tomakomai is situated at the end of a very wide sound that is bound by the tip of the island Honshu in the south and the island of Hokkaido in the west and north. The typhoon waves break at the shores of this sound; the long-wave energy is released and is able to reach a different shore as a free wave.

At the harbour buoy (ST1) the calculated energy spectrum has a good agreement with the measured data (Figure 3.10 right). At the first natural frequency of the harbour ($f = 0.0034$ Hz), the simulation differs to some extent from the measurements, but the results are still acceptable. The energy peak at the second natural frequency of the harbour ($f = 0.007$ Hz) is well-predicted and appears only excited by released bound wave components (compare dotted and dashed lines).

At the third natural frequency of the harbour ($f = 0.011$ Hz), the simulations are reasonably close to the measurements. Here the resonance is caused mostly by the free wave components. From these results it is concluded that the model is capable of reproducing the wave action inside the port area with acceptable accuracy. A possible reason why the amplification of the bound wave energy occurs at the second rather than the third natural frequency is as follows. For a given frequency the bound wave number (length) is larger (smaller) than the free wave number (length) because the bound wave number is the vectorial difference between two primary wave numbers, see e.g. Sand (1982b). Conversely, for a given wave length the bound wave frequency is smaller than the free wave frequency. Since seiching is due to the resonance of a particular wave length in a basin, resonance will therefore occur for lower bound wave frequencies than free wave frequencies. However, in the basin the bound waves will be released from the wave groups in which process their wave lengths will lengthen over some propagation distance. This means that the precise bound wave amplification process is difficult to determine in a complex harbour, and is therefore not further explored here.

The results of the long waves in the harbour for the case of 4:00-5:00 (Figure 3.11 right) are less satisfactory. The first natural frequency ($f = 0.0034$ Hz) is hardly triggered in both the measurements and the simulation. The amplification at the second mode ($f = 0.007$ Hz) is underestimated while the third natural frequency ($f = 0.011$ Hz), which corresponds to the peak frequency of free waves at the ocean, is well-predicted. A possible explanation of the underestimation of the second mode is the requirement of accurate data of the short waves at the ocean. From the investigation of the case of 7:00-8:00 it was concluded that a detailed input of the short-wave spectrum at sea is important for correct modelling of the response in the mid-infragravity

frequency range. Hence, small measurement errors or incorrect input of short waves at the boundaries can lead to these significant differences. The latter explanation may play a role here, because the model parameters, such as the mean wave direction and the directional spreading, are calibrated for the case of 7:00-8:00 and were then used again for the case of 4:00-5:00. In the next section it will be shown that the third peak is the most important for ship response, so the poor modelling of the second peak will have no effect on those results.

3.5.3 Simulation of ship motions

Wave forces on the ship

The low-frequency wave forces on the coal carrier are determined using the strip theory formulations as described in Section 3.2.2. The wave forces are calculated at the positions of 25 cross-sections (Figure 3.12) and then integrated over the length of the ship. The cross-sectional added mass and damping coefficients, required for the determination of the diffraction forces, are approximated based on the values obtained with DELFRAC for the full body. For the DELFRAC computation the submerged hull is discretized with 1184 flat quadrilateral panels, the quay wall is modelled as a long array of panels and the water depth is assumed constant ($h = 14$ m), see Figure 3.12. In this fashion the influence of the quay wall on the wave pattern of the diffracted and radiated waves is taken into account. The spectra of wave forces for the two cases are plotted in Figure 3.13. The wave force spectrum for the case of 7:00 to 8:00 has four peaks. The lowest two peaks correspond to the highest two excited natural frequencies of the harbour basin ($f = 0.007$ Hz and $f = 0.011$ Hz). There are two more peaks at higher frequencies in the wave force spectrum ($f = 0.021$ Hz and $f = 0.026$ Hz), which do not have an analogous peak in the wave energy spectrum (Figure 3.8). The occurrence of these peaks in the force spectrum is related to the

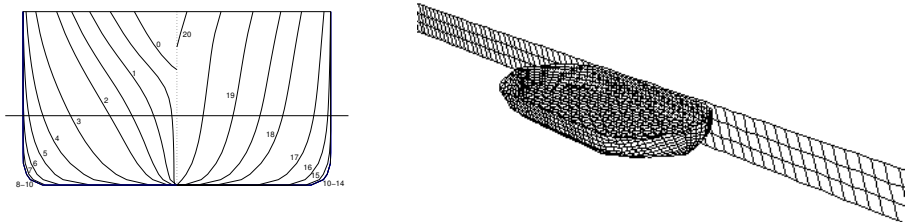


Figure 3.12: Body plan of the 60,000 DWT coal carrier (left) and panel distribution on the ship and the quay wall (right).

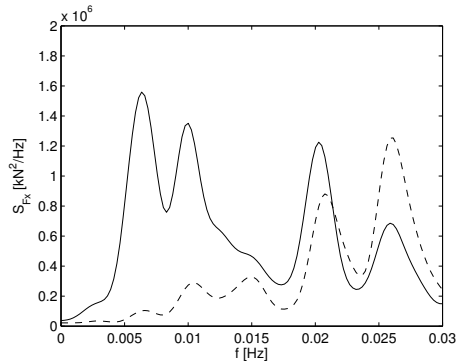


Figure 3.13: Variance density of calculated low-frequency wave forces; 4:00 to 5:00 (—) and 7:00 to 8:00 (---).

fact that the wave length of the corresponding long waves ($\lambda = 450$ to 580 m) is about twice the length of the ship. Then, the gradient of the water surface along the ship leads to considerable surge forces. The lowest energy peak of the long-wave energy spectra ($f = 0.0034$ Hz, see Figure 3.8) does not have a corresponding peak in the spectral density of the long-wave forces. Because the wave length at this frequency ($\lambda = 1000$ m) is much larger than the length of the ship, there are no considerable surge forces, but only heave forces.

Results of motions of the moored coal carrier

The only free parameters to calibrate in the ship's dynamic model are the fender friction and the initial tension in the mooring lines. The viscous damping coefficient for surge is approximated as 200 tn/m, based on experimental drag coefficients for a tanker in current (OCIMF, 1997). The fender friction coefficient is calibrated at 0.5 , although the sensitivity to fender friction appeared to be low for the low pretension in mooring lines in this case. The initial tension is calibrated considering the information from the site and previous studies. According to Sa02 some mooring lines had been broken during the loading operation, shortly before 7:00. After the line break accident, some lines were added to decrease the ship motions. In addition, initial tensions of mooring lines were lowered to prevent the breakage of ropes. Unfortunately, it is unknown when and which of the mooring lines were broken and what the pretensions in the mooring lines were. In order to overcome this lack of information, Sa02 assumed two cases: the first case with a pretension of 4 ton in each mooring line with a winch; the second case without any pretension. The calculated significant surge motions

were 5.91 m and 7.66 m and the significant surge period 95 s and 149 s for first and second case respectively. Therefore, in Sa02 the frequency of the motion was better approached for the case without pretension, while the amplitude of the surge motion was better approached for the case with pretension. Sasa's computations are based on a linear model for long-period harbour oscillations forced by free long waves, accurate calculation of the Froude-Krylov force and an approximation for the diffraction forces on the ship.

In the present study, to investigate the sensitivity of the surge motion on the pretension value, a large number of simulations for different pretensions have been carried out. A few of the results are given in Figure 3.14 for different values of the pretension in bow and stern lines. For both cases, 3 ton pretension was assumed in the spring lines. For 7:00-8:00, one spring line was assumed to be broken as was suggested by Sa02.

The peak period of the ship motions has shifted between 5:00 and 7:00. Before the line break accidents the pretension in spring lines caused a larger stiffness of the moored ship system than after the line breaking. Hence, for 4:00-5:00 the ship motions are amplified at the third natural frequency of the harbour ($f = 0.011$ Hz) and for 7:00-8:00 the amplification is at the second mode of the harbour basin ($f = 0.007$ Hz). Because the third mode of the harbour was simulated well for 4:00-5:00 and this is close to the natural surge frequency of the ship, the surge motions are simulated correctly as well.

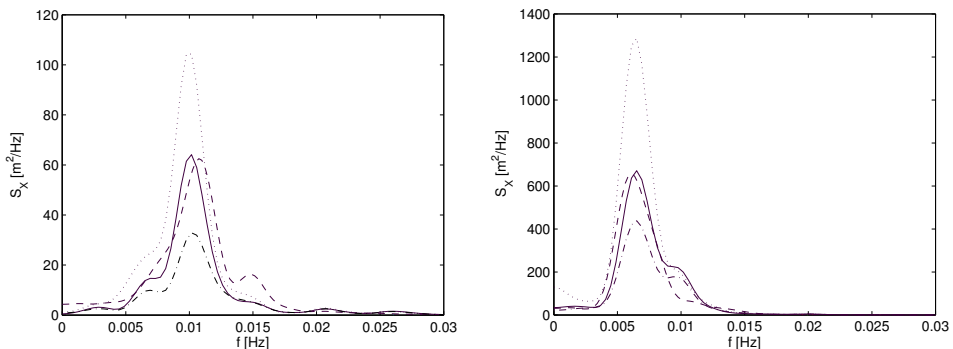


Figure 3.14: Surge motion spectra of the bulk carrier for different values of pretension in bow and stern lines. Left: case from 4:00 to 5:00; measured data (---), simulations with 2 ton (\cdots), 3 ton (—) and 4 ton ($\cdot-\cdot$) pretension. Right: case from 7:00 to 8:00; measured data (---), simulations with 2.5 ton (\cdots), 3.5 ton (—) and 4.5 ton ($\cdot-\cdot$) pretension.

Table 3.3: Significant values of low-frequency (lf) wave heights and surge motions of the ship; excursions in meters, periods in seconds.

Period	Offshore (ST0)			Harbour (ST1)				Surge motion			
	Measured			Measured		Simulated		Measured		Simulated	
	H_s	$H_{s,lf}$	$T_{s,lf}$	$H_{s,lf}$	$T_{s,lf}$	$H_{s,lf}$	$T_{s,lf}$	$X_{1,s}$	T_s	$X_{1,s}$	T_s
4-5 am	1.26	0.23	64	0.19	78	0.17	73	2.35	91	2.07	95
7-8 am	2.43	0.48	97	0.32	105	0.31	109	6.54	143	6.60	138

The results of the two cases are summarized in Table 3.3. Significant values, defined as the average of the 1/3 highest crest-trough values, are determined from the calculated wave elevations and ship motions and compared with the measurements. For 4:00-5:00 the simulation with 3 ton pretension in all lines is adopted and for 7:00-8:00 3.5 ton in head and stern lines.

The results of the simulations show that, given the information of long and short waves at the ocean, it is possible to accurately predict the wave and ship motions in the harbour, although the ship motions are very sensitive to the pretension in mooring lines.

3.6 Results for an LNG carrier on a sloping sea bed

In order to illustrate the possibilities of the method to calculate low-frequency wave forces on a ship moored in shallow water, results are presented in this Section for an LNG carrier in open water close to the shore. There are no measured data to compare with, but the focus is on investigating the important parameters related to low-frequency wave forcing in the coastal zone. Besides the influence of the bed slope on the low-frequency waves, the other components of the low-frequency drift forces and the added mass and damping are also affected (Buchner, 2006). Only low-frequency forcing due to second order waves is considered here. This is the main contribution to the total low-frequency force in shallow water.

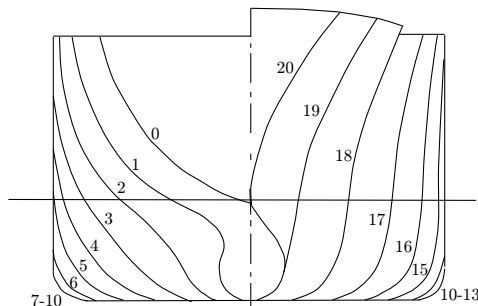
The ship is a 125,000 m³ LNG carrier. The body plan is shown in Figure 3.15 and the dimensions of the ship are given in Table 3.4. The incident wave conditions are described with a uni-directional JONSWAP spectrum with $H_s = 1.5$ m at 50 m water depth, $T_p = 15$ s, wave direction bow-on and perpendicular to the coast, $\gamma = 3.3$. The water depth at the CoG of the ship is 18.4 m ($\delta = 1.6$). The bottom slope of the coast is 1:40. With these conditions the modelling domain can be very narrow without unintended effects from the lateral boundaries. If the wave direction

Table 3.4: Dimensions of the 125,000 m³ LNG carrier.

Designation	Symbol	Unit	Magnitude
Length between perpendiculars	L_{PP}	m	273.00
Breadth	B	m	42.00
Draft	d	m	11.50
Displacement volume	Δ	m ³	98,740
Centre of buoyancy forward of station 10	LCB	m	2.16
Centre of gravity above keel	\overline{KG}	m	13.70
Transverse radius of gyration	k_{xx}	m	14.70
Longitudinal radius of gyration	k_{yy}	m	65.52

is not perpendicular to the coast or if directional spreading is considerable, long-shore currents and edge waves come into play and the modelling domain needs to be much wider. The length of the modelling domain is 2000 m for all computations with a grid size $\Delta x = 20$ m and a time step $\Delta t = 2$ s.

The results of three calculations are presented here based on three different conceptual approaches. The first calculation is based on a constant water depth of 18.4 m, with the incident wave height corrected for shoaling of the short waves. For the second calculation the actual bottom slope is considered from the wave generating boundary at 50 m water depth up to the 15 m depth contour. Reflections from the coast are not taken into account in the first two calculations. This calculation has been carried out to determine the effect of the shoaling properties of bound long waves. The third calculation includes the full effects of the bottom slope up to the shore, breaking of short waves and reflections of long waves at the coast. For this computation the grid is finer in the surf zone.

**Figure 3.15:** Body plan of the 125,000 m³ LNG carrier.

In Figure 3.16 the spectrum of wave elevations at the location of the CoG is given for the simulation with constant water depth. The results are compared with a theoretical long-wave spectrum based on the summation of the contributions of pairs of short-wave components which satisfy the second order boundary condition at the free surface (Bowers, 1976). The second theoretical result is obtained from the given short-wave energy at the same location and the formulation for the long wave based on radiation stresses in a uni-directional wave train from Longuet-Higgins and Stewart (1962):

$$\zeta^{(2)}(x, t) = -\frac{E_w(x, t)}{\rho(gh - c_g^2)} \left(\frac{2c_g}{c} - \frac{1}{2} \right) + \text{const} \quad (3.24)$$

Here the wave celerity c and the group velocity c_g are based on the peak frequency. With this assumption of a fixed celerity small errors are made, which together with the discretization of the wave energies clarify the difference between both theoretical spectra. In the simulation some energy has shifted from very low frequencies to frequencies larger than $\omega = 0.1$ rad/s along the travelling distance between the wave generating boundary and the location of the ship.

Wave spectra and surge force spectra with the results for the three calculations are given in Figures 3.16 and 3.17 respectively. The main differences between the calculations with a horizontal sea bed and the full bathymetry are at frequencies near the beat frequency, which corresponds to the period for the wave groups to travel to the shore plus the period for the long waves to return to the observation point. Concerning the results with inclusion of reflections from the coast, the peak of wave elevations is at a different position than the surge force peak due to the standing wave-like pattern in which large surge forces occur near a node. The large difference between the calculations with and without the inclusion of the bottom slope in front of the ship is striking. The long-wave height at constant water depth can be approximated with Eq. 3.24, only this equation is not based on energy conservation for waves travelling on a sloping bottom. The obtained bound wave height is proportional to $\sim h^{-5/2}$ in shallow water compared with $\sim h^{-1/4}$ when energy conservation is applied (Longuet-Higgins & Stewart, 1962). Therefore, energy has to be transferred from the short carrier wave to the long bound wave and this energy transfer costs time. For this energy transfer the bound wave tends to lag behind the wave group during the shoaling process, thus the 180° phase shift is no longer valid and consequently the celerity of the bound wave is a little smaller than the short-wave group velocity (Janssen et al., 2003). On a very gentle slope this time for energy transfer is available and the equilibrium situation is reached leading to strong enhancement of the

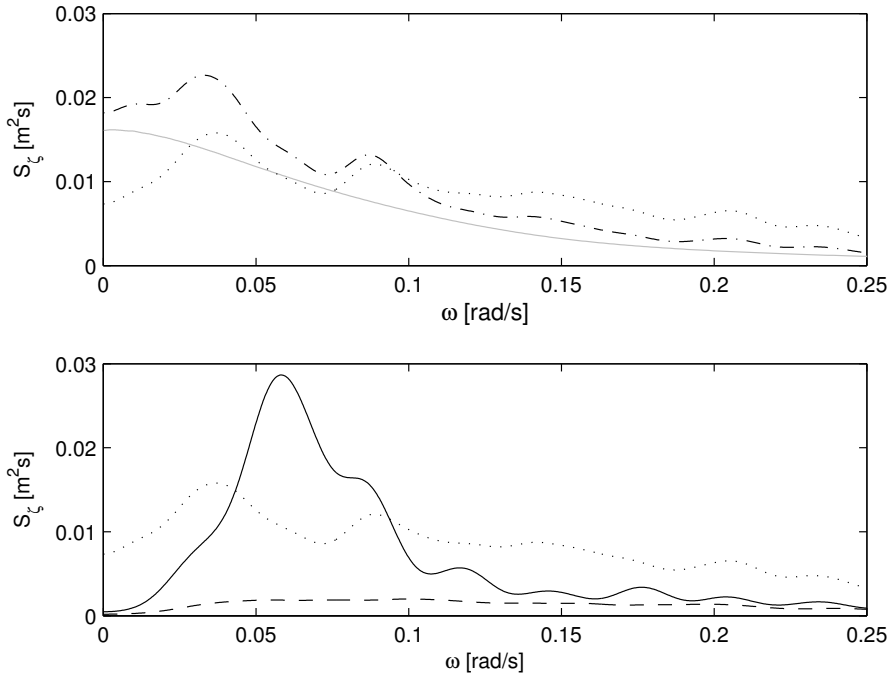


Figure 3.16: Spectra of long-wave elevations at the location of the CoG ($h = 18.4$ m). Upper plot for a horizontal sea bed: \cdots simulation, $\cdot\cdot\cdot$ from the generated wave energies, 'solid gray': theoretical after Bowers (1976); bottom plot for the dependence on the bed slope: $--$ simulation with the bed slope in front of and underneath the ship, $—$ simulation with the bed slope and reflections from the shore.

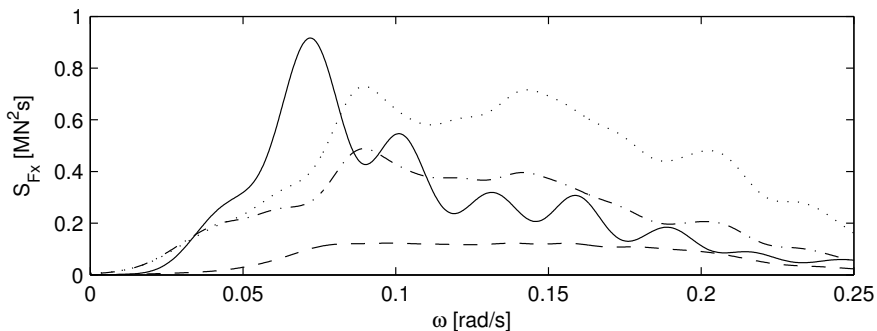


Figure 3.17: Spectra of surge forces on the ship; legend as in Figure 3.16

long waves. On a steep slope the energy transfer has only partly taken place and the growth rate of the long waves is much closer to the growth related with energy conservation comprising weak enhancement. An investigation of the shoaling properties of infragravity waves has been described by Battjes et al. (2004). They introduce a normalized bed slope parameter β which characterizes the shoaling of infragravity waves:

$$\beta \equiv \frac{h_x}{\omega} \sqrt{\frac{g}{h}} \quad (3.25)$$

with h_x the bed slope and ω the infragravity wave frequency. They find transition values for the mild-slope and steep-slope regime at $\beta \simeq 0.06$ and 0.30 . For values less than the lower limit the bottom slope is gentle enough to allow amplitude growth rates as in the equilibrium solution. For values exceeding the upper limit, the growth rate hardly deviates from the shoaling of a free wave. The study was intended to describe infragravity waves in the surf zone. Nevertheless, it can also be useful to approximate the incoming long-wave height at an open berth on a sloping sea bed. In this case using a mid-frequency value $\omega = 0.09$ rad/s and a characteristic water depth in the shoaling region $h = 30$ m, the bed slope parameter $\beta = 0.16$ yielding a transitional regime where the equilibrium situation is not fully reached.

Hence, inclusion of shoaling effects of infragravity waves can lead to a reduction of the low-frequency waves at the location of the ship. On the contrary, inclusion of reflections from the shore lead to enhancement of the long waves and a standing wave pattern is observed. In the example here a great amount of wave energy travels back out to sea as a leaky wave. There is only some dissipation due to bottom friction in the cross-shore direction, mainly in the swash zone very close to the shore with marginal water depths. If the wave direction is more oblique a large amount of wave energy can be refractively trapped as an edge wave. The influence of edge waves can reach far outside the surf zone, so that they can excite alongshore wave forcing on the ship. If the berth is far away from the coast, the generation of edge waves leads to a reduction of wave forcing due to reflections from the coast as only the leaky waves remain.

3.7 Discussion

A method has been introduced in this Chapter to calculate low-frequency response of a moored ship in a harbour due to long waves associated with wave groups at the ocean. An infragravity wave model is used based on nonlinear shallow water equations with additional forcing due to wave groups. The short-wave energies are

phase-resolved, so that it is possible to perform the calculations on a coarse grid which suits the properties of the infragravity waves. The ship is not modelled in the infragravity wave model, but the forces are calculated by postprocessing the output of the wave model. The forces are obtained using a strip-theory approach using the computed wave elevations and fluid motions at the midpoint of each cross-section of the ship. Using direct time-domain formulation for the Froude-Krylov forces and the Haskind relations for the determination of the diffraction forces with precalculated hydrodynamic coefficients for the ship, it is possible to make quick computations with fair accuracy and without information on the wave direction which is difficult to determine in the multi-directional wave field in a harbour. The motions of the ship are obtained with the third model in the chain where the low-frequency wave forces are the exciting loads on the moored ship.

Computational results have been compared with model tests for the forces on a container carrier in a rectangular harbour basin and with prototype measurements for the motions of a coal carrier moored in Tomakomai Port, Japan. The calculations of infragravity waves in the harbour agree reasonably with the measurements. The model predicts the correct natural frequencies of the harbour basin and approximates the corresponding amplification factors. The simulation results for Tomakomai Port show that both free long waves and bound waves, associated with wave groups at the ocean, can excite harbour oscillations. Both the model tests and the prototype have inherent uncertainties in the measured data: in the model tests these are related to the influence of reflections against the sidewalls of the laboratory basin and for the prototype measurements they are regarding the lack of information on the wave directions, which had to be estimated. This implies that not only wave amplitude spectra, but also accurate data on wave directions and directional spreading of long and short waves at the ocean are required for accurate modelling of wave penetration in the harbour.

The wave forces on the container ship show the same reasonable correspondence for the forces as for the wave elevations at the frequencies close to the first natural mode of the harbour basin. However, the measured surge force is dominated by a higher frequency contribution. The calculations show much less wave action along the harbour axis for these higher frequencies and therefore the calculated surge force is also less than the measured force. Wave forces were not measured during the prototype measurements.

The simulations of ship motions using the calculated infragravity waves at the location of the ship show good correspondence with the measured surge movements for the coal carrier in Tomakomai Port. Only one of the resonant peaks of the harbour

basin remains in the spectrum of the surge motions, which is closest to the natural frequency of the moored ship. The ship motions are very sensitive to the value of the pretension in the mooring lines. Due to the nonlinear properties of the synthetic mooring lines, the system becomes stiffer for increasing pretensions. Increasing the value of the pretension leads to smaller movements, but increases the line loads. Besides, the natural frequency of the moored ship is also increased. Hence, by either tensioning or slackening of mooring lines the natural frequency of the mooring system shifts away from the harbour oscillation frequency. This can be a useful and easy solution to decrease the movements of a moored ship during operation in a port subjected to low-frequency oscillations. During the model tests the ship was restrained to its position by means of a stiff frame, so that ship motions were not relevant.

Further calculations have been presented for a ship in open water on a sloping sea bed close to the coast. Results are compared between calculations with and without the bed slope and reflections from the coast taken into account. Analysis of the results has led to the conclusion that bathymetrical effects have large influences on the results. Compared with the results obtained for a horizontal sea bed without reflections, the waves and the wave forces on the ship especially increase at frequencies at little larger than the beat frequency, if the bed slope and reflections from the coast are considered.

The shoaling properties of bound waves and the process of long waves becoming free during the breaking of the wave groups are taken into account in the wave model. This makes the model very useful for the determination of low-frequency wave forces on a ship moored in the coastal zone. However, it is emphasized that the model only predicts the forces due to the incident second order wave spectrum. The wave groups are also determined and the propagation of short-wave energies is considered. However, the phase information of the individual short waves is lost and it is not possible to retrieve it unambiguously. Inside a harbour the short waves are nearly diminished, so that it is allowable to neglect them. Outside the harbour the forcing consists of first order terms and slowly varying drift forces divided by product term of first order quantities and second order waves. Only the latter contribution is predicted by the model. The other two terms need to be added. Notwithstanding for these terms it is often allowed to assume a horizontal bottom and reflection of short waves from the coast is almost negligible, so that these forces can be determined e.g. with a linear panel model. With this approach it is difficult to get the correct phase coupling between the forces due to second order waves and the other forces. Nevertheless, because the low-frequency wave forcing is dominated by the second order waves in shallow water the deviations are often acceptable.

4. A BOUSSINESQ-PANEL MODEL FOR MOORED SHIP RESPONSE IN NONLINEAR WAVES

4.1 Computational approach

For the calculation of the motions of a moored ship under the influence of waves in a harbour or in open water with considerable effects of shoaling and refraction, use is made of a combination of a wave model for wave propagation over an uneven bathymetry and a diffraction model for wave interaction with a floating object. The method described in this Chapter deals with a Boussinesq-type wave model and a linear time-domain boundary-integral diffraction model. With this approach it is possible to treat nonlinear effects which are relevant in the propagation of high waves in shallow water. Boussinesq-type wave models are capable to handle nonlinearities, such as the nonlinear wave profile (sum and double-frequency effect), the bound long wave (difference-frequency effect) and other nonlinear wave-wave interactions which are present in a non-homogeneous wave field. These nonlinear effects may be important in the area between deep water and the ship. On the other hand for a ship moored in a harbour, the wave height at the berth is much lower. Furthermore, the motions of the moored ship can often be considered small and the scattered waves, due to the scattering of the incident wave field by the ship, and the radiated waves, due to the ship movements, are much lower than the incident waves, so that a linear approach for the wave interaction with the ship is often sufficient.

The computational process is as follows. The waves in the harbour or in the coastal area are determined using a Boussinesq-type wave model. This computation takes into account the influence of the 2D variations, viz. the harbour geometry and bathymetry; the presence of the 3D shape of the ship is incorporated in the wave model. Instead, time series of pressures and flow velocities are prescribed at the hull of the ship. A reverse transformation in the Boussinesq model is used to obtain the vertical variation of the orbital velocities and the non-hydrostatic pressure from the computed depth-averaged velocities and surface elevations. The results are written

to a file which serves as input for the diffraction model.

The positions at which these quantities are prescribed are the centroids of the quadrilateral panels according to the mesh of the boundary-integral model. This model computes the scattering of the incident wave field by the presence of the ship and the subsequent wave forces. It is based on time-domain boundary-integral equations, so that direct computations can be carried out in the time-domain without transformations. Because a linear approach is adopted, the forces due to radiated waves from the moving ship are considered to be proportional to the ship movements and the calculation for the radiated waves can be carried out beforehand. Reflections of scattered waves against other structures such as nearby quay walls can be incorporated as well. For these structures it is not necessary to prescribe the incident wave conditions, because the reflection of the incident waves against fixed structures is already included in the wave model.

Calculation of ship motions can now be carried out based on the determined wave field and taking into account the nonlinear characteristics of the mooring system. The first order wave forces follow directly from the computed incident and scattered waves. Because the Boussinesq wave model is a nonlinear wave model, this force automatically includes the force due to nonlinearities in the incident wave field, otherwise referred to as the second order force due to the second order potential. The other contributions to the second order force are products of first order quantities and can be obtained based on the calculated incident, scattered and radiated waves and the ship motions.

Thus, a straightforward fully time-domain method has been defined with which it is possible to calculate the motions of a moored ship due to first and second order wave forces taking into account the multi-directional, irregular and inhomogeneous character of the wave field in a harbour.

4.2 Model formulations

4.2.1 Integral equations

Consider a body floating in a fluid that can be considered as incompressible, homogeneous and irrotational. The model domain \mathcal{D} is bounded by the body surface \mathcal{H} , the fluid surface \mathcal{F} , the sea floor \mathcal{B} and the surface of any nearby structures \mathcal{W} , see Figure 4.1. Γ is the waterline, i.e. the intersection between the body and the fluid surface. The water depth h describes the position of the sea floor below the mean fluid surface level. The coordinate system $Oxyz$ is a right-handed system with the origin

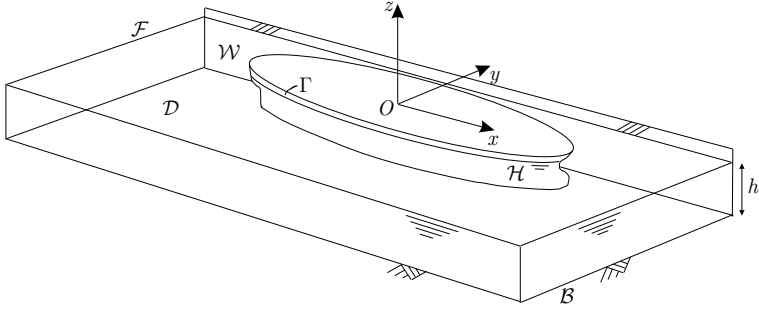


Figure 4.1: Definition sketch of the floating body in the computational domain.

at the still water level and the z -axis positive upwards. The body is able to make any arbitrary motion \vec{X} with six degrees of freedom. The motions are assumed to be small, so that linear approximations are valid. In the horizontal plane the motions are kept small by means of a mooring system connected to the body.

The fluid flow around the floating body is described by means of a velocity potential Φ , which is defined such that the gradient of Φ is equal to the flow velocity. The velocity potential is decomposed into

$$\Phi = \phi^I + \phi^S + \sum_{j=1}^6 \phi^j \quad (4.1)$$

the scattered wave potential ϕ^S , describing the scattering of the incident wave potential ϕ^I around the floating body and the radiation potentials ϕ^j due to the moving body in the j -mode. The sea floor \mathcal{B} is assumed horizontal in the area surrounding the floating body, so that a constant water depth assumption can be applied for the calculation of the radiated and scattered waves. Large-scale bottom variations though can be included in the computation of the incident wave propagation, which is necessary because the total area of interest (e.g. a complete harbour) is much larger than the fluid domain considered in the diffraction model (the area surrounding the moored ship).

To solve the velocity potentials ϕ in time Green's theorem is applied:

$$\int_0^\infty d\tau \iint_{\mathcal{H}_0 + \mathcal{W}_0} (\phi G_{n_\xi} - \phi_{n_\xi} G) dS_\xi = \begin{cases} -4\pi\phi, & \vec{x} \in \mathcal{D} \\ -2\pi\phi, & \vec{x} \in \mathcal{H}_0 \cup \mathcal{W}_0 \\ 0, & \vec{x} \in \mathcal{D}_i \end{cases} \quad (4.2)$$

where \mathcal{H}_0 and \mathcal{W}_0 denote the mean wetted surface of the bodies and \mathcal{D}_i refers to the domain interior to the bodies. $G(\vec{x}, \vec{\xi}, \tau)$ is the Green function which satisfies the boundary conditions at the free surface and at the bottom. The time-domain Green function is the solution of the potential due to an impulsive source below a free surface. The formulation and a description of the numerical algorithm to calculate the Green function are given in Appendix B. The subscript n_ξ denotes the normal derivative with respect to the source point $\vec{\xi}$.

4.2.2 Equation of motion

The motions of the ship in the six degrees of freedom are obtained by integrating the equation of motion in time in the form as proposed by Cummins (1962):

$$(\mathbf{M} + \mathbf{A})\ddot{\vec{X}}(t) + \mathbf{B}\dot{\vec{X}}(t) + \mathbf{C}\vec{X}(t) + \int_0^\infty \mathbf{K}(\tau)\vec{X}(t - \tau)d\tau = \vec{F}(t) \quad (4.3)$$

where \mathbf{M} is the inertia matrix. \mathbf{A} , \mathbf{B} and \mathbf{C} are the matrices for the added mass, linearized viscous damping and hydrostatic restoring respectively. \mathbf{K} contains the impulse response functions. The external force \vec{F} may consist of several contributions, both linear and nonlinear, also considering the characteristics of the mooring system. The linear contributions of the hydrodynamic forces due to the moving body are collected in the left-hand side and the wave forces on the restrained body are in the right-hand side together with all nonlinear contributions.

4.2.3 Hydrodynamic forces

The hydrodynamic coefficients in the equation of motion (Eq. 4.3) can be obtained by solving the radiation problem, which is described here following the derivations made by Cummins (1962), Wehausen (1967) and Beck and Liapis (1987). The radiation problem is treated for the body making an impulsive movement at time $t = 0$ in the j -mode in initially still water

$$\dot{X}_j(t) = \delta(t), \quad j = 1, 2, \dots, 6 \quad (4.4)$$

where δ is the Dirac delta function. After $t = 0$ the body is again fixed to its position, only the fluid surface has been disturbed. The fluid flow is described by means of a velocity potential ϕ , which is decomposed into an impulsive and a time-varying part

$$\phi^j(\vec{x}, t) = \psi^j(\vec{x})\delta(t) + \chi^j(\vec{x}, t) \quad (4.5)$$

The potentials have to meet the Laplace condition in the fluid domain, the linearized dynamic and kinematic conditions at the free surface, the Neumann condition at the closed boundaries and the sea floor which is assumed horizontal and the Dirichlet condition at infinite distance from the floating body and for ψ at the free surface:

$$\nabla^2 \chi^j = 0 \quad \text{in } \mathcal{D} \quad (4.6)$$

$$\psi^j = 0 \quad \text{on } z = 0 \quad (4.7)$$

$$\chi_{tt}^j + g\chi_z^j = 0 \quad \text{on } z = 0 \quad (4.8)$$

$$\psi_n^j = \begin{cases} n^j & \text{on } \mathcal{H} \\ 0 & \text{on } \mathcal{W} \text{ and } z = -h \end{cases} \quad (4.9)$$

$$\chi_n^j = 0 \quad \text{on } \mathcal{H}, \mathcal{W} \text{ and } z = -h \quad (4.10)$$

$$\psi^j = 0, \quad \chi^j = 0 \quad \text{for } R \rightarrow \infty \quad (4.11)$$

where R is a horizontal distance and \vec{n} is the unit normal vector directed out of the fluid domain; $n_{4...6} = (\vec{x} - \vec{x}_G) \times \vec{n}$. For the determination of the potentials ψ and χ either a direct or an indirect method can be used. Computation using the indirect source potential formulation is less efficient, only with the advantage that it is easier to compute velocities in the fluid. The direct formulation is provided here. The indirect formulation is analogous to the indirect formulation to determine the scattered waves as given in Section 4.2.5.

Substitution of the potential and the boundary condition in Green's theorem leads to integral equations for ψ and χ :

$$\begin{aligned} 2\pi\psi^j(\vec{x}) + \iint_{\mathcal{H}_0 + \mathcal{W}_0} \psi^j(\vec{\xi}) G_{n_\xi}^{(0)}(\vec{x}, \vec{\xi}) dS \\ - \iint_{\mathcal{H}_0} n_\xi^j(\vec{\xi}) G^{(0)}(\vec{x}, \vec{\xi}) dS_\xi = 0 \end{aligned} \quad (4.12)$$

$$\begin{aligned} 2\pi\chi^j(\vec{x}, t) + \iint_{\mathcal{H}_0 + \mathcal{W}_0} \left[\chi^j(\vec{\xi}, t) G_{n_\xi}^{(0)}(\vec{x}, \vec{\xi}) + \psi^j(\vec{\xi}) G_{n_\xi}^w(\vec{x}, \vec{\xi}, t) \right] dS_\xi \\ + \int_0^t d\tau \iint_{\mathcal{H}_0 + \mathcal{W}_0} \chi(\vec{\xi}, t - \tau) G_{n_\xi}^w(\vec{x}, \vec{\xi}, \tau) dS_\xi \\ - \iint_{\mathcal{H}_0} n_\xi^j G^w(\vec{x}, \vec{\xi}, t) dS_\xi = 0 \end{aligned} \quad (4.13)$$

$G^{(0)}$ and G^w are the impulsive and the wave part of the Green function respectively.

The hydrodynamic forces can be obtained from pressure integration over the wetted hull \mathcal{H} . Integration of ψ leaves the added mass coefficients A_{kj} and integration of χ_t leads to the impulse response functions K_{kj} :

$$A_{kj} = \rho \iint_{\mathcal{H}_0} \psi^j n^k dS_\xi, \quad k = 1, 2, \dots, 6 \quad (4.14)$$

$$K_{kj}(t) = \rho \iint_{\mathcal{H}_0} \frac{\partial \chi^j}{\partial t} n^k dS_\xi, \quad k = 1, 2, \dots, 6 \quad (4.15)$$

4.2.4 Incident waves

For the determination of the incident wave, thus without the disturbance due to the presence of the ship, the Boussinesq-type wave model TRITON (Borsboom et al., 2000), developed at WL|Delft Hydraulics, is used. The starting point of Boussinesq wave modelling is that the 3D wave flow is written in 2D equations. The variation of the flow over the water depth is accounted for using a truncated polynomial expansion of the horizontal particle velocity over depth in terms of a dispersion parameter μ and a nonlinearity parameter ε . After expanding the continuity and the momentum equations, all terms up a certain order of μ and ε are gathered to provide the model equations. Still, there is quite some freedom in deriving Boussinesq equations leading to improvements in dispersion, shoaling and nonlinearity characteristics. The model equations in TRITON are modified in such a way that low-order Boussinesq equations conserve both mass and depth-integrated momentum. These are given here in generalized form. For a more detailed derivation of the model equations is referred to Borsboom et al. (2000). The continuity equation reads

$$\frac{\partial D}{\partial t} + \nabla \cdot (D\vec{u}) = 0 \quad (4.16)$$

and the momentum equation:

$$\rho \frac{\partial D\vec{u}}{\partial t} + \frac{1}{2} \rho \nabla (D\vec{u} \cdot \vec{u}) + \nabla P - p_b \nabla h = 0 \quad (4.17)$$

where $D = h + \zeta$ the total water depth and \vec{u} is the depth-averaged horizontal flow velocity. In these 2D Boussinesq equations the linear operator ∇ denotes the horizontal gradient. P is the depth-integrated pressure force, p_b is the pressure at the bottom and ∇h the bottom slope. To improve the dispersion and shoaling characteristics, the model is extended with a [2/2] Padé approximation, which is incorporated in the formulations of P and p_b . The model gives accurate results up to $kh \approx 3$.

Various types of boundary conditions can be modelled. At seaward boundaries incident waves in the form of time series or spectra can be prescribed, while at the same time waves can leave the domain without spurious reflections (Borsboom et al., 2001). Full and partial reflection at arbitrarily shaped inner domain structures (e.g. quay walls) can be modelled as well (Wenneker & Borsboom, 2005). This implies that the model is capable of accurately treating complex harbour geometries.

For a correct link between the 2D Boussinesq model and the 3D boundary-integral model, the pressures and particle velocities need to be prescribed at the hull of the floating body \mathcal{H} . Hence, back-transformation of the depth-averaged velocity and pressure is required to find the distributions over the water depth. Transformation of the variables from the original model equations lead to formulations for the velocities and the pressure p in the fluid. The formulations are given here as the following power series:

$$\vec{u}(x, y, z, t) = \vec{u}^{(0)} + (z + h)\vec{u}^{(1)} + (z + h)^2\vec{u}^{(2)} \quad (4.18)$$

$$w(x, y, z, t) = w^{(0)} + (z + h)w^{(1)} + (z + h)^2w^{(2)} + (z + h)^3w^{(3)} \quad (4.19)$$

$$p(x, y, z, t) = p^{(0)} + (z + h)p^{(1)} + (z + h)^2p^{(2)} \quad (4.20)$$

The horizontal velocities are expanded up to the same order (2) as in the model equations. The vertical velocity w is expanded to the third order, so that the divergence-free constraint

$$\nabla \cdot \vec{u} + \frac{\partial w}{\partial z} = 0 \quad (4.21)$$

is satisfied. Expressions for the terms $\vec{u}^{(n)}$, $w^{(n)}$ and $p^{(n)}$ contain quantities that are directly available from the numerical model equations (or easily computed from them), such as ∇h , D , ∇D , $\nabla \cdot (D\vec{u})$, and so on.

4.2.5 Wave forces

The diffraction problem is solved for the scattering of waves around the floating body \mathcal{H} . The scattered potential ϕ^S describes the scattering of the incident wave ϕ^I . The scattering of the incident waves around the other structures \mathcal{W} is assumed to be included in the incident wave potential ϕ^I , so that ϕ^I only needs to be prescribed on \mathcal{H} . This also implies that ϕ^S decays for large distances from the floating body, so that no difficulties arise at the edges of the computational domain, e.g. if long quay walls are cut off in the computational domain at large distances from the ship. The

scattered potential has to meet the following conditions:

$$\nabla^2 \phi^S = 0 \quad \text{in } \mathcal{D} \quad (4.22)$$

$$\phi_{tt}^S + g\phi_z^S = 0 \quad \text{on } z = 0 \quad (4.23)$$

$$\phi_n^S = \begin{cases} -\phi_n^I & \text{on } \mathcal{H} \\ 0 & \text{on } \mathcal{W} \text{ and } z = -h \end{cases} \quad (4.24)$$

$$\phi^S = 0 \quad \text{for } R \rightarrow \infty \quad (4.25)$$

Analogous to the solution for the radiation problem and derivations described by Kormsmeier and Bingham (1998), the direct formulation can be applied:

$$\begin{aligned} 2\pi\phi^S(\vec{x}, t) + \iint_{\mathcal{H}_0 + \mathcal{W}_0} \phi^S(\vec{\xi}) G_{n_\xi}^{(0)}(\vec{x}, \vec{\xi}) dS_\xi + \iint_{\mathcal{H}_0} \phi_{n_\xi}^I(\vec{\xi}) G^{(0)}(\vec{x}, \vec{\xi}) dS_\xi \\ + \int_{-\infty}^t d\tau \iint_{\mathcal{H}_0 + \mathcal{W}_0} \phi^S(\vec{\xi}, t - \tau) G_{n_\xi}^w(\vec{x}, \vec{\xi}, \tau) dS_\xi \\ + \int_{-\infty}^t d\tau \iint_{\mathcal{H}_0} \phi_{n_\xi}^I(\vec{\xi}, t - \tau) G^w(\vec{x}, \vec{\xi}, \tau) dS_\xi = 0 \end{aligned} \quad (4.26)$$

Alternatively, the indirect source potential formulation can be used. This is a common technique in potential theory with the advantage that the velocities in the fluid are easily obtained. The indirect formulation is reached after introducing a scalar potential ϕ' which describes the flow interior to the body. The source strength σ is defined as the remaining difference between the normal velocities at the body surface

$$\sigma = \frac{1}{4\pi} (\phi_n^S - \phi_n') \quad (4.27)$$

The source strength is further defined such that $\phi' = \phi^j$ at the body surface. Substituting the formulations for σ in Green's theorem leads to an expression for ϕ^S

$$\begin{aligned} \phi^S(\vec{x}, t) = \iint_{\mathcal{H}_0 + \mathcal{W}_0} \sigma(\vec{\xi}, t) G^{(0)}(\vec{x}, \vec{\xi}) dS_\xi \\ + \int_0^t d\tau \iint_{\mathcal{H}_0 + \mathcal{W}_0} \sigma(\vec{\xi}, t - \tau) G^w(\vec{x}, \vec{\xi}, \tau) dS_\xi \end{aligned} \quad (4.28)$$

which is without terms proportional to derivatives of the Green function. Consequently, determination of velocities only requires first order derivatives of the Green function. The unknown source strengths are determined from the following integral equation

$$\begin{aligned}
2\pi\sigma(\vec{x}, t) + \int_0^t d\tau \iint_{\mathcal{H}_0 + \mathcal{W}_0} \sigma(\vec{\xi}, t - \tau) G_{n_x}^w(\vec{x}, \vec{\xi}, \tau) dS_{\xi} \\
+ \iint_{\mathcal{H}_0 + \mathcal{W}_0} \sigma(\vec{\xi}, t) G_{n_x}^{(0)}(\vec{x}, \vec{\xi}) dS_{\xi} = \begin{cases} -\phi_{n_x}^I(\vec{x}, t), & \vec{x} \in \mathcal{H} \\ 0 & , \vec{x} \in \mathcal{W} \end{cases} \quad (4.29)
\end{aligned}$$

Using either the direct or the indirect formulation, the incident wave can be given as arbitrary time series of normal velocities provided on the hull of the floating body. Treatment of nonlinear multi-directional waves is well-possible, only the scattered waves are treated as linear waves.

The first order wave forces due to the incident and scattered wave are found by integration of first order pressures over the mean submerged hull, where the pressure p can be obtained using Bernoulli's equation

$$-\frac{p - p_0}{\rho} = gz + \frac{\partial\Phi}{\partial t} + \frac{1}{2}\nabla\Phi \cdot \nabla\Phi + \text{const} \quad (4.30)$$

with p_0 the atmospheric pressure. The first term in the right-hand side contributes to the restoring forces. The second term is the linear component of the dynamic pressure and the third term is the quadratic pressure related to the second order forces. The first order wave force is the sum of the Froude-Krylov force, given by the integration of pressures in the undisturbed wave, p^I , over the mean submerged hull, and the diffraction force, which is found by integration of first order pressures in the scattered wave:

$$\vec{F}^{(1)} = \iint_{\mathcal{H}_0} \left(p^I - \rho \frac{\partial\phi^S}{\partial t} \right) \vec{n} dS \quad (4.31)$$

$$\vec{M}^{(1)} = \iint_{\mathcal{H}_0} \left(p^I - \rho \frac{\partial\phi^S}{\partial t} \right) (\vec{x} - \vec{x}_G) \times \vec{n} dS \quad (4.32)$$

The second order wave effects are already included in these forces, because a non-linear wave model is used for the incident waves. However, the other contributions to the second order forces are not taken into account. The second order wave forces are obtained using the direct pressure integration technique (Pinkster, 1980). The remaining four terms in the formulation for the second order force and moment include the products of first order quantities, i.e. (1) the relative wave height, (2) the second order pressure, (3) the product of first order pressures and first order body motions and (4) the contribution of the product of first order rotations and first order inertia forces:

$$\begin{aligned} \vec{F}^{(2)} &= \frac{1}{2}\rho g \int_{\Gamma} (\zeta - \alpha_3)^2 \vec{n} dl \\ &\quad - \rho \iint_{\mathcal{H}_0} \left(\frac{1}{2} \nabla \Phi \cdot \nabla \Phi + \vec{\alpha}^{(1)} \cdot \nabla \frac{\partial \Phi}{\partial t} \right) \vec{n} dS + \vec{\Omega}^{(1)} \times \mathbf{M} \vec{X}^{(1)} \end{aligned} \quad (4.33)$$

$$\begin{aligned} \vec{M}^{(2)} &= \frac{1}{2}\rho g \int_{\Gamma} (\zeta - \alpha_3)^2 (\vec{x} - \vec{x}_G) \times \vec{n} dl + \vec{\Omega}^{(1)} \times \mathbf{M} \vec{\Omega}^{(1)} \\ &\quad - \rho \iint_{\mathcal{H}_0} \left(\frac{1}{2} \nabla \Phi \cdot \nabla \Phi + \vec{\alpha}^{(1)} \cdot \nabla \frac{\partial \Phi}{\partial t} \right) (\vec{x} - \vec{x}_G) \times \vec{n} dS \end{aligned} \quad (4.34)$$

where $\vec{\alpha} = \vec{X} + \vec{\Omega}(\vec{x} - \vec{x}_G) \times \vec{n}$ is the local displacement vector with $\vec{\Omega}$ the rotation about the centre of gravity. The wave elevation ζ and the velocity potential Φ include the contributions of the incident, the scattered and the radiated wave. Contrary to frequency-domain calculations the second order force is not calculated based on the freely floating body, but on the moving body influenced by the mooring system. Therefore, the quantities are not necessarily of first order, but these are quantities based on the actual fluid and body motions. To reduce the effect of unrealistic second order forces due to large horizontal body motions, the near-resonance low-frequency horizontal motions are removed in the calculation of the second order force, leaving the wave-frequency movements denoted by the superscript (1) in Eqs. 4.33 and 4.34.

4.3 Numerical considerations

4.3.1 Numerical implementation

Boussinesq model computations (without the floating body) are carried out on an orthogonal rectilinear grid. Inclusion of more complicated basin shapes is possible using a cut-cell technique (Wenneker & Borsboom, 2005). To acquire accurate results of the nonlinear wave form, a grid size of at least 20 grid points per wave length is necessary. The discretization in space is carried out using a central finite volume scheme. An explicit fourth-order Runge-Kutta method is used for the integration in time.

The integration of the integral equations for the radiation and the diffraction problem is carried using a linear panel method. The mean wetted surfaces of the floating body \mathcal{H} and the other structures \mathcal{W} are discretized by in total N flat quadrilateral (or triangular) elements at which the velocity potential is assumed constant. The collocation points for the unknown potentials are placed in the element centroids, thus leaving a system of N linear equations with N unknowns. The integration of

the impulsive part of the Green function $G^{(0)}$ and its normal derivative are performed using the algorithms in Newman (1986), which is an exact analytical integration of the $1/r$ terms. The evaluation of the time-dependent Green function G^w is taken at the element centroids or a four-point Gauss quadrature formula is used for the integration over the element. This only gives unacceptable errors if both the element and the field point are close to the free surface. In that case a horizontal array of 3 or 5 points is used for the integration over the element, so that panels close to the free surface with a large aspect ratio can be treated.

Time-domain boundary-integral methods require the evaluation of lengthy convolution integrals involving the Green function. This matrix of Green functions easily becomes very large. E.g. considering a domain with $N = 1000$ panels (if other structures play a role, symmetry relations cannot be applied), time step $\Delta t = 0.5$ s, the period of the convolution integral $T = 2$ minutes and using single precision, the storage space for the matrix is $N^2 \times T/\Delta t \times 4$ bytes = 916 Mb. In order to speed up the computation, the whole matrix should be stored in RAM memory. For the calculations carried out in this thesis the storage space was limited to 2 Gb. If the direct formulation is used to determine the scattered potentials, the integral equation (Eq. 4.26) is solved in the following form:

$$\mathbf{D}\vec{\phi}^S = \vec{\varphi}^I(t) + \vec{\varphi}^S(t) \quad (4.35)$$

in which the vectors contain the values at each collocation point. $\vec{\varphi}^I$ and $\vec{\varphi}^S$ comprise the products $G\phi_n^I$ and $G_n\phi^S$ respectively. $\vec{\varphi}^I$ is computed first for all time steps, after which $\vec{\varphi}^S$ is evaluated and ϕ^S can be obtained. In this way either the large array G or G_n fills up the memory, while the other is stored to disc. If the source potential formulation is used, this procedure is more straightforward, because the arrays G and G_n are already in separate equations. The integration in time of the convolution integrals is carried out using Simpson's rule with a fixed time step Δt . The convolution integrals can be cut off to reduce the number of Green function values to be stored and to reduce the calculation time. The cut-off period must at least be chosen such that the information of waves that are generated at a wave making source is preserved at all boundaries. E.g. if the incident waves are prescribed at the ship alone, the integration length of the convolution integral must at least be the time for the shortest waves of interest to travel to a different structure, so that the waves reflected from this structure are preserved. The convolution integrals also involve a term proportional to the potential at time t . However, the Green function G^w and its spatial derivatives are equal to zero at $\tau = 0$, so there is no contribution of the wave

part of the Green function to the matrix \mathbf{D} at the left-hand side of Eq. 4.35. The matrix \mathbf{D} therefore only contains the values of $G_n^{(0)}$ and it is independent of time, so that it only needs to be filled and inverted once.

The input of the integral equation for the scattered waves, Eq. 4.29, are the particle velocities in the undisturbed wave. These are prescribed at the collocation points together with the incident wave pressures for the determination of the wave forces. Incident wave elevations are prescribed at the midpoints of the waterline segments, which are required for the computation of the second order forces.

The normal velocity on the hull in the incident wave serves as boundary condition for the boundary-integral model. The velocities along the hull are required for the determination of the second order forces. These lateral velocities in the incident wave are easily obtained from the TRITON output. The velocities in the scattered and radiated waves are defined as the gradients of the scattered and radiated potentials. To avoid lengthy computations to provide the velocities of the scattered and radiated waves along the hull (e.g. using the gradient of Eq. 4.28), the velocities are obtained by numerically determining the gradients of the velocity potential along the hull (the normal gradient of the total potential is known and equal to the local normal body velocity). To determine the lateral gradients the potential is first provided at the nodes of the element by linear interpolation between the neighbouring collocation points. With the known potentials at the nodes of the element, it is straightforward to determine the gradient over the quadrilateral. A different process is carried out to obtain the potentials at nodes that are at the free surface and to obtain wave elevations at the waterline segments. The free surface condition (Eq. 4.23) is used to calculate the potential here from the given potential at the closest collocation point(s).

The integration of the equation of motion for the moored ship is carried out by means of a Runge-Kutta scheme taking into account the nonlinear characteristics of fenders and mooring lines. Low-frequency viscous damping is included in the calculation of the current and wind forces. The current and wind velocities are taken relative to the moving body. Other sources of viscous damping, such as damping in mooring lines and fender hysteresis can be incorporated in experimental coefficients. The second order wave forces, which consist of both high and low-frequency contributions, are obtained simultaneously with the determination of the ship motions.

4.3.2 Irregular frequencies

So-called irregular frequencies are known to have detrimental effects on computations with boundary-integral methods. An irregular frequency corresponds to one of the

eigenfrequencies of the fictitious flow problem interior to the body with Dirichlet conditions at the body boundary. Irregular frequencies come into play, because of the fact that the analytical integral equation is numerically discretized and described at the body surface alone by introducing a Green function that fulfills the boundary condition at the free surface. Hence, they are not present in Rankine panel models. The irregular frequency problem has been studied extensively, mainly in the frequency-domain, beginning with the theoretical work of John (1950). There are a few options to remove their effect in the frequency-domain. The most widely used and most robust solution is to apply a lid at the free surface inside the body as proposed by Ohmatsu (1975). A mesh is provided at the free surface at which the boundary condition relates the velocity potential and its vertical derivative according to the free surface condition and the flow problem interior to the body is solved simultaneously with the exterior problem, see e.g. Huijsmans (1996) for the mathematical formulations and numerical results obtained with this technique.

In time-domain computations the irregular frequencies are also present, but their removal is more awkward. A mesh at the free surface is not possible because of the singularity of the Green function here and because the velocity potential and its vertical derivative are not unambiguously related in irregular waves. Korsmeyer and Sclavounos (1989) propose a large-time asymptotic matching technique for the removal of irregular frequencies from the impulse response functions. However, such an approach is not accurate if the waves are influenced by other nearby structures. Therefore, this technique is not used in this thesis, but it is assumed that the effect is effectively reduced when the number of panels is sufficiently large and the time step sufficiently small (Korsmeyer & Bingham, 1998). Further consideration why the effects of irregular frequencies are not removed is the fact that for normal hull shapes and without forward speed the irregular frequencies are well outside the range of frequencies of interest.

The irregular frequency problem can also come into play when dealing with long time series so that the convolution integrals in Eqs. 4.26 or 4.29 have to be cut off in order to obtain a workable computation. If the Green function is cut off at a position at which it has not yet sufficiently decayed, this is felt as an instability and the system reacts to this instability by introducing an oscillation at the frequency of mainly the first irregular frequency. If the convolution integral is cut off in the radiation problem, this phenomenon is immediately observed in the impulse response functions. In the diffraction problem this is not immediately observed, because there is no impulsive instability at $t = 0$. Nevertheless, instabilities can grow gradually and lead to problems at a much later stage. Hence, the length of the kernel in the

convolution integrals must be chosen at a level at which the Green functions have sufficiently decayed. The required kernel length is generally longer for shallow water than for deep water. This effect occurs for systems which are vulnerable to irregular frequencies, e.g. for a ship in open water. If the waves are highly influenced by the presence of other structures, this is a much smaller problem.

Another phenomenon related to the discretization of the hull is the occurrence of high-frequency instabilities, if the panels that intersect with the free surface are not wall-sided. Theoretically, these panels should be exactly orthogonal to the free surface. Practically, small deviations of the angle are acceptable and the results are not significantly affected if $|n_z| \leq 0.6$, where n_z is the vertical component of the normal vector.

5. RESULTS OF THE TIME-DOMAIN PANEL MODEL FOR LINEAR WAVES

As a verification of the time-domain boundary-integral model, computations have been performed for a 200 kDWT tanker in open water and for a Panamax container ship in a harbour. The incident waves are assumed as linear waves, so that simple linear wave theory can be applied to obtain the wave propagation in constant water depth. Concerning the calculations for the tanker regular incident waves are treated and for the container ship irregular waves. The focus is on the first order wave forces on the ship, but also mean drift forces are calculated for the tanker.

5.1 200 kDWT tanker in open water

Computational results are compared with model test measurements and other numerical calculations for a 200 kDWT tanker. This ship is chosen, because computational results as well as model test data are readily available from literature to compare with. The model test experiments have been carried out by Van Oortmerssen (1976) on the tanker in 100% loading condition and with a water depth of 22.68 ($\delta = 1.2$;

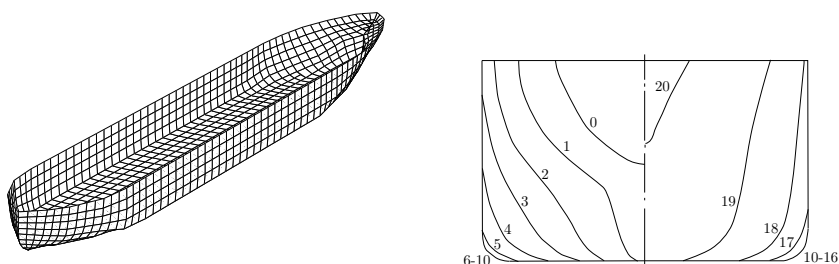


Figure 5.1: Hull mesh (1042 panels) and body plan of the 200 kDWT tanker;

Table 5.1: Dimensions of the 200 kDWT tanker

Designation	Symbol	Unit	Magnitude
Length between perpendiculars	L_{PP}	m	310.00
Breadth	B	m	47.17
Draft	d	m	18.90
Displacement volume	Δ	m ³	234,826
Centre of buoyancy forward of station 10	LCB	m	6.60
Centre of gravity above keel	\overline{KG}	m	13.32
Transverse radius of gyration	k_{xx}	m	14.77
Longitudinal radius of gyration	k_{yy}	m	77.47
Longitudinal radius of gyration	k_{zz}	m	79.30

the water depth relative to the draft of the ship), so that the influence of finite water depth is significant. The dimensions of the ship are given in Table 5.1.

The experiments consisted of oscillation tests in which the ship was given a forced harmonic motion with a constant period and amplitude, measuring the forces on the ship. The added mass and damping coefficients were then determined from the in-phase and out-phase parts of the force. In addition, experiments were performed in regular waves, measuring the motions, where the ship was kept at its positions by means of very soft springs. Drift forces were not measured by Van Oortmerssen. Experimental results of drift forces for the same ship and water depth are obtained from Pinkster and Huijsmans (1992).

Numerical results to compare with have been obtained with the frequency-domain panel model DELFRAC (Pinkster, 1995). These computations have been performed on the same mesh of the hull as for the time-domain calculations to exclude possible differences in the results due to a different description of the hull. The mesh on the mean wetted hull consists of 1042 quadrilateral panels, see Figure 5.1. The intersection of the hull with the free surface is described with 104 water line segments. The time step for all time-domain calculations $\Delta t = 0.42$ s or $\Delta t\sqrt{g/L} = 0.075$.

5.1.1 Hydrodynamic coefficients

Figure 5.2 shows the impulse response functions for calculations using either the direct formulation or the indirect source potential formulation. The oscillatory tail of the result does not indicate any physical behaviour, but it is due to effect of the first irregular frequency. Clearly, this effect is much stronger for the source potential

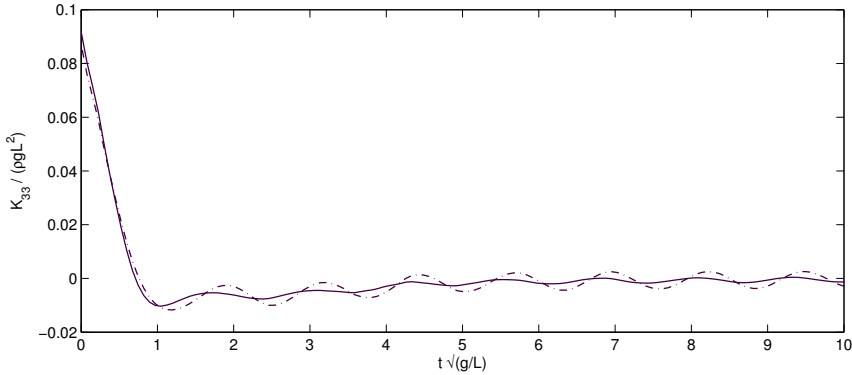


Figure 5.2: Heave impulse response function; — direct formulation, · - · indirect formulation.

formulation, so that it is chosen to perform all other simulations in this chapter with the direct formulation. To eliminate unrealistic low-frequency damping, the mean value of the impulse response functions is subtracted from the results, so that the zero-frequency radiation damping is equal to zero by definition.

In Figures 5.3 and 5.4 the non-zero terms of the computed added mass and damping coefficients, a and b , are given and compared with a DELFRAC calculation and the model test data of Van Oortmerssen. The Fourier Transform has been applied on the computed impulse response functions to obtain the frequency-dependent hydrodynamic coefficients:

$$a_{kj}(\omega) = A_{kj} - \frac{1}{\omega} \int_0^{\infty} K_{kj}(t) \sin \omega t dt \quad (5.1)$$

$$b_{kj}(\omega) = \int_0^{\infty} K_{kj}(t) \cos \omega t dt \quad (5.2)$$

Generally, the results agree well with the DELFRAC computations. The fact that the results are close is expected because both methods are based on the same linear wave theory, only a few more discretization steps are required for the time-domain method to obtain the hydrodynamic coefficients. Significant differences are only observed for some of the off-diagonal terms and for the roll damping, which are all small forces. A further difference is the fact that the frequency-domain results are obtained with the source potential method. Time-domain results with the source potential method (not plotted here) are generally in between the plotted time- and frequency-domain results.

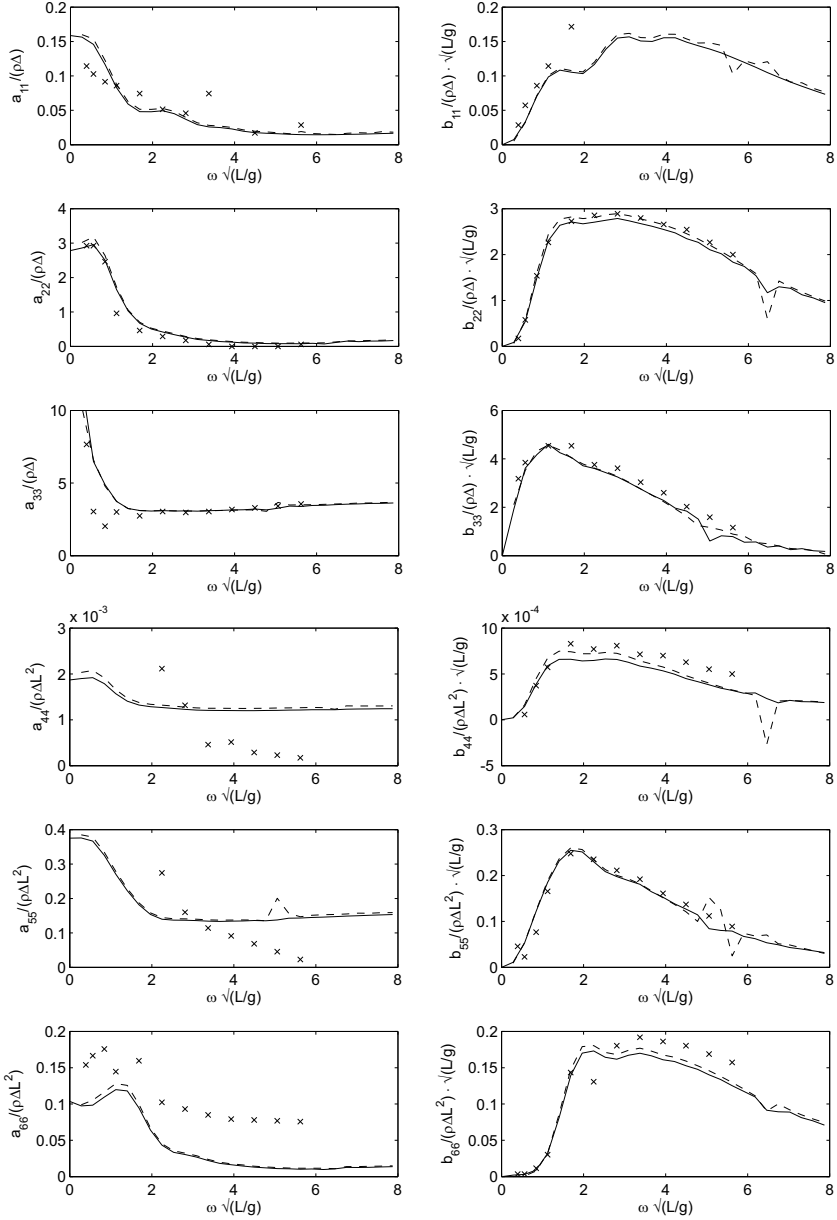


Figure 5.3: Diagonal terms of the added mass and damping coefficients; — time-domain calculation, - - frequency-domain calculation (DELFRAC), × measurements Van Oortmerssen.

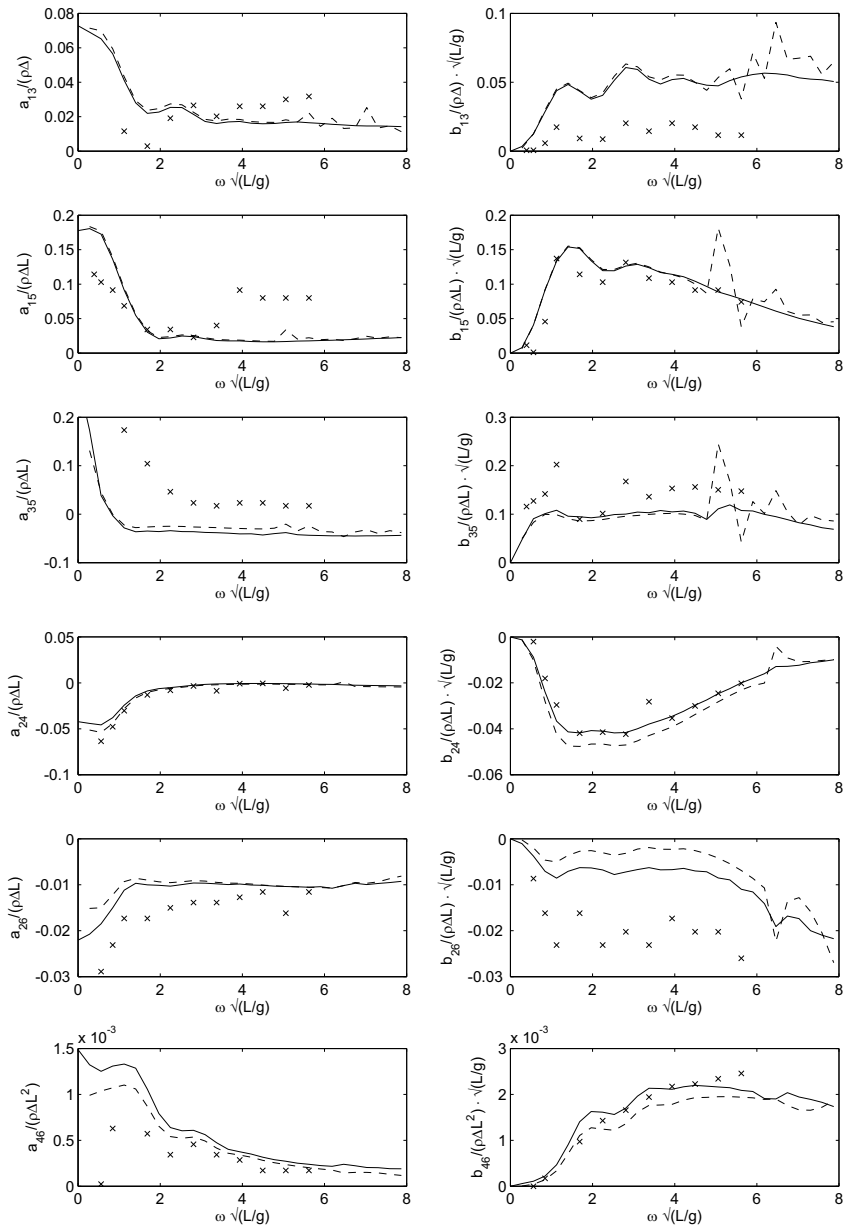


Figure 5.4: Off-diagonal terms of the added mass and damping coefficients; legend as in Figure 5.3.

Both methods correspond rather well with the measurements. Large differences occur for some of the off-diagonal terms, because these small forces are difficult to measure accurately. It is not clear why the results for the added masses of roll and pitch disagree so much, whereas the damping for these directions correspond well. Also the calculations of Van Oortmerssen disagree with his measurements for these added mass coefficients.

The influence of irregular frequencies has not fully disappeared with the chosen number of panels and time step size; for a smaller number of panels or a larger time step their influence is larger. A small dip is still observed in the graph of the damping for sway and heave, but it has reduced to workable proportions. The influence of irregular frequencies is much larger for the DELFRAC results. Of course it is possible to remove this influence in the frequency-domain by applying a lid on the free surface inside the body. This has not been done for the computations shown here to indicate the positions of the irregular frequencies and the difference of their influence in comparison with time-domain calculations.

5.1.2 Ship motions

The calculated motions of the ship in regular waves are shown in Figure 5.5 for head waves and Figure 5.6 shows the motions for bow quartering waves. Similar to the frequency-domain calculations the motions for the time-domain calculations are obtained from the solution of the equation of motion in the frequency-domain:

$$\sum_{j=1}^6 \left[-\omega^2 (M_{kj} + a_{kj}(\omega)) \tilde{X}_j + i\omega b_{kj}(\omega) \tilde{X}_j + C_{kj} \tilde{X}_j \right] = \tilde{F}_k, \quad k = 1, 2, \dots, 6 \quad (5.3)$$

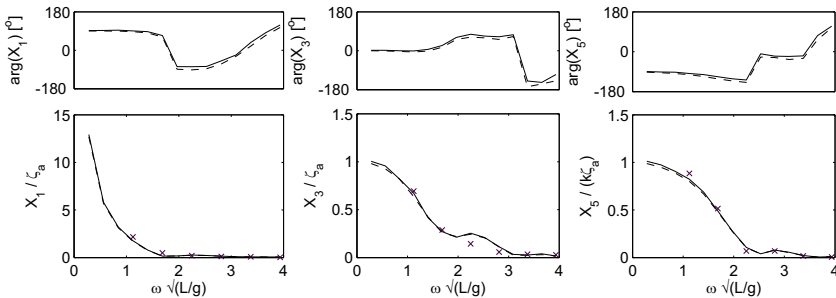


Figure 5.5: Response amplitude operators, $\theta = 180^\circ$; legend as in Figure 5.3.

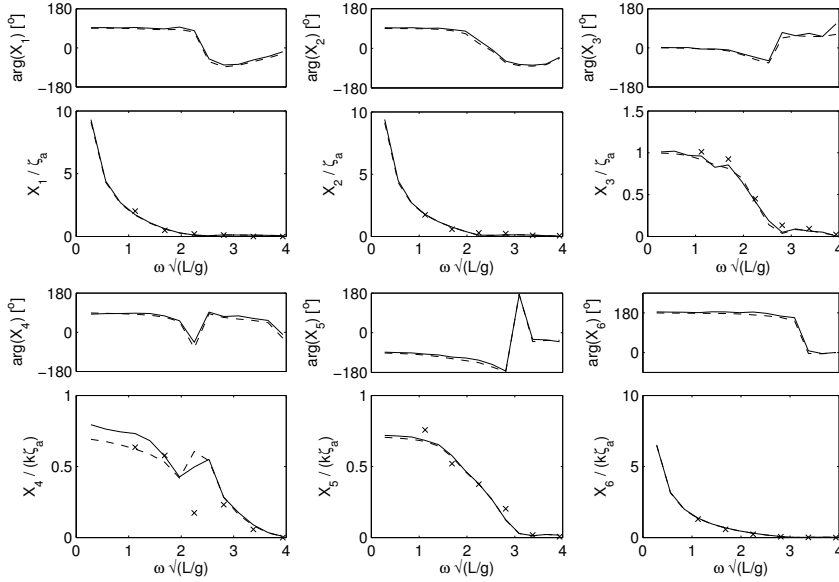


Figure 5.6: Response amplitude operators, $\theta = 225^\circ$; legend as in Figure 5.3.

Here the tilde $[\tilde{\cdot}]$ indicates that it is a complex amplitude, thus including the phase difference with respect to the incident waves. The calculated motions are in good correspondence with the frequency-domain computations as well as with the model test data. Differences between the two methods are only observed for low-frequency roll motions, but it is reminded that the plotted motions are relative to the wave number k . The absolute roll motions are very small for these low frequencies. Furthermore, it appears that the roll motions are very sensitive to the calculated phase angles of the roll and sway forces. The influence of viscous damping has been neglected in all calculations. Viscous roll damping should be included when dealing with large roll motions which are hardly damped by the small radiation damping.

5.1.3 Drift forces

Calculated horizontal drift forces are given in Figure 5.7 for head waves and Figure 5.8 for bow quartering waves. The results are also compared with computational results of Sieravogel (1998). Those results are obtained with a linear Rankine panel model. The model has been developed to compute the drift forces on a ship with small forward speed, but it is also possible to use the model for cases without forward speed. The

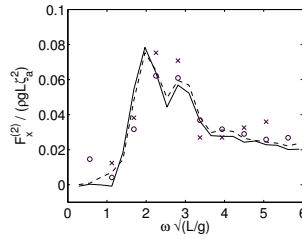


Figure 5.7: Drift force, $\theta = 180^\circ$; — time-domain calculation, - - frequency-domain calculation (DELFRAC), \circ calculation Sierevogel, \times measurements Pinkster & Huijsmans.

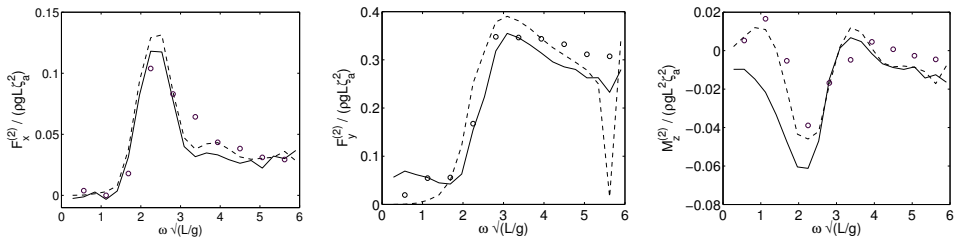


Figure 5.8: Drift forces, $\theta = 225^\circ$; legend as in Figure 5.7.

calculations have been performed for the same ship, but with a different description of the hull including 520 panels. Measured data are obtained from Pinkster and Huijsmans (1992) for the surge drift force in head waves. Measured data for other wave directions with this small water depth are not available from literature.

The computation of the drift force requires the necessary products of first order contributions in Eq. 4.33. The first order motion then is the motion as given in Figures 5.5 and 5.6. However, such a procedure would be much more complicated for the analysis of the drift forces on a moored ship in irregular waves, where the horizontal motions consist of first order wave frequency motions and motions close to the natural frequency of the mooring system. The low-frequency displacements can become very large if a soft mooring system is applied. As an assumption the contribution of the first order horizontal displacements is neglected in the computation of the drift force.

The results of the surge drift forces are in good correspondence with the measurements and the simulations with other models. The contribution of first order horizontal displacements is very small for the surge drift forces. The small differences are mainly found in the computation of velocities along the hull. The results of drift

forces for sway and yaw disagree in some respect from the other simulations. At the very low frequencies this is due to the fact that the contributions related to first order motions are not treated correctly. At the higher frequencies the sway drift forces differ a little due to the computation of the velocities. The influence of the first irregular frequency is observed in the result of the drift force for sway. This influence is only very small for the time-domain computation. Again, the effect can be removed in frequency-domain computations by applying a lid on the free surface inside the ship.

5.2 Panamax container ship in a harbour

Computational results for a Panamax container ship are compared with the model test measurements as described in Chapter 2. The calculations are performed for the ship in the harbour basin in order to prove that the model is capable to treat multi-body diffraction and wave propagation in a partly closed basin. Because the water depth in the basin is constant, the incident waves can be treated as linear waves to calculate the first order wave forces on the ship. In cases where the water depth is not constant or when second order effects are of greater importance, the incident waves should be treated by a nonlinear wave model, such as a Boussinesq model, describing the pressures and velocities at the hull of the ship. In this case the incident waves are prescribed at the ship as well as on the harbour basin walls and the diffraction by the ship and the walls is treated simultaneously.

The submerged hull of the ship is described by 576 panels and the basin walls are described by 730 panels, see Figure 5.9. The panels at the stern of the ship are

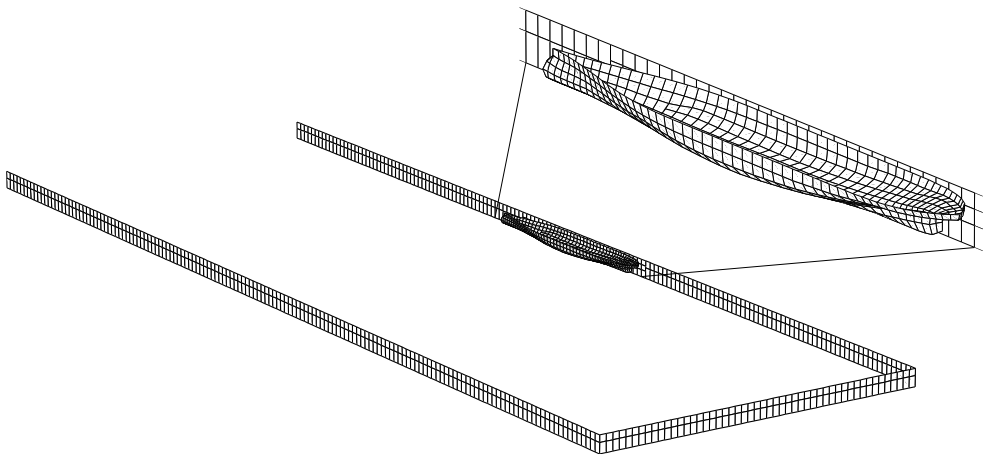


Figure 5.9: Panel description of the container ship and the harbour walls.

lowered over a short height to cancel out numerical difficulties to treat the panels close to the free surface. Only the inside of the walls is described which means that the thickness of the walls is neglected. Also the effect of the slope at the outside of the harbour on the waves inside the harbour is neglected. The panels on the wall close to the ship are a little smaller, because larger vertical velocities are expected in the vicinity of the ship. The time step for all calculations $\Delta t = 0.51$ s or $0.1\sqrt{L/g}$. The results are given on prototype scale.

Hydrodynamic analysis of a ship in close proximity of another floating body or a fixed structure is always influenced by viscous effects which are initially not taken into account in panel models. The fluid velocities in the narrow gap between the two bodies are much larger than at other places so that viscous damping at the keel of the ship and skin friction are not negligible. To reduce the wave amplitudes in the gap a few options are possible in frequency-domain calculations. Malenica et al. (2005) lower the vertical velocities at panels at the free surface for which the free surface boundary condition is slightly modified. This reduces the resonance between the two bodies to values which are much closer to measured wave amplitudes. They also mention modification of the body boundary condition, but computational results are not provided.

In time-domain calculations a mesh at the free surface is not possible, because of the singularity of the Green function here. However, changing the body boundary condition is possible. In order to reduce the resonance in the gap, Green's theorem is modified in such a way that the fluid is able to 'leak' into one of the bodies:

$$(1 + \varepsilon_x)2\pi\phi(\vec{x}, t) + \int_{-\infty}^t d\tau \iint_{\mathcal{H}_0 + \mathcal{W}_0} (\phi G_{n_\xi} - \phi_{n_\xi} G)(1 - \varepsilon_\xi) dS_\xi = 0 \quad (5.4)$$

with ε a transmission parameter which can range in values between 0 and 1. $\varepsilon = 0$ corresponds to full reflection and $\varepsilon = 1$ corresponds to full transmission. This solution may be physically not correct, because the calculated fluid velocities close to the boundary are no longer directed exactly parallel to the boundary, but it can effectively reduce the wave elevations in the gap to more realistic values.

5.2.1 Impulse response functions

In the model tests the ship was fixed to its position, so there are no measured data available of the hydrodynamic properties of the ship. Nevertheless, computational results are interesting to show here. The impulse response functions are given in Figure 5.10 for sway and heave. $K_{23}(t)$ is the force in sway due to an impulsive

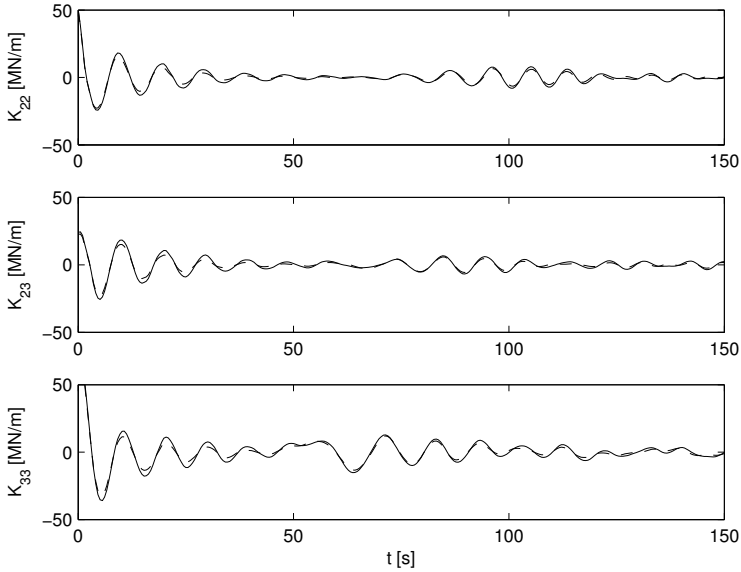


Figure 5.10: Impulse response functions for sway and heave; — $\varepsilon = 0$, - - $\varepsilon = .02$ at the wall close to the ship.

displacement in heave. The results indicate that the force decays much slower than for a ship in open water. The oscillations in the first 50 s are due to resonance of the fluid in the gap between the ship and the wall and underneath the ship. The oscillations after 50 s are due to waves that have been reflected at the wall on the other side of the harbour. The time for the wave front to travel this distance is 54 s. Apparently, these waves are first noticeable in the heave forces. The sway forces gradually grow in the period after the front has arrived due to the fact that resonance is building up in the gap between the ship and the wall.

The effect of a small non-zero value of the transmission parameter ε at the wall close to the ship is observed after a few oscillations. Near $t = 0$ there is hardly any difference, but after a few oscillations a considerable amount of energy has leaked through the wall. The reduction is near the resonant frequency and it can therefore approximate the energy loss due to friction and turbulence which also occur near the resonant frequency.

5.2.2 Wave forces

Calculations have been carried out for two wave conditions corresponding to test N° 4.3.1.1 and 4.3.3.2: $H_s = 3$ m, $T_p = 10$ s, $\theta_0 = 90^\circ$, with a directional spectrum proportional to $\cos^2(\theta - \theta_0)$ and $H_s = 3$ m, $T_p = 15$ s, $\theta_0 = 60^\circ$, spreading $\sim \cos^4(\theta - \theta_0)$ respectively. The mean wave directions with respect to the wavemaker, $\theta_0 = 90^\circ$ and 60° , correspond to 240° and 270° in the ship bound coordinate system.

Time series of incident waves for the simulations have been generated from the theoretical JONSWAP spectrum and the directional spectrum with random phase and prescribed at the collocation points of the panels on the ship and the basin walls. Second order low-frequency waves have been added; the wave amplitudes are based on the undisturbed waves. Also these waves are assumed to follow linear wave theory. This is not true outside the harbour, where these waves are bound to the short waves. However, at the harbour mouth the long wave partly becomes free and can resonate in the harbour. The long waves have been added in the simulation only for the sake of completeness. The focus in the comparison with the measurements is on the first order wave forces.

For simulations with such a large domain it is important to choose a correct length of the kernel in the convolution integrals involving the Green function. For accurate computation of the diffraction of the incident waves in the harbour, the kernel should include the time of a wave to travel from one to the other side of the harbour. In this case the time for a wave with period $T = 10$ s to travel over a distance of 1260 m is 104 s. The chosen length of the kernel in the simulations is 127.5 s. Simulations with much longer kernel lengths invoked memory allocation problems, because the array of Green functions became too large, and were therefore not possible. The total simulation time is 100 minutes using the direct formulation.

The walls are initially assumed as fully reflective. If all boundaries would be assumed as fully reflective, viscous effect are neglected and the simulations overestimate the measured forces. Especially near the gap between the the ship and the wall, viscous effects are not negligible. To approximate this effect the transmission coefficient ε at the wall close to the ship is tuned for the sway forces, because the sway forces are highly influenced by the water levels in the gap; all other boundaries are still assumed fully reflective. A summary of the results for both simulations is given in Tables 5.2 and 5.3. The significant wave force amplitude is defined as $F_{k,s} \simeq 2\sqrt{m_0}$ with m_0 the zeroth moment of the wave force spectrum. A small value of ε leads to a considerable reduction of the sway and heave forces, because the wave heights in the gap are reduced. The effect on the forces in the other modes is much less.

Table 5.2: Significant wave forces, $F_{k,s}$, for test 4.3.1.1.

mode	unit	measured	calculated		calc. $\varepsilon = .02$ relative to	
			$\varepsilon = 0$	$\varepsilon = .02$	measured	$\varepsilon = 0$
surge	MN	4.6	5.5	5.0	1.088	.901
sway	MN	29.6	41.9	32.1	1.084	.766
heave	MN	40.1	56.4	43.0	1.073	.764
roll	MNm	70.6	71.2	63.1	.893	.886
pitch	MNm	2231	2783	2469	1.106	.887
yaw	MNm	1717	1922	1662	.968	.865

Table 5.3: Significant wave forces, $F_{k,s}$, for test 4.3.3.2.

mode	unit	measured	calculated		calc. $\varepsilon = .02$ relative to	
			$\varepsilon = 0$	$\varepsilon = .02$	measured	$\varepsilon = 0$
surge	MN	4.9	5.4	5.1	1.054	.948
sway	MN	19.3	22.7	19.6	1.016	.865
heave	MN	50.9	55.2	49.9	.981	.904
roll	MNm	40.1	41.3	38.8	.965	.938
pitch	MNm	2129	2374	2252	1.058	.949
yaw	MNm	1110	1085	1013	.912	.933

A value of ε of .02 appears to be a good value for both simulations to obtain more realistic wave forces. However, that does not necessarily indicate that this value is always recommended. Viscous damping is usually quadratically related to the wave height and the transmission coefficient provides a linear reduction of the wave forces. Therefore, different values can be found for different wave conditions.

Spectra of the wave forces are given in Figures 5.11 and 5.12. The calculations predict the correct peak frequencies of the wave forces and approximate the height of the peaks. Apparently, despite the fact that the use of a transmission coefficient may physically not be correct, the proportional reduction of wave energy in the vicinity of the gap between the ship and the quay is at the correct wave frequencies.

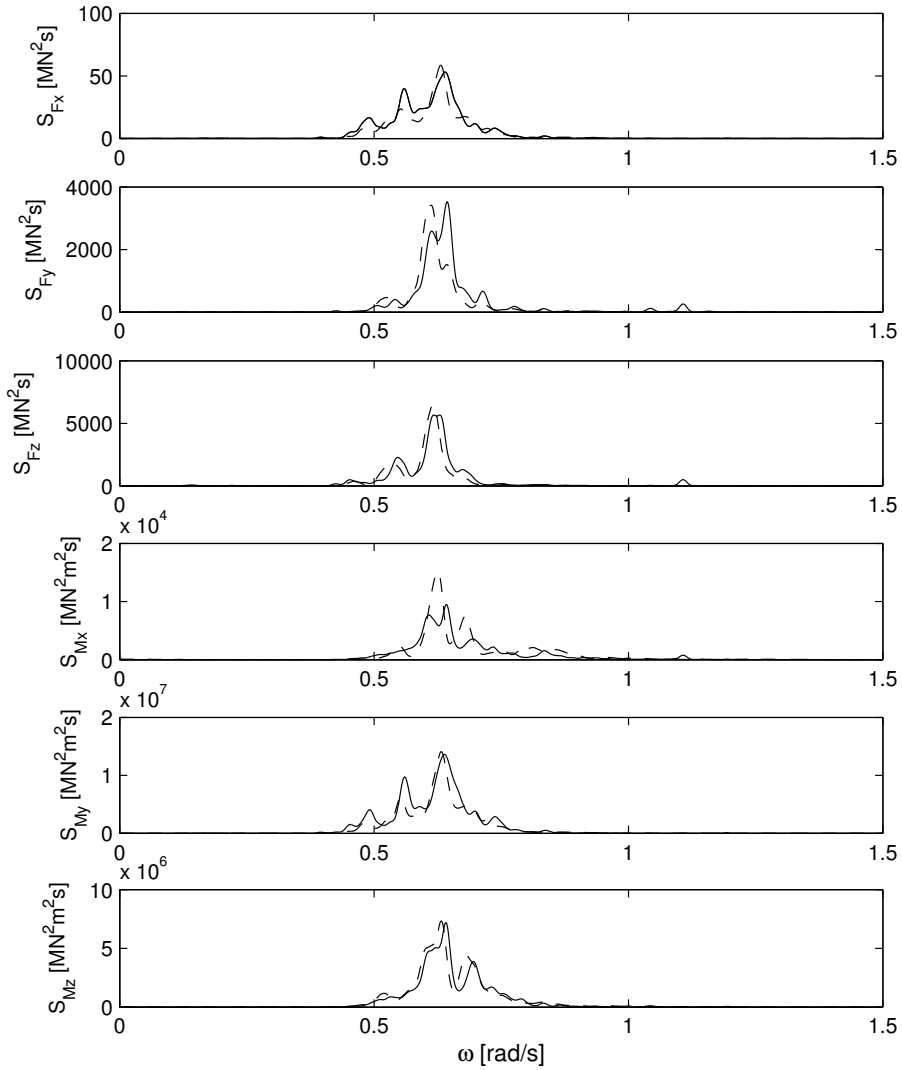


Figure 5.11: Spectra of the forces and moments on the container carrier in the harbour for tests 4.3.1.1; -- measurements, — calculation with $\varepsilon = .02$

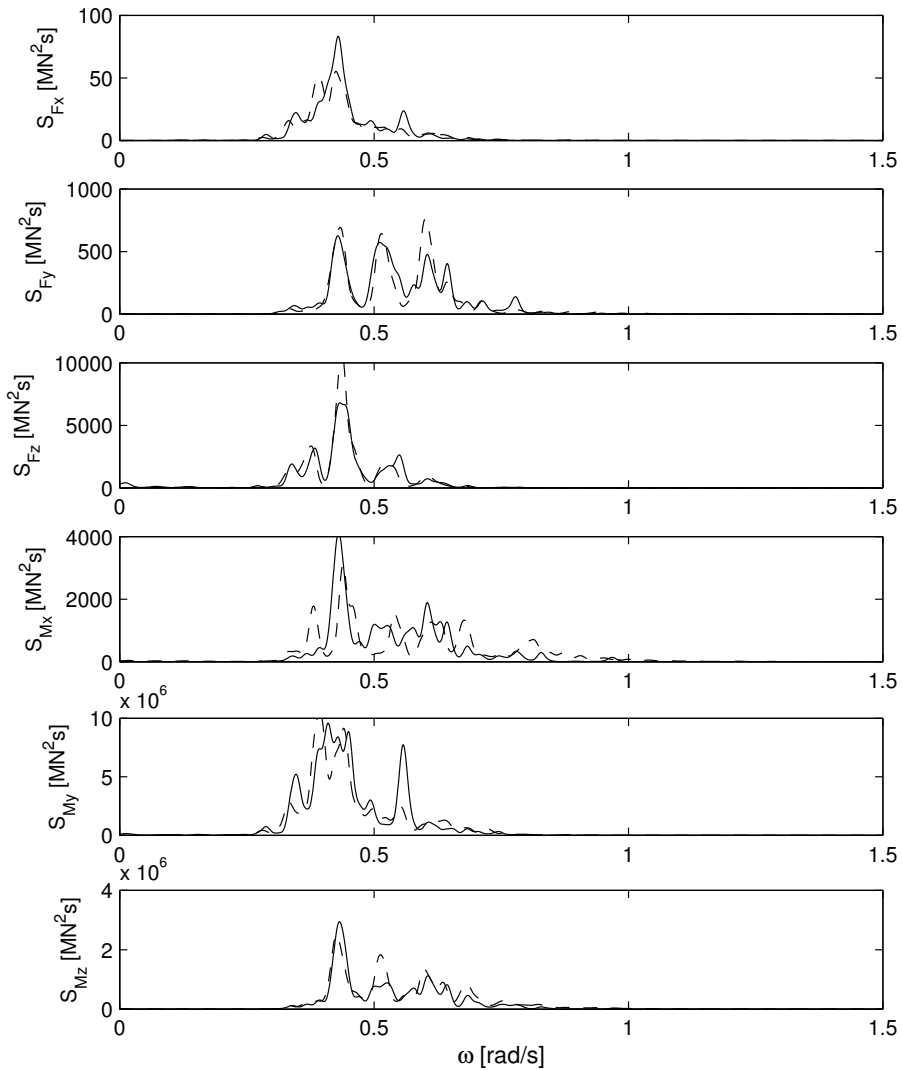


Figure 5.12: Spectra of the forces and moments on the container carrier in the harbour for tests 4.3.3.2; -- measurements, — calculation with $\varepsilon = .02$

6. VALIDATION OF THE BOUSSINESQ-PANEL MODEL FOR NONLINEAR WAVES

To validate the computational method to determine the wave forces in an arbitrary wave field calculations have been carried out for the forces on a Panamax container carrier due to waves generated by a passing ship. For further verification results are presented of the forces on a 125,000 m³ LNG carrier in irregular short-crested waves. In both cases the propagation of the incident waves is treated with the Boussinesq-type wave model TRITON, not taking into account the presence of the moored ship. The deformation of the wave field by the moored ship is treated with the time-domain panel model. In this fashion the first order forces can be obtained as well as second order forces due to bound harmonics in the incident wave field and varying drift forces.

The validation is presented for two cases in open water. Results of wave forces on a moored ship in a harbour are not presented in this Chapter, because TRITON results obtained for such a situation were not available. The coupling to the panel model will then be done in the same manner as described in this Chapter, only the waves scattered by the ship are also influenced by the harbour walls.

6.1 Forces on a container carrier due to a passing ship

Computational results of waves and wave forces on the container carrier are compared with model test measurements as described in Chapter 2 for waves generated by a passing ship corresponding to test N^o 2.5.2. The passing ship moves at a supercritical speed of depth-based Froude number $F_n = 1.5$. Similar to the generation of irregular waves, for this test the waves are also generated at the waveboard. Irrespective of the fact that the test does not represent a real passing ship moving at high speed, the conditions are very suitable for validation of the computational method.

6.1.1 Wash waves

Concerning the disturbance induced by a passing ship two effects can be distinguished. The first effect is due to the primary flow and the associated pressure drop around the passing ship. The influence of the primary flow is rather local, but can lead to problems at a larger distance due to the generation of seiches in a harbour basin with the entrance close to the shipping lane (Pinkster, 2004). The second effect is formed by the Kelvin waves, also known as wash waves. These waves become more important for increasing speeds. The wash waves propagate almost without dissipation, so that their influence is also felt at larger distances from the shipping lane. In the simulated case only the wash waves have been calculated.

For $F_n < 1$, i.e. for a ship sailing at subcritical speed, the Kelvin wave pattern consists of diverging bow and stern waves and transverse waves travelling virtually parallel to the ship. The angle between the wake behind the ship and the Kelvin envelope is constant for all subcritical speeds and equal to 19.5° at deep water. The Kelvin envelope describes the line through all cusps where crests of bow and transverse waves intersect. For increasing Froude numbers the transverse waves become much higher and the wedge describing the influence area of the transverse waves becomes much wider. At $F_n = 1$ the wedge describes a wide wave front propagating virtually parallel to the ship and the transverse waves in the wake behind the ship have disappeared. Beyond $F_n = 1$ the wedge becomes narrower again, because the waves cannot keep up with the speed of the ship.

For $F_n = 1.5$ the theoretical wave direction of the front $\theta = 48.2^\circ$ with respect to the heading of the passing ship, see Figure 6.1. This corresponds to a wave direction of 281.8° in the ship-bound coordinate system of the container ship.

For wave modelling in TRITON, the surface elevations must be prescribed at the wave boundary. This is achieved by deriving the incident wave boundary condition from the waveboard movement. The relation between the paddle movement x_p and the surface elevation ζ is deduced from linear long-wave theory,

$$\zeta = \frac{dx_p}{dt} \sqrt{\frac{h}{g}} \quad (6.1)$$

thus describing a crest at the bow and a trough at the stern radiating away from the ship. The model domain consists of 145×240 grid cells of 11×11 m² each. The time step is 1 s. All values are at prototype scale using Froude scaling.

The wave elevations at the location of the CoG of the container ship are given in Figure 6.2. The measured data are obtained during the simulation that was resumed

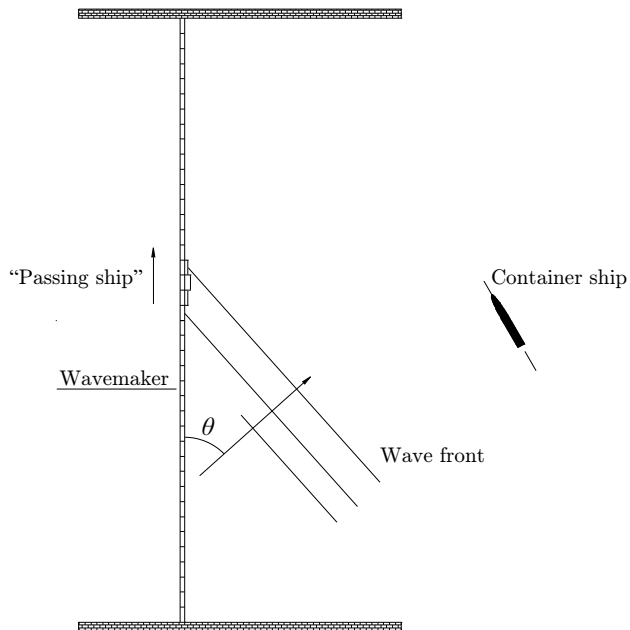


Figure 6.1: Plan view of the waves generated by the passing ship at the wavemaker in the basin.

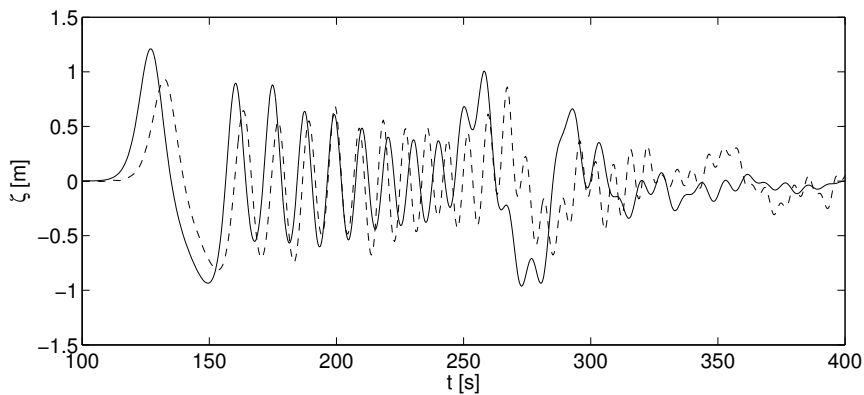


Figure 6.2: Free surface elevations at the position of the CoG of the container ship; — TRITON calculation, -- measurements.

under the same conditions, but without the container ship. Time $t = 0$ corresponds to the moment at which the ship starts to move along the wavemaker. The first crest to arrive is the bow wave followed by a trough due to the depression at the stern of the passing ship. These waves are highly dispersed over the long travelling distance between the wavemaker and the container ship; the low-frequency components of the disturbance at the passing ship arriving first followed by higher frequency waves. At $t \simeq 260$ s another long wave is observed. This is the bow wave that has been reflected against the side wall of the wave basin. The direction of this wave is 198.2° in the ship-bound coordinate system.

The wave pattern with the dispersed wash waves and the reflected waves from the sidewall is also observed in the calculation, only with a small phase lag with respect to the measured wave elevations. For these rather long waves TRITON predicts the correct wave celerity regarding linear wave theory, so that there is no direct clarification for this phase lag, which is nevertheless small with respect to the travelling time of the waves from the wavemaker to the container ship.

6.1.2 Wave forces

The velocities and pressures in the undisturbed wave from the TRITON calculation are written to file for the period between $t = 100$ and 400 seconds at the collocation points of all panels on the hull of the container ship. In the same time interval the free surface elevations at the midpoints of the waterline segments are written to file. The wetted hull of the ship is divided into 576 panels and 104 waterline segments for the time-domain calculation, see Figure 6.3. This is the same mesh as used in Section 5.2. The panels at the stern of the ship are lowered a little to avoid numerical instabilities at panels close to the free surface. The time step in the diffraction calculation is 0.38 s or $0.075\sqrt{L/g}$. The direct formulation is used for the determination of the scattered potentials. The cut-off period of the convolution integrals is 51 s.

For the frequency-domain calculations with DELFRAC a different mesh is used with 1466 panels and 102 waterline segments. The mesh is different, because frequency domain computations allow less restrictions regarding the position and the angle of panels intersecting the free surface. A lid on the free surface inside the ship is applied to eliminate inaccuracies near irregular frequencies. For the Fourier analysis of the normal velocities not only the 300 s period is analysed, but it is extended at the beginning and at the end with 100 s with normal velocities $v_n = 0$. A Fourier analysis assumes a repetitive motion, so that inaccuracies arise when this is not the case. The errors occur at the beginning and at the end of the analysed period. Therefore, if

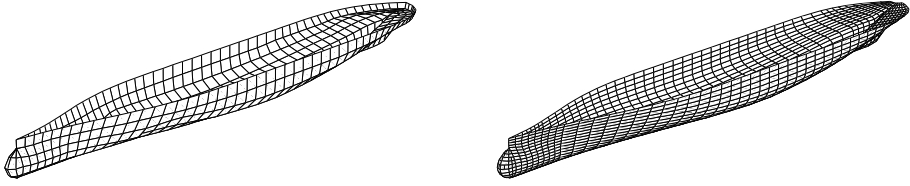


Figure 6.3: Panel descriptions of the Panamax container carrier for the time-domain calculation with 576 panels (left) and for the frequency-domain calculation with 1466 panels (right).

the analysed period is extended, the inaccuracies occur in periods which are not of interest.

The results are given in Figure 6.4. The sway forces are large in these almost beam waves. Only the waves that have been reflected against the sidewall are nearly bow-on and lead to larger surge and pitch forces. The calculated forces are the sum of first and second order contributions. Generally, there is good correspondence between the calculated and measured forces. The phase lag is equal to the phase lag between the calculated and measured waves at the CoG of the ship. The measured roll moments are larger, probably due to the difficulties in determining the roll moment from the forces in the force transducers. Small differences in the yaw moments can easily occur because the waves are nearly beam-on and the yaw moments are therefore relatively small. The results of the time and frequency-domain computations are nearly identical. Therefore, the dotted line of the frequency-domain results is not well visible in Figure 6.4.

The contribution of the second order horizontal forces is given in Figure 6.5 for both computational methods; it is virtually impossible to deduce the second order contributions from the measured forces. The major part of the force amplitudes is a double-frequency contribution, but there is also a (less visible) slowly varying drift force. Apparently, there is hardly any difference between the time and frequency-domain methods, despite the fact that the panel distributions are not identical.

6.2 Forces on an LNG carrier in irregular short-crested waves

Calculations have been carried out for an LNG carrier in irregular short-crested waves to verify whether the computational method is able to deal with longer time series of wave forces. The incident wave spectrum is a JONSWAP spectrum ($\gamma = 3.3$) with

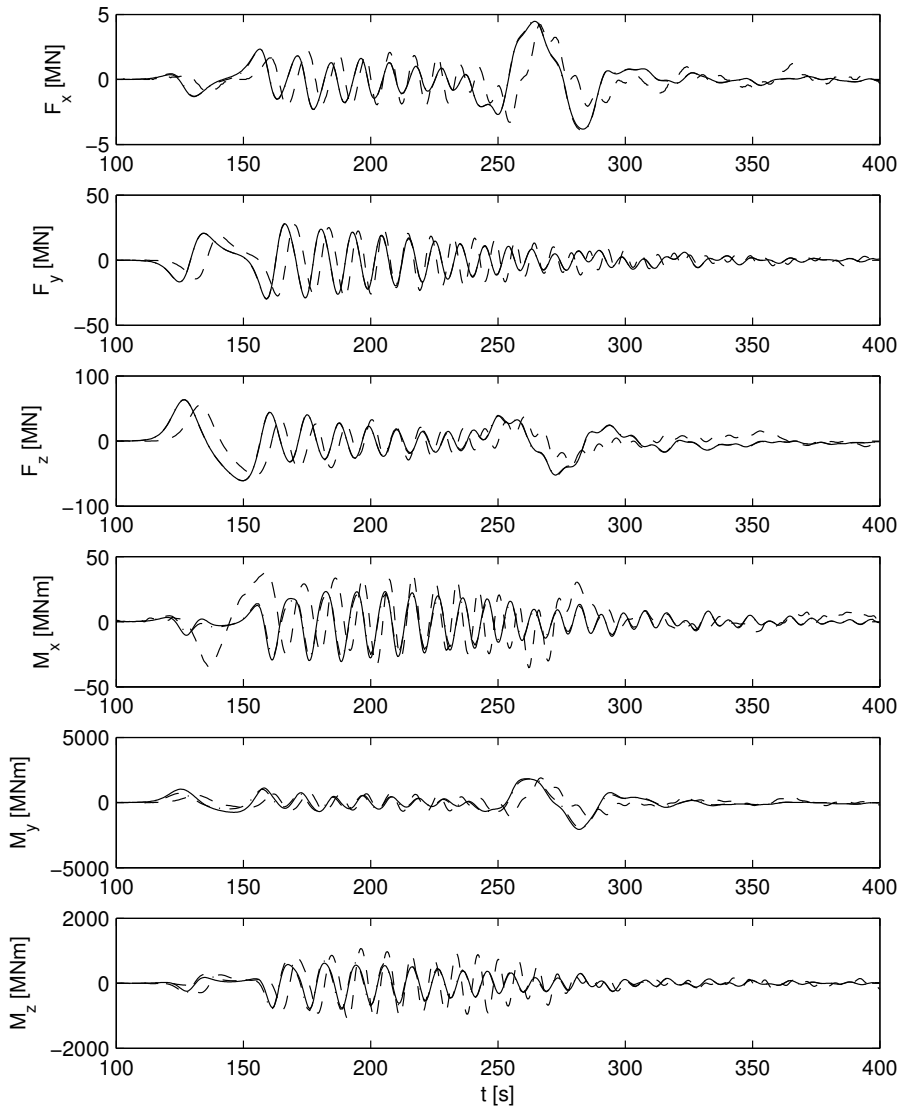


Figure 6.4: Total wave forces on the container ship; — time-domain calculation, · - · frequency-domain calculation, - - measurements.

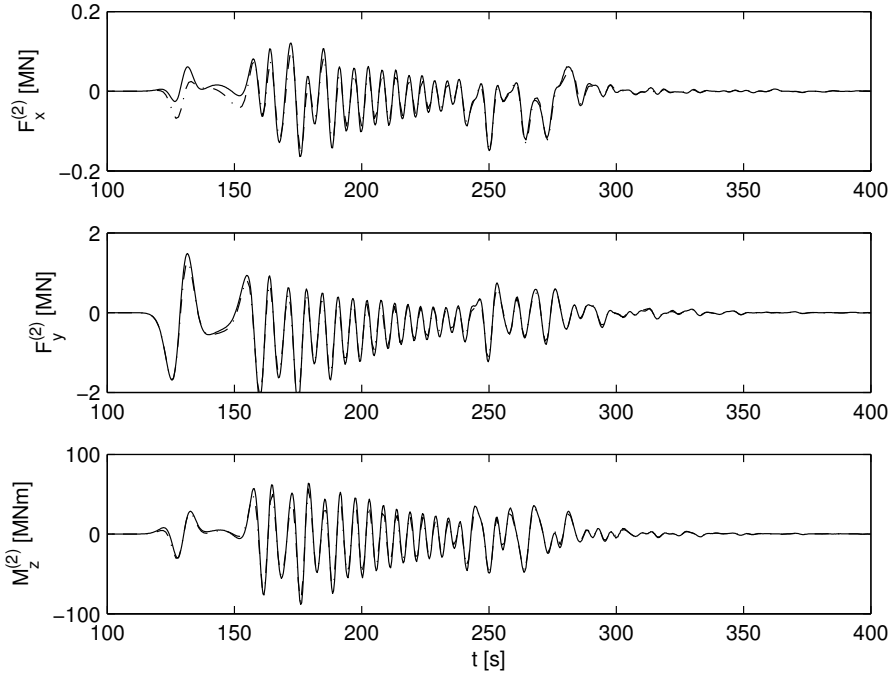


Figure 6.5: Second order wave forces on the container ship; — time-domain calculation, · · · frequency-domain calculation.

a significant wave height $H_s = 1.5$ m, peak period $T_p = 15$ s, mean wave direction $\theta_0 = 180^\circ$ (bow-on) with a spreading proportional to $\cos^4(\theta - \theta_0)$. The particulars of the 125,000 m³ LNG carrier are given in Table 3.4 and the body plan is presented in Figure 3.15. There are no measured data available for this case to compare with.

The domain for the TRITON computation is a rectangular basin with a length of 900 m, a breadth of 600 m and a uniform water depth of 15 m. The boundaries at the sides are closed and the boundary opposite of the wave generating boundary is open. This domain more or less represents a wave basin, where it is assumed that all wave energy is effectively absorbed at the end of the basin. Concerning prototype modelling for e.g. an LNG jetty in open, shallow water, the model domain needs to be wider to remove unintended effects of the side walls. The position of the CoG of the ship is 610 m from the wave generating boundary in the middle between the side boundaries. The domain is discretized with 150×100 grid cells of 5×5 m² each. The time step is 0.50 s and the simulation period is 3740 s. At the wave generating boundary

the waves are prescribed as surface elevations obtained with wave components based on the theoretical JONSWAP spectrum with random phase. It is emphasized that linear waves are prescribed at the boundary. Nonlinearities such as the bound long wave take effect in the propagation of the wave, but also a spurious free long wave with opposite phase is generated in about the same manner as in a physical model (Barthel et al., 1983). Because the group celerity of the short waves and the wave celerity of the free long wave do not deviate much in relatively shallow water, the long-wave action in the basin is underpredicted. Nevertheless, linear input signals are used here, because it is not the intention to reproduce the correct waves, but only to verify the modelling chain and the differences between the time and frequency-domain approaches. Influences of reflections from the coast could be taken into account by modelling the actual bathymetry, so that breaking of short waves and enhancement and reflection of long waves is taken into account.

For the determination of the wave forces the hull is discretized with 1134 panels and 126 waterline segments, see Figure 6.6. Pressures and velocities are obtained on the collocation point of each panel with a time step of 1 s. The same time-step is used for storage of the surface elevations at the waterline. For the time-domain and the frequency-domain model the same input data are used.

Time-domain diffraction computations have been performed using the direct formulation with a time step of 0.32 s or $0.06 \sqrt{L/g}$. The cut-off period of the convolution integrals is 105 s. The first order wave forces are obtained directly from the incident wave pressures from TRITON (Froude-Krylov force) and calculated pressures in the scattered wave (diffraction force). For the determination of the second order wave forces, which include terms proportional to vertical body movements and pressures and velocities in the radiated wave, the ship is assumed as free floating. A very soft mooring system is applied to prevent the ship from drifting away in the computation.

Frequency-domain computations with DELFRAC have been carried out on the same mesh with an added irregular frequency lid. To speed up the Fourier transformations, the simulation period is split into 5 overlapping segments of 1024 s (also 1024 samples) long. Then, the overlap between two segments is 345 samples. The overlap is introduced to overcome inaccuracies and large fluctuations of the diffraction forces at the position where two segments are connected. In the overlapping zone the resulting force gradually changes from the force obtained in the prior segment to force obtained in the latter segment. The matching frequency step size is 0.006136 rad/s and the Nyquist frequency is 3.142 rad/s. To reduce the amount of frequencies to be treated the Fourier transforms are cut off at 1.5 rad/s, which is justified here because there is hardly any wave energy at higher frequencies. This leads to a computation

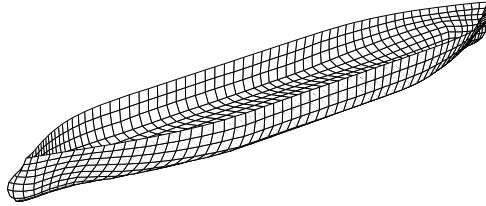


Figure 6.6: Panel description with 1134 panels of the 125,000 m³ LNG carrier.

for 244 frequencies for each segment.

The results of wave forces obtained with both methods are given in Figures 6.7 and 6.8. The first order forces are plotted separately from the second order forces. Due to the fact that low-frequency nonlinearities are included in the incident waves, the first order wave force spectra also include a low-frequency contribution. The forces for sway, roll and yaw are rather large despite the fact that the mean wave direction is bow-on. This is due to the fact that the directional spreading is large. It appears in this case with a small water depth and a rather large wave period that the contribution of the bound waves is dominant over the drift forces. The differences between both methods are very small. Significant differences are only observed in the sway and yaw drift forces.

In the time-domain results there is a very small peak in the heave spectrum near $\omega = 1$ rad/s. This peak is due to the effect of the first irregular frequency which comes into play because the kernel of the convolution integral for the determination of the scattered potentials is cut off. The instability grows gradually, so that the cut time had to be chosen at a larger value than for the calculation for the passing ship (also because the water depth is smaller). For much smaller cut off times the instabilities grow to unacceptably large values at the end of the simulation period.

6.3 Discussion

The modelling approach consisting of a Boussinesq-type wave model and a time-domain panel model to calculate the wave forces on a moored ship has been validated in this Chapter and compared with model test experiments for the forces on a moored ship due to the waves generated by a passing ship. The wave model provided good results for the waves at the location of the ship taking into account the difficult modelling of the highly dispersive wash waves. The results of wave forces obtained

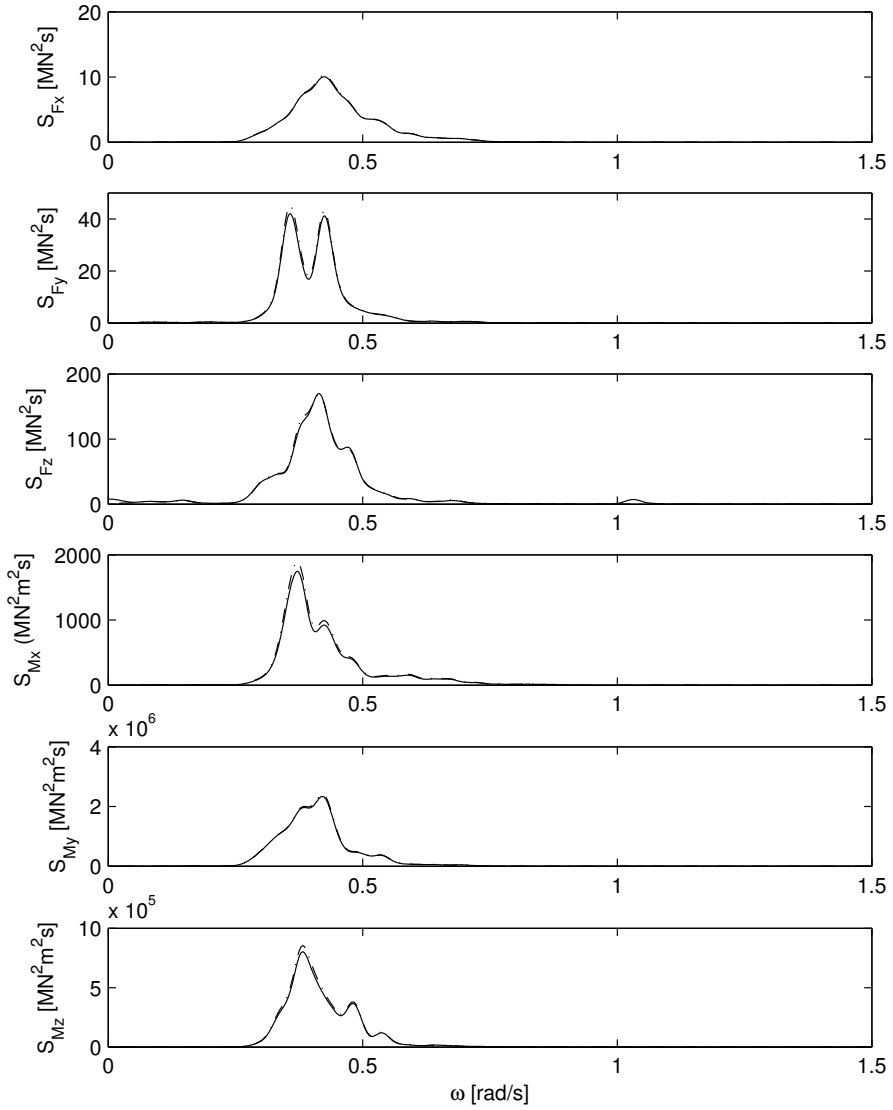


Figure 6.7: Forces on the LNG carrier: — time-domain calculation, · · · frequency-domain calculation.

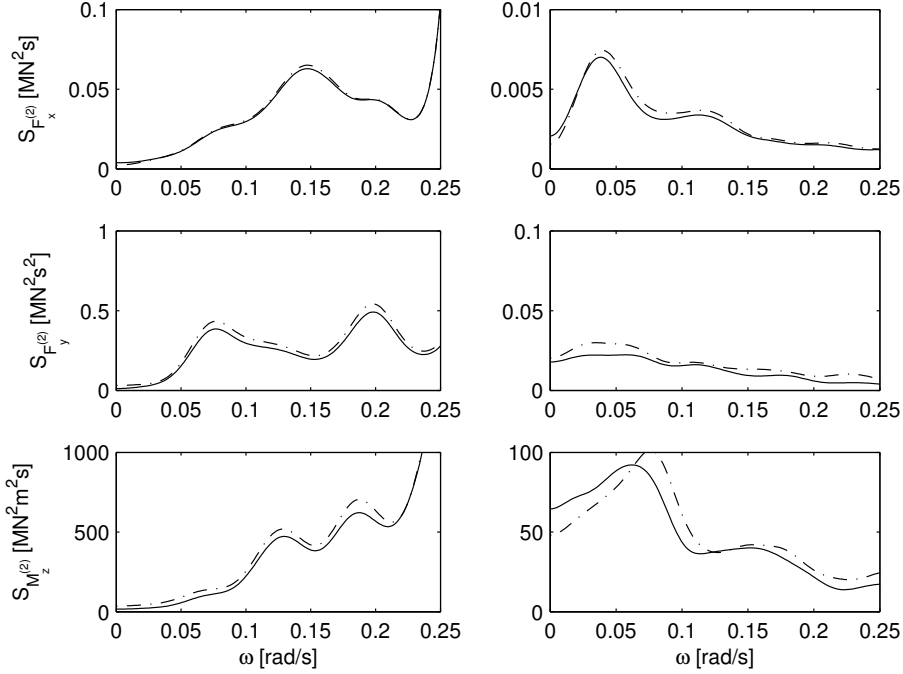


Figure 6.8: Low-frequency forces on the LNG carrier due to pressure integration of second order waves (left) and drift forces (right): — time-domain calculation, · - · frequency-domain calculation.

with input of the calculated undisturbed waves show good correspondence with the measurements: the deviations from the measured forces are about the same as the deviations found in the calculation of the incident waves.

The differences between the results of a time and frequency-domain approach for the calculation of the disturbance by the ship and the wave forces are very small. However, looking at the computational process there are a few important differences which mainly deal with the optimization of the calculation.

For time-domain computations the most important parameters (apart from the mesh of the hull and other structures) are the time step and the cut-off period of the convolution integrals. A time step needs to be chosen in such a way that the accuracy is in proportion with the accuracy in the discretization of the hull and also that the computation does not become unstable for high-frequency oscillations that occur near the free surface. This time step is often a little smaller than the time

step for the Boussinesq model calculation. The cut-off period of the convolution integrals needs to be defined in such a way that required wave information, mainly from other structures, is preserved and that irregular frequencies are suppressed. The clear choice of the input parameters leads to an unambiguous calculation. On the other hand, optimization to achieve a quicker computation is difficult, at least if the panel description is not changed.

Concerning frequency-domain computations, the division of the simulation period into overlapping segments is somewhat cumbersome. However, the results have proven to be correct or at least comparable with time-domain results. Quick optimizations are achieved with the choice of the cut-off frequency in the Fourier transforms. The frequencies above the cut-off frequency either contain only a minimal amount of wave energy or the wave forces in this range are not important because the ship does not respond to them. In this way a large part of the calculation can be omitted without losing important information. This makes the frequency-domain approach much more efficient in terms of the computational burden. Contrarily, the use of Fourier transforms implicitly means the assumption that the input signal is repetitive. At least for the treatment of forces due to waves from a passing ship this could be overcome by increasing the simulated period so that the errors are outside the period of interest.

It can be concluded that both the time and frequency-domain methods for the scattering of waves around the floating body are able to deal with the nonlinear input signals of incident waves provided by a calculation with a Boussinesq-type wave model in which the floating body is not included. The differences between the results are negligible. The frequency-domain computations are more efficient.

7. CONCLUSIONS AND RECOMMENDATIONS

7.1 Conclusions

The focus of this thesis has been on the development and validation of new computational methods to determine the behaviour of a moored ship in an arbitrary wave field and in a complex geometry, such as a harbour. Two objectives were set dealing with different accuracy levels and computational efforts:

- a method which focusses on long-period ship response, either due to free long waves or associated with wave groups at the ocean;
- a method to accurately predict the first order waves and associated second order bound waves in the harbour combined with an accurate and direct method to determine the first and second order forces on the moored ship.

Both objectives have been attained with the development of computational methods consisting of a chain of numerical models. With this approach it is made possible to utilize the strengths of the individual models, being either concerned with the wave propagation in a large area, such as a harbour, or concerned with the complex shape of the moored ship. Therefore, the waves in the harbour are calculated first with a wave model not taking into account the presence of the moored ship. The wave forces on the moored ship are subsequently found with a diffraction model, which takes into account the shape of the hull. The solutions for both objectives are treated respectively in the following subsections.

7.1.1 Moored ship response in long waves

The first method has been developed to simulate the moored ship motions due to long-wave action inside a harbour basin. The method is based on a coupling of three numerical models: (1) a depth-averaged nonlinear flow model with short-wave forcing for the calculation of infragravity wave penetration in the harbour, (2) a strip theory based method to determine the low-frequency wave forces from the computed wave

elevations and fluid motions and (3) a ship motion simulation model which takes into account the nonlinear properties of mooring lines and fenders.

Test calculations have been performed for a container ship in irregular waves to verify the strip theory formulations. Verification of the complete chain of models has been carried out against model test experiments for a container ship in a rectangular harbour and prototype measurements of long waves and surge motions of a coal carrier in Tomakomai Port, Japan. Additional calculations have been made for an LNG carrier close to the coast to show the influence of a sea bed and reflections from the coast on the low-frequency forces on the ship.

The wave forces on the container ship in the harbour did not agree with the measured forces for frequencies larger than the first natural mode of the harbour. Nevertheless, a large amount of wave energy was measured at frequencies where resonance is not expected. Probably large-scale oscillations were present in the laboratory basin, which were not simulated.

Good correspondence was found for the surge motions of the coal carrier in Tomakomai Port. Despite a significant wave height $H_s = 2.43$ m offshore and $H_{s,lf} = 0.32$ m in the harbour (which are not exceptional) the significant surge motions increased to more than 6 m. The occurrence of this event is also observed in the simulation. Due to line breaking accidents the natural surge period increased to a value close to a resonant period of the harbour basin, so that resonance of the ship could occur. Contrarily, increasing or decreasing the pretension in mooring lines can be an easy and practicable solution to decrease ship motions during loading operations in a harbour.

Calculations for the forces due to long waves forces by incoming short-wave groups on a sloping coast have shown that bathymetrical effects such as the slope of the sea bed have large effects on the low-frequency forces. The wave forces on the ship especially increase at frequencies a little larger than the beat frequency which corresponds to the period for the wave group to travel to the shore plus the period for the free long wave to return to the position of ship.

7.1.2 Moored ship response in nonlinear waves

The second method developed consists of a Boussinesq-type wave model in combination with a linear time-domain panel model. Boussinesq models allow wave propagation over an uneven bathymetry taking into account linear effects, such as wave dispersion, shoaling, refraction and diffraction, as well as nonlinear effects, such as the generation of higher and lower harmonics. The calculated pressures and velocities

at the hull of the moored ship are written to file. This file serves as input for the linear time-domain panel model that computes the interaction between the incident waves and the moored ship.

The time-domain panel model has been verified for the hydrodynamic coefficients, first order motions and mean drift forces of a 200 kDWT tanker. Comparison has been made with model test data from literature and calculations using a frequency-domain panel model. Further verification has been made for the forces on a container carrier in a rectangular harbour in irregular short-crested waves and compared with model tests. The results agree well with both the model test data and the frequency-domain calculations. All results have been obtained with the direct formulation, which directly solves the scattered potential at the collocation points of the panels at the hull as well as at other closed boundaries with input of the history of the normal velocities in the incident wave at the hull. This formulation is less vulnerable to effects of irregular frequencies.

The complete method with the wave conditions determined with the Boussinesq model has been validated against model test experiments for the forces on a container ship due to waves generated by a passing ship. The results proved that the Boussinesq model is able to treat the highly dispersive wash waves. The diffraction model is able to treat the nonlinear waves as calculated by the Boussinesq model as input conditions on the hull of the ship. The deviations with respect to the measured wave forces are small; the differences with respect to calculations with a frequency-domain diffraction model for the same input of incident waves are almost negligible, both for the first order and for the second order forces.

The results for an LNG carrier in irregular waves and for a longer simulation period with input of wave conditions from the Boussinesq model have shown that, again, the differences between a time-domain and frequency-domain approach for the diffraction are almost negligible. The time-domain computations are less ambiguous, because for a workable solution in the frequency-domain the simulation period needs to be divided into overlapping segments. Nevertheless, the frequency-domain approach is more efficient, because optimizations are easier achieved, e.g. by cutting off the Fourier transforms so that frequencies outside the range of interest can be omitted.

7.2 Recommendations

The following suggestions are made for further validation and improvement of the calculation methods:

- Validation of the Boussinesq-panel method in a harbour configuration using model test results is needed. The calculations of wave forces with input of fluid motions from the Boussinesq model presented in this thesis are only for a ship in open water. With application of the cut-cell approach in the Boussinesq model it is also possible to perform accurate computations with reflecting oblique boundaries. This makes the model suitable to calculate wave penetration in a harbour. Validation calculations should prove that it is appropriate that the Boussinesq model treats the waves in the harbour taking into account the fixed structures and that the panel model treats the scattering around the ship and the interaction of the scattered waves with the other structures. In the same manner as described in Chapter 6 a comparison can be made between the time-domain and frequency-domain approaches for the scattered waves.
- More insight is needed in the viscous effects which especially play a role in the flow between a ship and a quay wall. As an engineering solution it is suggested in this thesis to apply a partially transmissive boundary at the quay wall close to the ship. First of all this does not simulate the real flow pattern close to the wall and secondly the value of the transmission coefficient cannot be solved with potential theory. Experimental data should be used to tune the transmission coefficient. Otherwise, these data can be used to obtain a different solution to include viscous effects.
- Calculations with the infragravity wave model have been presented in this thesis for Tomakomai Port. An advantage in this case has been that the breakwater is a caisson type one. These caissons can be regarded as fully reflective for the long waves and therefore the model has no difficulties with it. However, if a rubble mound breakwater is applied the boundary can no longer be regarded as fully reflective, at least not for the higher frequency infragravity waves. These waves may not fully break, but energy is lost in the flow along the stones in the breakwater. It can even occur that very long waves penetrate through the breakwater, if the breakwater has a relatively open core. For proper modelling of these effects it should be possible to apply partially reflective boundaries and partially transmissive obstacles in the infragravity wave model. Ultimately the coefficients should be dependent on the wave frequency, but in a harbour it could be convenient if the coefficient is fixed and tuned for the main resonant frequency of the harbour basin.

BIBLIOGRAPHY

- Agnon, Y., Madsen, P. A., & Schäffer, H. A. (1999). A new approach to high-order Boussinesq models. *J. Fluid Mech.*, *399*, 319–333.
- Barthel, V., Mansard, E. P. D., Sand, S. E., & Vis, F. C. (1983). Group bounded long waves in physical models. *Ocean Engineering*, *10*, 261–294.
- Battjes, J. A., Bakkenes, H. J., Janssen, T. T., & Van Dongeren, A. R. (2004). Shoaling of subharmonic gravity waves. *J. Geophys. Res.*, *109*, C02009.
- Battjes, J. A., & Groenendijk, H. W. (1999). Shallow foreshore wave height statistics. In *Coastal Structures '99* (Vol. 1, pp. 29–35). Santander, Spain.
- Beck, R. F., & Liapis, S. (1987). Transient motions of floating bodies at zero forward speed. *J. Ship Res.*, *31*, 164–176.
- Berkvens, P. J. F. (1998). *Floating bodies interacting with water waves; simulations by a time-domain panel method*. PhD thesis, University of Twente, Enschede, The Netherlands.
- Biésel, F. (1952). Equations générales au second ordre de la houle irrégulière. *La Houille Blanche*, *7*, 371–376.
- Bingham, H. B. (2000). A hybrid Boussinesq-panel method for predicting the motion of a moored ship. *Coastal Engineering*, *40*, 21–38.
- Bingham, H. B., Korsmeyer, F. T., Newman, J. N., & Osborne, G. E. (1993). The simulation of ship motions. In *6th Int. Conf. on Numerical Ship Hydrodynamics* (pp. 561–579). IOWA City, IA.
- Booij, N., Ris, R. C., & Holthuijsen, L. H. (1999). A third-generation wave model for coastal regions. Part 1, model description and validation. *J. Geophys. Res.*, *104* (C4), 7649–7666.

- Borsboom, M. J. A., Doorn, N., Groeneweg, J., & Van Gent, M. R. A. (2000). A Boussinesq-type wave model that conserves both mass and momentum. In *Proc. 27th ICCE* (Vol. 1, pp. 148–161). Sydney, Australia.
- Borsboom, M. J. A., Groeneweg, J., Doorn, N., & Van Gent, M. R. A. (2001). Flexible boundary conditions for a Boussinesq-type wave model. In *Proc. WAVES 2001*. San Francisco, CA.
- Bowers, E. C. (1976). Long period oscillations of moored ships subject to short wave seas. *Trans. Roy. Inst. Naval Architects*, 118, 181–188.
- Bowers, E. C. (1977). Harbour resonance due to set-down beneath wave groups. *J. Fluid Mech.*, 79, 71–92.
- Bowers, E. C. (1998). Modelling techniques for the development of safe, efficient coastal harbour designs. In *Proc. 11th Int. Harbour Congress* (pp. 5.49–5.60). Antwerp, Belgium.
- Bruun, P. (1981). Breakwater or mooring system? *The Dock and Harbour Authority*, 62, 126–129.
- Buchner, B. (2006). The motions of a ship on a sloping seabed. In *Proc. OMAE 2006* (paper N° 92321). Hamburg, Germany.
- Clément, A. H. (1998). An ordinary differential equation for the Green function of time-domain free-surface hydrodynamics. *J. Eng. Math.*, 33, 201–217.
- Cummins, W. E. (1962). The impulse response function and ship motions. *Schiffstechnik*, 9, 101–109.
- Dalrymple, R. A. (1989). Directional wavemaker theory with sidewall reflection. *J. Hydraulic Res.*, 27, 23–34.
- Defant, A. (1961). *Physical oceanography* (Vol. II). New York: Pergamon.
- De Jong, M. P. J. (2004). *Origin and prediction of seiches in Rotterdam harbour basins*. PhD thesis, Delft University of Technology, The Netherlands.
- Faltinsen, O. M. (1990). *Sea loads on ships and offshore structures*. Cambridge University Press.
- Fuhrmann, D. R., Bingham, H. B., & Madsen, P. A. (2005). Nonlinear wave-structure interactions with a high-order boussinesq model. *Coastal Engineering*, 52, 655–672.

- Gallagher, B. (1971). Generation of surfbeats by non-linear wave interactions. *J. Fluid Mech.*, 49, 1–20.
- Gradshteyn, I. S., & Ryzhik, I. M. (2000). *Table of integrals, series and products* (6th ed.). San Diego: Academic Press.
- Herbers, T. H. C., Elgar, S., & Guza, R. T. (1995). Generation and propagation of infragravity waves. *J. Geophys. Res.*, 100(C12), 24,863–24,872.
- Hess, J. L., & Smith, A. M. O. (1962). Calculation of nonlifting potential flow about arbitrary three-dimensional bodies. *J. Ship Res.*, 8, 22–44.
- Hiraishi, T., Atsumi, Y., Kunita, A., Sekiguchi, S., & Kawaguchi, T. (1997). Observations of long period wave and ship motion in Tomakomai-port. In *Proc. 7th ISOPE Conf.* (Vol. 3, pp. 546–551). Honolulu, HW.
- Holthuijsen, L. H., Herman, A., & Booij, N. (2003). Phase-decoupled refraction-diffraction for spectral wave models. *Coastal Engineering*, 49, 291–305.
- Huijsmans, R. H. M. (1996). *Mathematical modelling of the mean drift force in current*. PhD thesis, Delft University of Technology, The Netherlands.
- Huntley, D. A., Guza, R. T., & Thornton, E. B. (1981). Field observations of surf beats. Part 1, progressive edge waves. *J. Geophys. Res.*, 86, 6451–6466.
- Hwang, L. S., & Tuck, E. O. (1970). On the oscillation of harbours of arbitrary shape. *J. Fluid Mech.*, 42, 447–464.
- Ippen, A. T., & Goda, Y. (1963). *Wave induced oscillations in harbors: The solution for a rectangular harbor connected to the open-sea* (Report 59). Hydrodynamics Laboratory, MIT.
- Janssen, T. T., Battjes, J. A., & Van Dongeren, A. R. (2003). Long waves induced by short-wave groups over a sloping bottom. *J. Geophys. Res.*, 108(C8), 3252.
- John, F. (1950). On the motion of floating bodies. Part 2. *Comm. Pure Appl. Math.*, 3, 45–101.
- Journée, J. M. J., & Adegeest, L. J. M. (2003). *Theoretical manual of strip theory program "SEAWAY for Windows"* (Report 1370). Delft University of Technology.

- Korsmeyer, F. T., & Bingham, H. B. (1998). The forward speed diffraction problem. *J. Ship Res.*, *42*, 99–112.
- Korsmeyer, F. T., & Sclavounos, P. D. (1989). The large-time asymptotic expansion of the impulse response function for a floating body. *Appl. Ocean Res.*, *11*, 75–88.
- Korvin-Kroukovsky, B. V., & Jacobs, W. R. (1957). Pitching and heaving motions of a ship in regular waves. *Trans. SNAME*, *65*, 590–632.
- Kubo, M., & Sakakibara, S. (1997). A time domain analysis of moored ship motions in a harbor considering harbor oscillations. In *Proc. 7th ISOPE Conf.* (Vol. 3, pp. 610–616). Honolulu, HW.
- Lee, C.-H., & Newman, J. N. (2005). Computation of wave effects using the panel method. In S. K. Chakrabarti (Ed.), *Numerical models in fluid-structure interaction* (pp. 211–251). Southampton: WIT Press.
- Lee, J. J. (1971). Wave-induced oscillation in harbours of arbitrary geometry. *J. Fluid Mech.*, *45*, 375–394.
- Longuet-Higgins, M. S., & Stewart, R. W. (1962). Radiation stress and mass transport in gravity waves, with application to 'surf beats'. *J. Fluid Mech.*, *13*, 481–504.
- Longuet-Higgins, M. S., & Stewart, R. W. (1964). Radiation stresses in water waves; a physical discussion with applications. *Deep-Sea Res.*, *11*, 529–562.
- Madsen, P. A., Bingham, H. B., & Schäffer, H. A. (2003). Boussinesq-type formulations for fully nonlinear and extremely dispersive water waves: derivation and analysis. *Proc. R. Soc. Lond. A*, *489*, 1075–1104.
- Madsen, P. A., Murray, R., & Sørensen, O. R. (1991). A new form of Boussinesq equations with improved linear dispersion characteristics. Part 1. *Coastal Engineering*, *15*, 371–388.
- Malenica, Š., Orozco, J. M., & Chen, X. B. (2005). Some aspects of multibody interactions in seakeeping. In *Proc. 15th ISOPE Conf.* (Vol. 3, pp. 68–75). Seoul, Korea.
- Maruo, H. (1960). The drift of a body floating on waves. *J. Ship Res.*, *4*, 1–10.
- Mei, C. C., & Agnon, Y. (1989). Long-period oscillations in a harbour induced by incident short waves. *J. Fluid Mech.*, *208*, 595–608.

- Mei, C. C., Stiassnie, M., & Yue, D. K. P. (2005). *Theory and application in ocean surface waves*. Singapore: World Scientific.
- Miles, J., & Munk, W. H. (1961). Harbor Paradox. *J. Waterways and Harbors Division*, 87, 111–130.
- Molin, B., Remy, F., Kimmoun, O., & Jamois, E. (2005). The role of tertiary wave interactions in wave-body problems. *J. Fluid Mech.*, 528, 323–354.
- Monárdez, P. (2004). *Numerical modeling of long waves in harbours*. MSc thesis, UNESCO-IHE Institute for Water Education, Delft, The Netherlands.
- Munk, W. H. (1949). Surf beats. *Eos Trans. AGU*, 30, 849–854.
- Mynett, A. E., Keuning, P. J., & Vis, F. C. (1985). The dynamic behaviour of moored vessels inside a harbour configuration. In *Int. Conf. Numerical and Hydraulic Modelling of Ports and Harbours* (pp. 211–220). Birmingham, UK.
- Newman, J. N. (1967). The drift force and moment on a ship in waves. *J. Ship Res.*, 11, 51–60.
- Newman, J. N. (1974). Second-order, slowly varying forces on vessels in irregular waves. In *Int. Symp. on the Dynamics of Marine Vehicles and Structures in Waves* (pp. 193–197). London, UK.
- Newman, J. N. (1986). Distribution of sources and normal dipoles over a quadrilateral panel. *J. Eng. Math.*, 20, 113–126.
- Newman, J. N. (1992). The approximation of free-surface Green functions. In P. A. Martin & G. R. Wickham (Eds.), *Wave Asymptotics* (pp. 107–135). Cambridge University Press.
- Newman, J. N., & Lee, C. H. (2002). Boundary-element methods in offshore structure analysis. *J. Offshore Mechanics and Arctic Engineering*, 124, 81–89.
- Nwogu, O. (1993). Alternative form of Boussinesq equations for nearshore wave propagation. *J. Waterway, Port, Coastal, Ocean Eng.*, 119, 618–638.
- OCIMF. (1997). *Mooring equipment guidelines* (2nd ed.). Oil Companies International Marine Forum. London: Witherby.
- Ohmatsu, S. (1975). On the irregular frequencies in the theory of oscillating bodies in a free surface. *Papers of Ship Research Institute*, 48, 1–13. (in Japanese)

- Ohyama, T., & Tsuchida, M. (1997). Expanded mild-slope equations for the analysis of wave-induced ship motion in a harbor. *Coastal Engineering*, 30, 77–103.
- Penney, W. G., & Price, A. T. (1952). The diffraction theory of sea waves and the shelter afforded by breakwaters. *Phil. Trans. R. Soc. Lond. A*, 244, 236–253.
- Peregrine, D. H. (1967). Long waves on a beach. *J. Fluid Mech.*, 27, 815–827.
- PIANC. (1995). *Criteria for movements of moored ships in harbours: a practical guide* (Supplement to bulletin N° 88). Report of working group PTC II-24.
- Pinkster, J. A. (1980). *Low frequency second order wave exciting forces on floating structures*. PhD thesis, Delft University of Technology, The Netherlands.
- Pinkster, J. A. (1995). Hydrodynamic interaction effects in waves. In *Proc. 5th ISOPE Conf.* (Vol. 3, pp. 414–419). The Hague, The Netherlands.
- Pinkster, J. A. (2004). The influence of a free surface on passing ship effects. *Int. Shipbuilding Progr.*, 51, 313–338.
- Pinkster, J. A., & Huijsmans, R. H. M. (1992). Wave drift forces in shallow water. In *Proc. BOSS'92* (pp. 1159–1183). London, UK.
- Pinkster, J. A., & Naaijen, P. (2003). Predicting the effect of passing ships. In *Proc. 18th Int. Workshop on Water Waves and Floating Bodies*. Le Croisic, France.
- Raichlen, F. (1966). Harbor resonance. In A. Ippen (Ed.), *Estuary and Coastline Hydrodynamics* (pp. 281–340). New York: McGraw-Hill.
- Remery, G. F. M., & Hermans, A. J. (1971). The slow drift oscillations of a moored object in random seas. In *Third Offshore Technology Conference* (Vol. 2, paper N° 1500). Houston, TX.
- Reniers, A. J. H. M., Roelvink, J. A., & Thornton, E. B. (2004). Morphodynamic modeling of an embayed beach under wave group forcing. *J. Geophys. Res.*, 109, C01030.
- Reniers, A. J. H. M., Roelvink, J. A., & Van Dongeren, A. R. (2000). Morphodynamic response to wave group forcing. In *Proc. 27th ICCE* (Vol. 4, pp. 3218–3228). Sydney, Australia.
- Roelvink, J. A. (1993). *Surf beat and its effect on cross-shore profiles*. PhD thesis, Delft University of Technology, The Netherlands.

- Sand, S. E. (1982a). Long wave problems in laboratory models. *J. Waterway, Port, Coastal, Ocean Div.*, 108, 492–503.
- Sand, S. E. (1982b). Long waves in directional seas. *Coastal Engineering*, 6, 195–208.
- Sasa, K. (2002). *A study on prediction of ship operation using numerical simulations and observed oceanographic database under swells and long period waves in harbour facing to open seas*. PhD thesis, Kobe University of Mercantile Marine, Kobe, Japan.
- Sawaragi, T., & Kubo, M. (1982). The motion of a ship in a harbor basin. In *Proc. 18th ICCE* (Vol. 3, pp. 2743–2762). Cape Town, South Africa.
- Schäffer, H. A. (1994). Edge waves forced by short-wave groups. *J. Fluid Mech.*, 259, 125–148.
- Shiraishi, S., Kubo, M., Sakakibara, S., & Sasa, K. (1999). A study on numerical simulation methods to reproduce long-period ship motions. In *Proc. 9th ISOPE Conf.* (Vol. 3, pp. 536–543). Brest, France.
- Sierevogel, L. M. (1998). *Time-domain calculations of ship motions*. PhD thesis, Delft University of Technology, The Netherlands.
- Symonds, G., Huntly, D. A., & Bowen, A. J. (1982). Two-dimensional surf-beat: long wave generation by a time-varying break point. *J. Geophys. Res.*, 87, 492–498.
- Tucker, M. J. (1950). Surfbeats: sea waves of 1 to 5 minutes' period. *Proc. R. Soc. Lond. A*, 202, 565–573.
- Ursell, F. (1949). On the heaving motion of a circular cylinder on the surface of a fluid. *Quart. J. Mech. Appl. Math.*, 2, 218–231.
- Van Daalen, E. F. G. (1993). *Numerical and theoretical studies of water waves and floating bodies*. PhD thesis, University of Twente, Enschede, The Netherlands.
- Van der Molen, W., Monárdez, P., & Van Dongeren, A. R. (2006). Numerical simulation of long-period waves and ship motions in Tomakomai Port, Japan. *Coastal Engineering Journal*, 48, 59–79.
- Van Dongeren, A. R., Klopman, G., Reniers, A. J. H. M., & Petit, H. A. H. (2001). High quality laboratory wave generation for flumes and basins. In *Proc. WAVES 2001* (Vol. 2, pp. 1190–1199). San Francisco, CA.

- Van Dongeren, A. R., Reniers, A. J. H. M., & Battjes, J. A. (2003). Numerical modeling of infragravity waves response during DELILAH. *J. Geophys. Res.*, *108*(C9), 3288.
- Van Giffen, I. K., Battjes, J. A., Van Dongeren, A. R., & Moes, J. (2003). Simulation of long waves in Saldanha Bay. In *Long Wave Symposium* (pp. 113–122). Thessaloniki, Greece.
- Van Oortmerssen, G. (1976). *The motions of a moored ship in waves*. PhD thesis, Delft University of Technology, The Netherlands.
- Wehausen, J. V. (1967). Initial-value problem for the motion in an undulating sea of a body with fixed equilibrium position. *J. Eng. Math.*, *1*, 1–19.
- Wehausen, J. V., & Laitone, E. V. (1960). Surface waves. In S. Flügge (Ed.), *Handbuch der Physik* (Vol. 9, pp. 446–778). Berlin: Springer.
- Weiler, O. M., & Dekker, J. (2003). Mooring container ships exposed to long waves. In *Proc. 13th Int. Harbour Congress*. Antwerp, Belgium.
- Wenneker, I., & Borsboom, M. J. A. (2005). A novel cartesian cut-cell approach. In *Finite Volumes for Complex Applications IV*. Marrakech, Morocco.
- Wenneker, I., Borsboom, M. J. A., Pinkster, J. A., & Weiler, O. M. (2006). A Boussinesq-type wave model coupled to a diffraction model to simulate wave-induced ship motion. In *Proc. 31st PIANC Congress*. Estoril, Portugal.
- Wichers, J. E. W. (1988). *Simulation model for single buoy moored tankers*. PhD thesis, Delft University of Technology, The Netherlands.
- Wilson, B. W. (1972). Seiches. *Adv. Hydroscience*, *8*, 1–94.
- Woo, S. B., & Liu, P. L. F. (2004). Finite-element model for modified Boussinesq equations. Part II, applications to nonlinear harbor oscillations. *J. Waterway, Port, Coastal, Ocean Eng.*, *130*, 17–28.
- Wu, J. K., & Liu, P. L. F. (1990). Harbour excitations by incident wave groups. *J. Fluid Mech.*, *217*, 595–613.
- Wuisman, W. K., & Van der Molen, W. (2005). Hydrodynamics of a moored LNG carrier behind a detached breakwater. In *Proc. WAVES 2005* (paper N° 97). Madrid, Spain.

APPENDIX

A. MODEL TEST RESULTS

The results of the model tests are presented here in the form of general characteristics of the frequency spectra obtained from the measured time-series. The results are given only for the tests with the harbour basin and irregular waves with a significant wave height $H_s = 3$ m. The results of the waves (Tables A.1 and A.2) are obtained from the tests that were resumed without the ship in the basin. WG1 is one of the wave gauges close to the wavemaker, WG8 is located at the rear of the harbour basin, WG16 is placed at the position of the centre of gravity of the ship and SG1 is a speed gauge at the same location which measures horizontal velocities along the wall of the harbour basin.

The significant wave heights are defined as $H_s \simeq 4\sqrt{m_0}$ with m_0 the zeroth moment of the surface elevation spectrum. The velocities measured at the speed gauge are multiplied by $\sqrt{h/g}$. In case of a travelling long wave along the harbour wall the values in the table for WG16 and SG1 would be equal. Therefore, more energy measured at WG16 indicates more potential energy found near anti-nodes for both lateral and transverse standing waves; more energy measured at SG1 indicates more kinetic energy found near anti-nodes of lateral standing waves.

The first period is defined as $T_1 = 2\pi m_0/m_1$ and the amplification is the ratio of the measured wave heights at WG8 and WG1. The results for high-frequency and low-frequency waves are given separately. The split frequency at which the spectrum is separated is chosen at $\omega = 0.25$ rad/s ($T \simeq 25$ s).

The results of the wave forces on the container ship are given in Tables A.3 and A.4 for the six modes $k = 1, 2, \dots, 6$ corresponding to surge, sway, heave, roll, pitch and yaw respectively. The significant wave force amplitudes are defined as $F_{k,s} \simeq 2\sqrt{m_0}$ with m_0 the zeroth moment of the wave force spectrum above or below the split frequency for the high or low-frequency wave force.

Table A.1: Results of short waves.

Test N ^o	H_s [m]				T_1 [s]				ampl.
	WG1	WG8	WG16	SG1	WG1	WG8	WG16	SG1	
4.2.1.1	3.07	2.66	2.70	1.02	8.2	9.6	8.6	9.9	.869
4.2.1.2	3.18	4.93	3.25	1.65	12.3	14.6	13.2	14.4	1.550
4.2.2.1	3.18	1.29	1.22	.59	8.7	9.8	9.4	9.8	.406
4.2.2.2	3.09	2.13	1.61	.95	12.1	15.1	14.1	14.3	.688
4.3.1.1	3.16	2.44	3.01	1.65	8.5	9.8	9.0	9.7	.774
4.3.1.2	2.92	3.85	3.15	2.05	12.1	14.2	13.0	13.6	1.315
4.3.2.1	2.93	2.01	2.14	1.07	8.6	9.7	9.0	9.7	.684
4.3.2.2	2.93	3.25	2.50	1.38	12.1	14.3	13.1	13.6	1.110
4.3.3.1	2.96	1.83	1.84	.83	8.6	9.6	8.8	9.7	.618
4.3.3.2	2.96	3.01	2.32	1.17	12.1	14.4	13.3	13.9	1.016

Table A.2: Results of long waves.

Test N ^o	H_s [m]				T_1 [s]				ampl.
	WG1	WG8	WG16	SG1	WG1	WG8	WG16	SG1	
4.2.1.1	.153	.191	.180	.153	57.2	59.8	55.5	86.7	1.248
4.2.1.2	.258	.407	.360	.276	52.5	47.5	48.9	57.4	1.574
4.2.2.1	.262	.323	.261	.180	51.3	83.9	72.2	87.2	1.233
4.2.2.2	.281	.460	.413	.246	46.1	58.8	55.7	61.2	1.638
4.3.1.1	.095	.139	.120	.135	49.0	54.9	54.7	70.2	1.463
4.3.1.2	.125	.225	.187	.182	45.3	55.2	54.0	59.8	1.801
4.3.2.1	.099	.106	.091	.100	51.9	57.4	53.3	79.3	1.064
4.3.2.2	.148	.218	.166	.148	48.4	52.8	53.9	61.4	1.475
4.3.3.1	.107	.118	.098	.093	47.6	57.2	55.3	82.9	1.102
4.3.3.2	.155	.240	.185	.151	48.8	51.3	51.4	60.0	1.544

Table A.3: Results of high-frequency wave forces.

Test N°	$F_{k,s}$ [MN, MNm]						$T_{1,k}$ [s]					
	1	2	3	4	5	6	1	2	3	4	5	6
4.2.1.1	5.0	38.9	51.1	81.7	2497	2205	10.2	10.1	10.6	9.3	10.1	9.6
4.2.1.2	7.5	28.3	71.4	55.3	3252	1681	14.3	11.5	13.9	10.8	14.0	11.5
4.2.2.1	2.2	18.3	23.6	33.8	1068	951	10.4	10.2	10.8	9.4	10.3	9.6
4.2.2.2	3.7	12.9	37.0	25.1	1625	708	14.7	12.1	14.6	11.5	14.6	11.6
4.3.1.1	4.6	29.3	39.6	69.8	2243	1717	10.1	10.0	10.4	9.0	10.0	9.5
4.3.1.2	6.6	21.4	53.7	48.0	2877	1283	14.2	11.6	13.9	10.8	14.0	11.3
4.3.2.1	3.8	26.6	33.7	58.8	1861	1568	10.0	9.9	10.5	9.1	10.0	9.5
4.3.2.2	5.5	19.3	49.2	42.2	2403	1147	14.1	11.4	14.0	10.8	13.9	11.3
4.3.3.1	3.4	26.3	32.8	55.9	1726	1491	10.0	9.9	10.5	9.1	9.9	9.4
4.3.3.2	5.0	18.5	48.8	39.6	2198	1088	14.2	11.6	14.1	10.9	13.9	11.3

Table A.4: Results of low-frequency wave forces.

Test N°	$F_{k,s}$ [MN, MNm]						$T_{1,k}$ [s]					
	1	2	3	4	5	6	1	2	3	4	5	6
4.2.1.1	.24	1.99	4.1	6.7	120	65	56.4	116.6	71.9	81.2	65.2	68.5
4.2.1.2	.69	1.57	10.1	8.3	283	91	45.5	64.3	52.1	64.6	43.3	74.6
4.2.2.1	.37	.45	7.6	4.3	164	15	52.7	89.2	81.4	79.4	56.7	65.1
4.2.2.2	.65	.42	11.6	6.3	274	22	46.3	52.0	59.1	59.9	47.4	66.2
4.3.1.1	.18	1.39	2.4	6.5	90	57	59.8	98.7	66.3	78.6	63.7	65.7
4.3.1.2	.39	.94	4.7	5.7	163	54	51.6	62.1	61.3	70.2	47.7	66.2
4.3.2.1	.15	.99	2.0	4.3	74	44	49.3	90.3	67.0	74.6	54.5	62.7
4.3.2.2	.35	.74	4.6	4.7	145	44	46.8	61.5	59.1	69.4	45.7	69.4
4.3.3.1	.15	.92	2.4	3.9	74	35	49.8	94.3	65.5	74.9	55.4	64.0
4.3.3.2	.37	.68	5.1	4.7	156	39	45.4	63.3	55.7	73.9	44.7	68.3

B. COMPUTATION OF THE GREEN FUNCTION

The time-domain Green function is the solution of the Cauchy-Poisson problem for a unit source below the free surface given by $\sigma(\vec{\xi}, t) = \delta(t)$. The solution

$$G(\vec{x}, \vec{\xi}, t) = \delta(t)G^{(0)}(\vec{x}, \vec{\xi}) + H(t)G^w(\vec{x}, \vec{\xi}, t) \quad (\text{B.1})$$

consists of a Rankine part $G^{(0)}$ and a wave part G^w ; $\delta(t)$ is the Dirac delta function and $H(t)$ the Heaviside step function. The Rankine part is an immediate influence of the source on the field point and the wave part is a memory part which describes the influence due to a wave that has been formed at the free surface. The solution for the case of finite water depth is given by Wehausen and Laitone (1960, Eq. 13.53):

$$G^{(0)} = \frac{1}{r} + \frac{1}{r_2} - 2 \int_0^\infty \frac{e^{-kh}}{\cosh kh} \cosh k(z+h) \cosh k(\zeta+h) J_0(kR) dk \quad (\text{B.2})$$

$$G^w = 2 \int_0^\infty \frac{\sqrt{gk \tanh kh}}{\cosh kh \sinh kh} \sin(t\sqrt{gk \tanh kh}) \times \cosh k(z+h) \cosh k(\zeta+h) J_0(kR) dk \quad (\text{B.3})$$

where r and r_2 are the distances from the field point to the source and to the mirror source below the sea floor respectively and R is the horizontal distance. z and ζ are the vertical coordinates of the field and source point respectively. J_0 is the Bessel function of the first kind.

The variables are nondimensionalized with respect to the acceleration of gravity, g , and the water depth, h , thus defining the dimensionless variables $X = R/h$, $Y = -\zeta/h$, $Z = -z/h$ and $T = t\sqrt{g/h}$. After applying the addition theorem for the products of two hyperbolic cosines, the formulation of the the Green function expressed in the dimensionless variables takes the form

$$G^{(0)} = h^{-1} [F_0(X, 2 - Y - Z) + F_0(X, Y - Z)] \quad (\text{B.4})$$

$$G^w = h^{-1} \sqrt{g/h} [(F(X, 2 - Y - Z, T) + F(X, Y - Z, T))] \quad (\text{B.5})$$

with

$$F_0(X, V) = \frac{1}{\sqrt{X^2 + V^2}} - \int_0^\infty \frac{e^{-k}}{\cosh k} \cosh kV J_0(kX) dk \quad (\text{B.6})$$

$$F(X, V, T) = 2 \int_0^\infty \frac{\omega}{\sinh 2k} \cosh kV \sin \omega T J_0(kX) dk \quad (\text{B.7})$$

where $\omega = \sqrt{k \tanh k}$. F_0 can be expressed by the contribution of an array of Rankine image sources. Following the derivations made by Newman (1992), the solution can be constructed from a pair of periodic source arrays

$$F_0 = \sum_{n=-\infty}^{\infty} \frac{(-1)^n}{\sqrt{X^2 + (V + 2n)^2}} - \sum_{n=1}^{\infty} \frac{(-1)^n}{n} - \log 2 \quad (\text{B.8})$$

The $(-1)^n/n$ term is added to speed up convergence. Alternatively, Fourier series can be derived for F_0 (Gradshteyn & Ryzhik, 2000, Eq. 8.526.2):

$$F_0(X, V) = 2 \sum_{m=0}^{\infty} \cos((m + \frac{1}{2})\pi V) K_0((m + \frac{1}{2})\pi X) \quad (\text{B.9})$$

where K_0 is the modified Bessel function of the second kind. These series converge rapidly, except for small X . Therefore, Eq. B.9 is used for $X > \frac{1}{2}$ and Eq. B.8 for smaller distances.

The evaluation of the wave part of the Green function provides a more challenging problem. The kernel of the integral in Eq. B.3 is highly oscillatory, so that standard methods for numerical quadrature are inefficient. The evaluation of the infinite depth Green function can be simplified by making a change of variables, so that the Green function can be expressed by a function of only two variables. Clément (1998) used this decomposition to reformulate the Green function into a general fourth-order ordinary differential equation. In case of the finite depth Green function however, this decomposition is not possible making an efficient computation much more complicated. The formulation in Eq. B.7 is the same integral as studied by Newman (1992). For small values of X and T the evaluation is straightforward, after making a polynomial approximation of the kernel. Newman applied an approach based on asymptotic polynomial expansions for the evaluation if X and T are large. Three overlapping domains are defined in relation to the front $X = T$. An optimal contour of integration is found for each combination of X and T . It is the objective here to find a solution to Eq. B.7 which has the same contour of integration for each time step and which is based on coefficients which are independent of time. Although maybe not ideally

optimal, in that case the evaluation of the Green function for a large number of time steps is sufficiently efficient.

For large X Eq. B.7 is decomposed in the form

$$F = f_0 + \mathfrak{I}_m(f_+ + f_-) \quad (\text{B.10})$$

where the three components are defined as

$$f_0 = 2 \int_0^\Omega \frac{\omega^2}{\omega^2 + \sinh^2 k} \cosh kV \sin \omega T J_0(kX) d\omega \quad (\text{B.11})$$

$$f_\pm = \int_\Omega \frac{\omega^2}{\omega^2 + \sinh^2 k} \cosh kV e^{i\omega T \pm ikX} \sqrt{\frac{2}{\pi kX}} e^{\mp i\pi/4} \sum_{j=0} b_j \left(\frac{\pm i}{kX}\right)^j d\omega \quad (\text{B.12})$$

and

$$b_j = \frac{[\Gamma(j+\frac{1}{2})]^2}{\pi 2^j j!} \quad (\text{B.13})$$

are the coefficients of the asymptotic expansion of the Bessel function. This expansion is not valid close to the origin, so that the integrand for f_0 is used in this region up to Ω , e.g. where $kX = 20$. The integration parameter is changed to ω so that ωT is a linear argument. In Eq. B.12 the power of the exponential is not linear. In order to linearize this, the Taylor series

$$k(\omega) = \sum_{n=0} \frac{k_n \tilde{\omega}^n}{n!} \quad (\text{B.14})$$

are used in terms of the n^{th} -order derivatives k_n and a local variable $\tilde{\omega} = \omega - \omega_0$ relative to an arbitrary ω_0 . A series expansion is made of the higher order powers to give

$$e^{i\omega T \pm ikX} = e^{i\omega_0 T \pm ik_0 X} e^{i\tilde{\omega}(T \pm k_1 X)} \sum_{m=0} \frac{(\pm iX)^m}{m!} \sum_{n=2m} c_{mn} \tilde{\omega}^n \quad (\text{B.15})$$

where c_{mn} are the polynomial coefficients related to the higher order derivatives of $k(\omega)$. The first coefficients in these series are

$$c_{00} = 1 \quad (\text{B.16})$$

$$c_{0n} = 0, \quad n = 1, 2, \dots \quad (\text{B.17})$$

$$c_{1n} = \frac{k_n}{n!}, \quad n = 2, 3, \dots \quad (\text{B.18})$$

$$c_{24} = \frac{k_2^2}{2^2} \quad (\text{B.19})$$

$$c_{25} = \frac{2k_2k_3}{2!3!} \quad (\text{B.20})$$

$$c_{26} = \frac{2k_2k_4}{2!4!} + \frac{k_3^2}{(3!)^2} \quad (\text{B.21})$$

$$c_{36} = \frac{k_2^3}{2^3} \quad (\text{B.22})$$

With these expansions of the Bessel function, the kernels in Eqs. B.11 and B.12 can be expressed as the products of a trigonometric function with a linear argument and a regular polynomial,

$$f_0 = 2 \int_0^\Omega \sin \omega T \sum_{n=0} p_n^{(0)}(X, V) \omega^n d\omega \quad (\text{B.23})$$

$$f_\pm = e^{i\omega_0 T \pm ik_0 X \mp i\pi/4} \int_\Omega e^{i\tilde{\omega}(T \pm k_1(\omega_0)X)} \times \sum_{n=0} [p_n^{(\pm)}(X, V, \omega_0) + iq_n^{(\pm)}(X, V, \omega_0)] \tilde{\omega}^n d\omega \quad (\text{B.24})$$

so that analytical integration is possible (Gradshteyn & Ryzhik, 2000, §2.635). The integral in Eq. B.24 is evaluated subsequently at each partition of the integrand. The order of the polynomial is chosen as 4 and the step size is optimized in such a way that an accuracy of 6 significant decimals in the result of the Green function is achieved. The polynomial coefficients p_n and q_n are (as intended) independent of time, so that they need to be evaluated only once for the calculation of Green functions for a given field and source point. Evaluation of time series of Green functions is then easily carried out with these constant coefficients.

A similar approach is applied to evaluate the horizontal and vertical derivatives of the Green function.

CURRICULUM VITAE

The author was born in Harderwijk on the 25th of June 1977. He started secondary school in 1989 at the Corderius Lyceum in Amersfoort and received the vwo-diploma in 1995. He studied Civil Engineering from 1995 to 2001 at the Delft University of Technology, where he graduated at the Department of Hydraulic and Geotechnical Engineering on a verification study using prototype measurements concerning the behaviour of moored LNG carriers in swell. The MSc graduation project was conducted in order of Shell Global Solutions and performed at Royal Haskoning.

The PhD graduation project leading to this dissertation was performed from 2002 until 2006 at the Section of Hydraulic Engineering of the Delft University of Technology under the supervision of the promoters, prof.ir. H. Ligteringen and prof.dr.ir. J.A. Pinkster, and partly in cooperation with WL|Delft Hydraulics. The project was supported by the Water Research Centre of the Delft University of Technology.

From June until October 2006 the author has worked for Royal Haskoning, division Maritime in Rotterdam, on an LNG terminal's mooring analysis study applying the infragravity-strip theory method as described in this dissertation.

ACKNOWLEDGEMENTS

It feels almost like the end of era after spending more than eleven years studying and doing research in Delft; a little longer than I had expected beforehand due to the years as a PhD student. Continuing doing research is maybe not the first thing you think of after completing an engineering study. Therefore, I wish to thank Han Ligteringen for his recognition that this was the right step for me to take and offering me the opportunity to start this research project which indeed appeared to be the way I liked to continue. After the definition of the research objectives I received much freedom and time to find solutions and in the writing process I found a sharp eye in formulations. Furthermore, his idea to offer me a short job at Royal Haskoning was a good opportunity to bring the developed models into practice and to bridge the period between the work at the university and my leave to South Africa.

Discussions with Jo Pinkster were always very inspiring and our cooperation with respect to verification computations went rather smoothly. When I provided input data for DELFRAC, he would send the results mostly the next day; obviously very pleasant when you are very curious to the results and keen on proceeding with the postprocessing.

I wish to thank Otto Weiler from WL|Delft Hydraulics for providing the results of the model test experiments. These tests came at exactly the right moment, so that new data came available to compare with. I further thank him for his efforts in the first stage of the project, when we were able to set a goal which would lead to scientific and practicable solutions. Ivo Wenneker and Mart Borsboom are acknowledged for their efforts in the work in combination with TRITON, the comparison with the model test data and Ivo's useful comments to the text.

I am very thankful to Tetsuya Hiraishi from the PARI institute in Japan for providing the measured data from the port of Tomakomai and his kind hospitality during my visit to Japan. Also the first-hand information provided by Kenji Sasa was very helpful here. Patricio Monárdez has done much work dealing with these data during his MSc graduation project performed at our section. The cooperation with

him was very pleasant, also regarding the discussions we had with Ap van Dongeren.

Besides the research work, there should be room for side stories which were always nearby with my roommate, Mathijs van Ledden, Fabiana Maccharini or Bianca Stalenberg, or in the coffee room during discussions with colleagues. Also (email) conversations with Robert van Leijenhorst and other friends about cycling, football and politics were a good distraction to reset my mind. Finally, I would like to thank my parents for there ever present support. I hope I have always been able to reassure them, especially in final stages of the project.

Wim van der Molen
Delft, October 2006

